



UNIVERSITAT DE BARCELONA

Studies of Black Hole Horizons

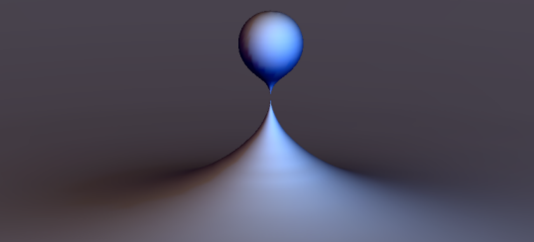
Marina Martínez Montero

ADVERTIMENT. La consulta d'aquesta tesi queda condicionada a l'acceptació de les següents condicions d'ús: La difusió d'aquesta tesi per mitjà del servei TDX (www.tdx.cat) i a través del Dipòsit Digital de la UB (diposit.ub.edu) ha estat autoritzada pels titulars dels drets de propietat intel·lectual únicament per a usos privats emmarcats en activitats d'investigació i docència. No s'autoritza la seva reproducció amb finalitats de lucre ni la seva difusió i posada a disposició des d'un lloc aliè al servei TDX ni al Dipòsit Digital de la UB. No s'autoritza la presentació del seu contingut en una finestra o marc aliè a TDX o al Dipòsit Digital de la UB (framing). Aquesta reserva de drets afecta tant al resum de presentació de la tesi com als seus continguts. En la utilització o cita de parts de la tesi és obligat indicar el nom de la persona autora.

ADVERTENCIA. La consulta de esta tesis queda condicionada a la aceptación de las siguientes condiciones de uso: La difusión de esta tesis por medio del servicio TDR (www.tdx.cat) y a través del Repositorio Digital de la UB (diposit.ub.edu) ha sido autorizada por los titulares de los derechos de propiedad intelectual únicamente para usos privados enmarcados en actividades de investigación y docencia. No se autoriza su reproducción con finalidades de lucro ni su difusión y puesta a disposición desde un sitio ajeno al servicio TDR o al Repositorio Digital de la UB. No se autoriza la presentación de su contenido en una ventana o marco ajeno a TDR o al Repositorio Digital de la UB (framing). Esta reserva de derechos afecta tanto al resumen de presentación de la tesis como a sus contenidos. En la utilización o cita de partes de la tesis es obligado indicar el nombre de la persona autora.

WARNING. On having consulted this thesis you're accepting the following use conditions: Spreading this thesis by the TDX (www.tdx.cat) service and by the UB Digital Repository (diposit.ub.edu) has been authorized by the titular of the intellectual property rights only for private uses placed in investigation and teaching activities. Reproduction with lucrative aims is not authorized nor its spreading and availability from a site foreign to the TDX service or to the UB Digital Repository. Introducing its content in a window or frame foreign to the TDX service or to the UB Digital Repository is not authorized (framing). Those rights affect to the presentation summary of the thesis as well as to its contents. In the using or citation of parts of the thesis it's obliged to indicate the name of the author.

STUDIES OF
BLACK HOLE HORIZONS



PhD Thesis
Marina Martínez Montero

PhD Thesis

Studies of Black Hole Horizons

MARINA MARTÍNEZ MONTERO

Departament de Física Quàntica i Astrofísica,
Facultat de Física



UNIVERSITAT_{DE}
BARCELONA

Studies of Black Hole Horizons

A dissertation presented by

Marina Martínez Montero

to the Faculty of Physics of the University of Barcelona in partial fulfilment of the requirements for the degree of Doctor of Philosophy in Physics. This thesis was prepared under the supervision of

Dr. Roberto Emparan

from the Department of Quantum Physics and Astrophysics of the University of Barcelona.

Director: Dr. Roberto Emparan

Tutor: Dr. Roberto Emparan

*to Carmen, my parents
and my grandmother*

Preface

This thesis is focused entirely on classical and thermodynamical aspects of black hole physics. Several types of black holes, together with the phenomena intrinsic to each one of them, have been investigated and are discussed in it. Some of the research exposed in this thesis has been done in an arbitrary number of dimensions and the rest in a specified number of dimensions ($d = 4, 5,$ and 6). Different techniques have been used in obtaining the results. While most of the analysis is analytic (sometimes exact, sometimes through effective descriptions), numerical methods have also been employed. Throughout the whole thesis special attention is paid to the geometry and other properties of black hole horizons.

The thesis is presented in the form of a “Compilation of Articles” and is divided in three parts. The first part is an introduction with essential background for the publications. The second part is divided into four chapters:

- Black Branes in a Box: Hydrodynamics, Stability, and Criticality
- Black String Flow
- Bumpy Black Holes
- Exact Event Horizon of a Black Hole Merger

Each chapter contains a published article. The last part of the thesis contains the conclusions and a summary in Spanish.

Marina Martínez Montero
Barcelona, July 2016

Acknowledgements

Quiero empezar por agradecer a mi director de tesis Roberto Emparan, a quien admiro y aprecio mucho. Estos años de tesis han sido fantásticos, he aprendido un montón y realmente lo he pasado súper bien. Siempre has estado presente con buenas ideas, buenos consejos e involucrándote con interés en todos los proyectos; trabajar contigo es una gozada. No es necesario que diga que sin ti esta tesis no habría sido posible. Quiero agradecer también a Pau Figueras por brindarme la oportunidad de desarrollar el proyecto de los *bumpy black holes* y por toda la ayuda y atención prestada en el camino. Me gustó mucho trabajar contigo en ese proyecto, eres un gran colaborador. Agradecer también a la Generalitat de Catalunya por la beca FI, gracias a la cual he podido realizar esta tesis.

Ahora agradeceré a mi papá y a mi mamá que siempre me han cuidado mucho y con quienes siempre me lo paso genial. Me habéis apoyado en todas las decisiones que he tomado en mi vida y en gran parte gracias a vosotros he podido realizar esta tesis. Sois unos padres estupendos aunque os burléis de mi fijación por la gastronomía asiática y no me dejéis ganar al tenis ;) . Muchísimas gracias por toda la vida, todo el cariño y por haberme enseñado el placer de viajar.

También quiero dar las gracias al resto de mi familia. En especial agradecer a mi hermanito Eloy con quien siempre me lo paso pipa practicando deportes extremos (yeaaaahh!) y quien es una gran persona, a mi yaya Isabel quien siempre me mimó más que nadie y siempre tenía ganas de verme, y a mis tietas Lini y Maribel que me han hecho mucha compañía estos años que llevo viviendo en Barcelona y han sido fantásticas y divertidas.

Los amigos son muy importantes en la vida y estos agradecimientos estarían muy incompletos sin mencionarlos a ellos.

Quiero empezar por agradecer a mi gran amiga Adri por todas las risas, las horas de salsa, las competiciones de picante (sabes que siempre ganaré ;)) y las charlas motivacionales cuando tocaba, eres una grande! Continuaré agradeciendo a mi amigo Andresito quien siempre ha confiado en mis capacidades bastante más que yo misma. Me encanta la amistad que tenemos, nuestras conversaciones en las que arreglamos el mundo y tu exquisito sentido del humor. Eres un tío genial y hacia ti sólo tengo amor y admiración.

Quiero dar las gracias a mi amigo más friki Oriol :-* , por haber ayudado mucho a mi adaptación en Barcelona y por todos los ratos divertidos que hemos compartido. A Blai por el tenis, la física y las charlas de la vida. Gracias a Albert por los juegos, las birras, la paciencia, las comas (y muchas otras cosas del lenguaje) y sus consejos tanto en el fútbol sala como en la vida. Siempre me lo paso genial contigo :). A Carla por su grandísima paciencia y su buena amistad. Gracias a los dos, he aprendido mucho de ambos. A Isa por las interesantes conversaciones y por su agradable compañía. A Núria G. por sus divertidas locuras y su cariño. A Iván por ser un tío genial y por animarme constantemente a lo largo de la tesis. A mi eterno compañero de despacho, Miquel, por hacer que las jornadas hayan sido siempre muy divertidas y por las pausas jugando con el Google Maps (los atolones lo petan!). A Christiana por sus buenos consejos, su sabiduría en la física y su

cariño. Quiero dar las gracias también a Blai P., Daniel, David, Eli, Genís, Javier, Julià, Luis C., Luis F., Markus, Miguel, Mirian y a Vicente (espero no haberme dejado a nadie) por haber sido geniales conmigo en el tiempo que hemos compartido en la UB. Muchas gracias también a las secretarias Bea, Elena y Cristina porque sois majísimas y siempre habéis estado ahí ayudando en lo que ha hecho falta.

Quiero agradecer a las chicas del Stabulo Boss: Anna, Carla, Carol, Carmen, Dela, Eli, Kim, Kumy, Maricruz, Miriam, Núria V., Paula y las Silvias por hacer que el miércoles sea siempre el mejor día de la semana. Muchas gracias también a los compis de la UAB por las excursiones, disfraces, lasertag, juegos de mesa, paintball, partidos de fútbol de algunos viernes y por dejarme múltiples veces una mesa para trabajar. Sois un grupo genial! Muchas gracias a Laura por todos los conciertos de Supersubmarina (cuántos llevamos ya? jeje), las motos y las clases de cocina en inglés y muchas gracias a Núria V. por todas las risas y por siempre estar dispuesta a hacer el calentamiento del fútbol conmigo. Muchas gracias también a Anna y Arnau por el espectacular viaje que nos marcamos por Camboya; me atrevo a decir que ha sido el viaje que más ha cambiado mi manera de ver la vida. Viajar con vosotros es un auténtico placer. Próxima parada: salar de Uyuni! Muchas gracias también por hablarme de ESF, soy mucho más feliz desde que metí en el grupo.

Daré las gracias también a mis amigos de Costa Rica que viven en Barcelona que son todos muy pura vida y siempre están ahí cuando los necesitas! Kim, Kumy, Fabián, Glori y Guillem, tener un grupo de amigos como vosotros es tener un cachito de Costa Rica aquí, muchas gracias por todo lo que hemos compartido, mucho amor para todos vosotros. También a los amigos ticos están por otros lados del mundo Diana, Elfrén, Isa, Manu, Mile y Santi, soy muy feliz cada vez que nos vemos y todos habéis enriquecido mi vida en algún que otro aspecto.

I want to thank some of the people I have met in conferences/schools etc, Benson, Helvi, Mirah, Suresh, Will and Wilke. Thank you for the interesting discussions, beers, dancing and hiking. Thank you Thomas Lai and Baobab for your kind hospitality in Taiwan. I like all of you guys a lot and I expect to be seeing more of you in the near future. I also want to thank Harvey Reall and Pei Ming Ho for hosting me in their groups during my stays at DAMTP and NTU. Also Vitor Cardoso, Niels Obers and the COST Action for funding some of the schools and conferences I have attended during the thesis.

Por último quiero dar las gracias a Carmen, la persona que más feliz me hace en todo el mundo. Me siento muy afortunada por poder haber compartido la vida contigo todos estos años y por todos los que nos quedan por delante. Muchas gracias por el apoyo y la confianza que has demostrado constantemente tener en mí, realmente siento muy bien :). Muchas gracias por tu paciencia aguantando todas y cada una de mis crisis :) y también por aguantarme aún cuando no tengo crisis, sé que digo tonterías todo el rato. Muchas gracias también por todo lo que hemos disfrutado juntas: viajes (muuuuchos viajes siiiii!!!!), fútbol, tenis, snow, surf (voy a parar de decir deportes... ;)), fotos, comidas exóticas, baile, etc. Muchas gracias por la vida que nos espera. Eres sin duda alguna mi persona favorita y te amo con todo mi corazón :-*.

CONTENTS

Preface	vii
Acknowledgements	ix
1 Introduction	1
1.1 Black branes	3
1.2 Flowing horizons	9
1.3 Rotating black holes	12
1.4 Black hole mergers	16
References	21
Collection of Articles	23
2 Black Branes in a Box: Hydrodynamics, Stability, and Criticality	25
3 Black String Flow	47
4 Bumpy Black Holes	63
5 Exact Event Horizon of a Black Hole Merger	87
Summary and Conclusions	111
6 Conclusions	113
7 Resumen en Castellano	115
7.1 Branas negras en una caja	115
7.2 Horizontes que fluyen (<i>Black String Flow</i>)	116
7.3 Agujeros negros <i>bumpy</i>	117
7.4 Fusión de agujeros negros	118

INTRODUCTION

General relativity (GR) is an amazing theory of gravity. A hundred years ago, when it was first proposed by Albert Einstein, it changed completely our way of understanding the gravitational interaction. Thanks to GR, gravity is no longer viewed as an instantaneous force, as it was in Newton's theory, but as the curvature of a dynamical spacetime. Einstein's equations,

$$R_{\mu\nu} - \frac{1}{2}Rg_{\mu\nu} = 8\pi GT_{\mu\nu}, \quad (1.1)$$

show the interplay between geometric quantities such as the metric, the Ricci scalar and the Ricci tensor, and the matter content, described by a stress-energy tensor. Through these equations, matter curves spacetime and spacetime tells matter how to move. The universal character of gravity here is automatic. All particles immersed in a given spacetime follow geodesics through it in the absence of external forces.

Apart from being beautiful and elegant, GR has been exhaustively tested. It is important to stress here that much of these tests were predictions that previous to GR were totally inconceivable. The first success of the theory was to explain Mercury's perihelion precession. This was followed by the observation of deflection of light by the Sun (in the famous 1919 total Sun eclipse), the gravitational redshift of light moving in a gravitational field (1959)¹, the Shapiro time delay a signal experiences when passing through a massive object (first measured in 1966) and the orbital decay due to gravitational wave emission (first reported in 1978, Nobel prize in 1993) among others. The most recent triumph, announced earlier this year, has been the direct observation of gravitational waves by LIGO. Most of the GR tests had been done within the solar system and hence were tests of its weak field regime. The gravitational wave detected on September 14th, 2015 (GW150914) was generated during the merger of two black holes of $\sim 30M_{\odot}$ each, in the most violent and strong gravitational field event ever observed.

GR predicts the existence of the most incredible objects ever conceived, black holes. These are objects in which gravity is so strong that not even light can escape. They are characterised by having an event horizon; this is the null surface limiting

¹This experiment (not observation), by Pound and Rebka, was the first one done to test GR. Notice it was performed more than 30 years after the theory was proposed.

which points in spacetime are causally connected to infinity, that is, the surface of no return.

Black holes lie at the core of the theory. The most popular black holes, Schwarzschild's and Kerr's, are in fact solutions to the vacuum Einstein's equations (they are purely curved spacetime). Then, in order to describe some black hole processes, one needs nothing more than spacetime dynamics. For example, the description of the inspiraling, merger and final relaxation/ringdown of a black hole fusion event can be accomplished solely by considering the vacuum Einstein's equations

$$R_{\mu\nu} = 0. \tag{1.2}$$

Solving the vacuum Einstein's equations and extracting details such as the event horizon or the gravitational radiation profile of a black hole merger is a complicated task. It requires in general sophisticated numerical techniques and heavy computational resources. Chapter 5 contains a publication in which we show that there is a limit in which the event horizon of a black hole merger can be described in an analytic way. More details on this are given in Sec. 1.4.

Dynamical situations, as we have mentioned above, are extremely complicated. However, when one considers static or stationary solutions, the picture simplifies in a substantial manner. In fact, for vacuum GR in four dimensions, there are uniqueness theorems that show the only asymptotically flat (AF) static or stationary solutions are respectively Schwarzschild's or Kerr's. For stationary and AF black hole solutions of Einstein-Maxwell's theory, there is a no-hair theorem that tells us that any black hole solution (non-singular on and outside the event horizon) can be described only by three parameters, mass, charge and angular momentum and is given by the Kerr-Newman solution.

Black holes are described in general by very few parameters, as opposed to the number of parameters needed to describe a star in a detailed way. It seems that there is something suspicious, and that one could lose entropy by throwing bodies into a black hole, or in fact, in the gravitational collapse of a star. The fact that black holes are described by very few parameters together with the resemblance between the laws of black hole mechanics and the laws of thermodynamics led Bekenstein to propose that an entropy could be associated to black holes and that it was proportional to their area² [1]. It was Hawking, nevertheless, who made this relation precise. A quantum field theory (QFT) calculation in curved spacetime showed that black holes are indeed thermodynamic bodies and that their temperature and entropy depend only on asymptotic charges [2].

It was realised immediately that if black holes had a temperature and radiated, it was possible for them to eventually evaporate. This led to the formulation of the black hole information paradox [3]. It states that it is not possible to trace back the initial state that first formed the black hole from the emitted Hawking quanta and hence information is lost in the black hole formation/evaporation process. This has turned into a fundamental problem in theoretical physics (it has been around

²He also noticed that there was a positive quantity, the surface gravity, which was an analogue of the temperature when comparing the laws of thermodynamics with that of black holes. It was stressed, however, that this temperature was not to be understood as a real one.

already 40 years). The information paradox expresses an existing tension between GR and QFT and highlights the need of a theory of quantum gravity.

One of the strongest candidates for a theory of quantum gravity is string theory. It has been around for many years now and a lot of effort has been put into developing it. Being able to identify the microscopic degrees of freedom that account for the entropy of a specific black hole has been one of its major successes [4]. In order for string theory to be a sensible theory, however, extra dimensions are unavoidable. The presence of extra dimensions within string theory, which contains GR, fomented the study and interest in higher-dimensional classical gravity. GR and specifically black holes in more than four dimensions have been an active field of study in the past decades [5]. Nevertheless, it is important to mention that the interest in GR with extra dimensions dates back to Kaluza's theory [6] in 1921.

Gravity in higher dimensions is different in a number of aspects. Extra dimensions allow for a richer space of solutions and, among other things, the uniqueness theorems that we knew from four dimensions do no longer hold. That is, in some cases there is more than one static or stationary black hole solution for the same asymptotic charges. Rotation also changes; increasing the number of dimensions permits more independent rotation planes. The possibility of extended horizons, like black strings and black branes, and the dynamics associated to those, are features that also arise from considering extra dimensions. As we have briefly mentioned here, when gravity is extended to higher dimensions substantial differences appear. In the following sections we will give a taste of higher-dimensional GR; concentrating on solutions, phenomena and techniques relevant for the publications contained in Chs. 2, 3 and 4 of this thesis.

1.1 Black branes

Black branes are black hole solutions with extended directions. The publication in Ch. 2 focuses on stability properties of black p -branes inside a ‘‘cylindrical’’ cavity. Black p -branes treated there are $(n + 3 + p)$ -dimensional solutions to the vacuum Einstein's equations. They are easily obtained by adding p flat directions to the $(n + 3)$ -dimensional Schwarzschild-Tangherlini solution,

$$ds^2 = - \left(1 - \frac{r_0^n}{r^n} \right) dt^2 + \frac{dr^2}{1 - \frac{r_0^n}{r^n}} + r^2 d\Omega_{(n+1)}^2 + \sum_{i=1}^p (dx^i)^2. \quad (1.3)$$

The first three terms in the metric above correspond to the higher-dimensional generalisation of Schwarzschild solution. The only changes in the metric with respect to the four dimensional solution are the change in fall of the gravitational potential $1/r \rightarrow 1/r^n$ and the substitution of the 2-sphere by a $(n + 1)$ -sphere. The last term accounts for the flat spatial extra dimensions. As a result, the black brane is a static solution with the horizon located at $r = r_0$ and with horizon topology $\mathbb{S}^{n+1} \times \mathbb{R}^p$ if the x^i are infinite or $\mathbb{S}^{n+1} \times \mathbb{T}^p$ if they are compactified. Solution (1.3) can also be written as

$$ds^2 = - \left(\eta_{ab} + \frac{r_0^n}{r^n} u_a u_b \right) d\sigma^a d\sigma^b + \frac{dr^2}{1 - \frac{r_0^n}{r^n}} + r^2 d\Omega_{(n+1)}^2 \quad (1.4)$$

making explicit the worldvolume coordinates $\sigma^a = (t, x^i)$ and the worldvolume velocity u^a which satisfies $\eta_{ab}u^a u^b = -1$.

The total mass M and entropy S of these solutions depend on the volume V^p of the space defined by the x^i directions. It is more convenient then to define mass density and entropy density

$$m = \frac{r_0^n (n+1) \Omega_{(n+1)}}{16\pi G}, \quad s = \frac{\Omega_{(n+1)} r_0^{n+1}}{4}. \quad (1.5)$$

Other quantities such as the temperature

$$T = \frac{n}{4\pi r_0}, \quad (1.6)$$

are insensitive to the volume of the flat spatial directions. The Schwarzschild black hole in four dimensions is known to be dynamically stable and locally thermodynamically unstable (negative specific heat). With the quantities above it is easy to check that these black branes also have a negative specific heat and therefore are locally thermodynamically unstable.

In 1993, Ruth Gregory and Raymond Laflamme analysed the dynamic stability of 10 dimensional black p -branes. They found that these black holes are linearly unstable to long wavelength perturbations along their worldvolume [7]. This is known as the Gregory-Laflamme (GL) instability. By perturbing the solution

$$g_{\mu\nu} \rightarrow g_{\mu\nu} + h_{\mu\nu} \quad (1.7)$$

and solving the linearised Einstein's equations³

$$\Delta_L h_{\mu\nu} = 0, \quad (1.8)$$

they found solutions of the form

$$h_{\mu\nu} = e^{\Omega t + i k_i x^i} H_{\mu\nu}(r). \quad (1.9)$$

These are essentially ripples along the horizon (see Fig. 1.1) that grow exponentially with time. They found real and positive values of $\Omega(k)$ for a finite range of k 's from 0 to k_{GL} , see Fig. 1.2. The fact that this instability exists only for wavelengths larger than $\lambda_{GL} = 2\pi/k_{GL}$ means that the brane can be stabilised by choosing the compactification scale smaller than λ_{GL} .

In the original derivation of the GL instability, the dispersion relation for unstable modes (for which we show a sketch in Fig. 1.2) was obtained numerically. Even if the GL instability was first found to be present in 10-dimensional solutions, it is present in neutral black p -branes independently of the number of dimensions (recall that they exist for $D \geq 5$).

All our discussion until now on the GL instability comes from the linearised analysis and little can be said about the endstate of the instability. One can speculate, however, on what can happen if the instability is pursued into the nonlinear

³ Δ_L is known as the Lichnerowicz operator and it is the curved space wave operator for a spin two massless field.

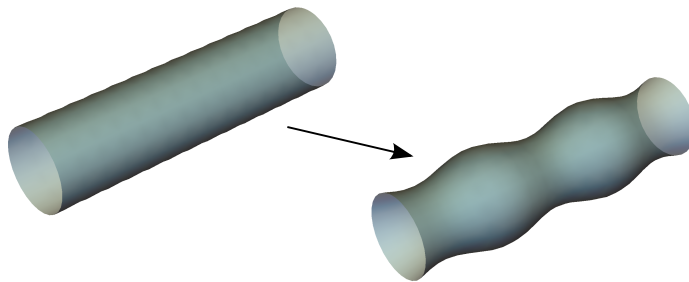


Figure 1.1: Schematic representation of the GL instability effect on a black string horizon.

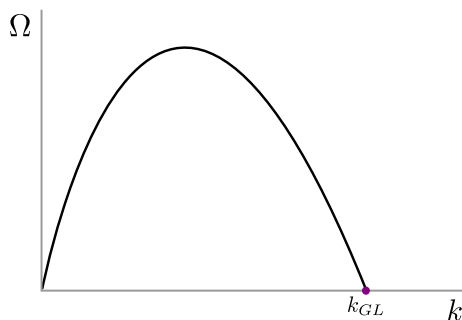


Figure 1.2: Sketch of the dispersion relation $\Omega(k)$ obeyed by unstable GL modes.

regime. It was argued in Ref. [7] that inhomogeneities could keep growing larger and larger until a fragmentation of the black string into localised black holes occurred through a naked singularity. The cosmic censorship hypothesis states that singularities are hidden behind horizons. In higher dimensions, however, it is not believed to be true as situations have been found in which probably naked singularities appear in horizon fragmentation processes of unstable black holes.

The full nonlinear evolution of the homogeneous black string in 5 dimensions was done in 2011 by Luis Lehner and Frans Pretorius [8]. They found the black string inhomogeneities grew to form almost spherical black holes connected by thin necks. Those necks subsequently developed a GL instability; giving as a result an array of localised black holes with smaller black hole satellites in a fractal-like manner. They argued that cosmic censorship was violated by finding that the black string thickness appeared to shrink to zero size in finite asymptotic time. It is now known that this is not the only possible endstate. The GL threshold mode (highlighted with a purple dot in Fig. 1.2) is a static deformation of the black brane horizon which gives rise to a family of solutions named non-uniform black strings (NUBS). There are studies that show the endstate of the GL instability depends strongly on the number of dimensions⁴.

⁴Reference [9] analysed black strings close to the threshold of instability ($L \sim 1/k_{GL}$) and determined that there was a critical dimension $d_{\text{crit}} \approx 13$ that marked two distinct behaviours (for $d > d_{\text{crit}}$ the BS should evolve to a NUBS and for $d < d_{\text{crit}}$ to an array of localised black holes.). Recently it was shown in Ref. [10], by evolving the GR equations in the large number of dimensions limit, that for the strict $d \rightarrow \infty$ limit, the endstate of the evolution is in fact a NUBS. The large d analysis in Ref. [11] recovered the correct value for d_{crit}

A complementary study of the GL instability can be achieved through the blackfold effective worldvolume theory [12, 13]. This approach serves for the study of long wavelength black brane dynamics and for the construction of new black hole solutions with two widely separated scales characterizing their horizon. Some black hole horizons in higher dimensions, for example black branes and some rotating black holes, have two characteristic length scales of very different size. For the black branes discussed here, those lengths correspond to the horizon thickness r_0 and the compactification scales (L^i) of the worldvolume⁵. AF black branes, in which the extended directions are not compactified, will naturally have $r_0 \ll L^i$ since $L^i \approx \infty$. The blackfold effective theory can then be used to study long wavelength ($\sim R \gg r_0$) fluctuations of these solutions. These fluctuations can be intrinsic (thickness variations along the horizon) or extrinsic (bending the worldvolume of the brane). In this thesis we have only treated intrinsic fluctuations.

When such an approach is taken, the complex dynamics of black brane horizons is captured by an effective hydrodynamic theory. That is, whenever the wavelength of the perturbations (let us call them R) along the worldvolume is much larger than the horizon thickness, Einstein's equations in a derivative expansion, are equivalent to the relativistic hydrodynamic equations of an effective fluid. The GL instability within this approach can then be understood as the dynamic instability of a fluid; this is reflected by the imaginary velocity of sound waves through it, *i.e.*, the non propagation of density perturbations.

The black branes discussed here are vacuum solutions to Einstein's equations, which means they have a zero stress-energy tensor. One of the crucial ideas of this approach is to integrate out the short wavelength ($r \ll R$) degrees of freedom captured by the whole geometry and instead describe the system by an effective stress-energy tensor that reproduces the same gravitational field far away ($r \gg r_0$). There are several definitions for such stress-energy tensors but it is better motivated, in the context of the blackfold approach, to use the Brown-York quasilocal stress-energy tensor [14]. For the black brane (1.4) it is that of a perfect fluid

$$T_{ab} = \varepsilon u_a u_b + P P_{ab}, \quad P_{ab} = \eta_{ab} + u_a u_b \quad (1.10)$$

with

$$\varepsilon = (n+1) \frac{\Omega_{n+1} r_0^n}{4G} \quad \text{and} \quad P = -\frac{\Omega_{n+1} r_0^n}{4G}. \quad (1.11)$$

Notice that with this effective perfect fluid description, obtained with the unperturbed black string, one can already realise the presence of an instability⁶. One can see this by introducing small density and velocity perturbations

$$\varepsilon \rightarrow \varepsilon + \delta\varepsilon, \quad P \rightarrow P + \frac{dP}{d\varepsilon} \delta\varepsilon, \quad u^a = (1, \vec{0}) \rightarrow (1, \delta u^i), \quad (1.12)$$

to the static fluid. Then stress-energy conservation gives sound waves

$$\partial_t^2 T^{tt} - \partial_i^2 T^{ii} = 0 \quad \longrightarrow \quad \left(\partial_t^2 - \frac{dP}{d\varepsilon} \partial_i^2 \right) \delta\varepsilon = 0, \quad (1.13)$$

⁵We will consider that all L^i are of the same order.

⁶The equation of motion for the effective stress-energy tensor was derived from Einstein's theory in Ref. [15]. The result shows the effective stress-energy tensor is conserved, $\nabla_a T^{ab} = 0$.

“propagating” with speed

$$c_s^2 = \frac{dP}{d\varepsilon} = -\frac{1}{n+1}. \quad (1.14)$$

The speed is imaginary for the black brane effective fluid and therefore there is no propagation. Instead, density fluctuations grow exponentially with time

$$\delta\varepsilon \sim e^{\Omega t + ik_i x^i}, \quad (1.15)$$

and unstable modes obey the dispersion relation

$$\Omega = \frac{k}{\sqrt{n+1}}. \quad (1.16)$$

Since the density only depends on the horizon radius r_0 , the instability of the fluid shown here corresponds to the hydrodynamic limit of the GL instability present in black branes; *i.e.*, the $k \rightarrow 0$ region of Fig. 1.2.

A further step was taken in Ref. [16]. There, the authors solved Einstein’s equations for a perturbed black brane in which the parameters r_0 and u_a were allowed to slowly vary along the worldvolume,

$$r_0 \rightarrow r_0(\sigma) \quad \text{and} \quad u_a \rightarrow u_a(\sigma). \quad (1.17)$$

The variations considered there are slow compared with the horizon scale r_0 and the equations can then be solved analytically in a derivative expansion. They computed the effective stress-energy tensor of the perturbed black brane. It was seen to be again fluid like, but now with dissipative terms. The perfect fluid part coincided with that of the homogeneous black string and the differences appeared as viscous corrections. The damping effect of viscosity can be appreciated in the corresponding dispersion relation for unstable sound waves

$$\Omega = \sqrt{-c_s^2} k - \left(\left(1 - \frac{1}{p}\right) \frac{\eta}{s} + \frac{\zeta}{2s} \right) \frac{k^2}{T} + \mathcal{O}(k^3), \quad (1.18)$$

where η and ζ are the bulk and shear viscosities respectively. This dispersion relation was compared with numerical results for the GL instability. Surprisingly good agreement was found, see Fig. 1.3, specially when the number of transverse dimensions considered was large. The surprise comes from the fact that the threshold mode of the GL instability is not a hydrodynamic mode, and hence one should not expect it to be captured by the hydrodynamic expansion.

It was proposed by Gubser and Mitra [17], in what has been known as the *correlated stability conjecture* (CSC), that dynamical and thermodynamical instabilities of translationally-invariant black branes are linked. The original statement of the conjecture was:

For a black brane solution to be free of dynamical instabilities, it is necessary and sufficient for it to be locally thermodynamically stable.

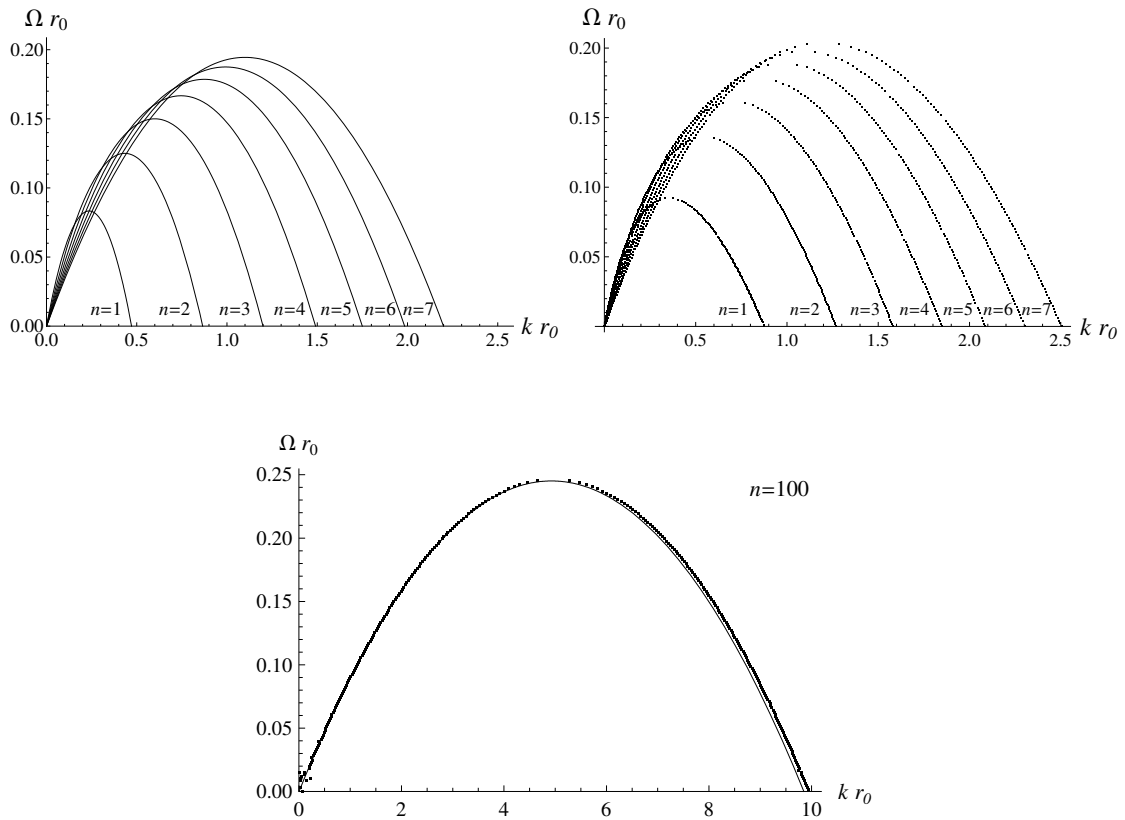


Figure 1.3: At the top left, the dispersion relation $\Omega(k)$ of the effective black brane fluid (1.18). At the top right, numerical data showing the dispersion relation $\Omega(k)$ for unstable GL modes in black branes. At the bottom, both dispersion relations superimposed for the $n = 100$ dimensional case. Images taken from Ref. [16].

The AF black p -branes we have been discussing are always (for all values of r_0 , which is the only parameter of the solution) both thermodynamically and dynamically unstable. This means that they do not violate the conjecture. It would be handy, however, to study a case in which there is a parameter that controls the stability of the solution. Then it could be checked if both dynamical and thermodynamical instabilities appear at the same critical value of the parameter.

In Ref. [18] the thermodynamic stability of the Schwarzschild solution in thermal equilibrium inside a cavity was investigated. The temperature a spherical box of a certain radius (area radius $r = R$) needs to have in order to be in thermal equilibrium with a black hole inside it is the same temperature a local observer at that area radius (in Schw. coordinates at $r = R$) would measure⁷. As a consequence, the temperature of these cavities increases as they are reduced. It was found that the specific heat of Schwarzschild black holes inside such cavities changes from negative to positive as the size of the box decreases. Since the same behaviour persists for black branes in a box, this system serves for the purposes of investigating the CSC with a control parameter. Most of the studies that investigate the validity of the CSC have focused mainly in the static threshold mode of the GL instability. The threshold mode of the black brane inside a cavity was studied in Ref. [19]. There it was shown that the threshold mode disappeared precisely for the size of the cavity that rendered the black brane thermodynamically stable.

There are many systems in which the ranges of the dynamical and thermodynamical instabilities coincide, agreeing then with the CSC. There have been found, however, solutions in which black branes are thermodynamically stable and at the same time exhibit a static zero mode indicating the presence of a dynamical instability.

Chapter 2 contains a publication in which we study the black brane in a cavity using the blackfold approach. We solve Einstein's equations in a derivative expansion imposing Dirichlet boundary conditions at the box. We compute the viscous fluid stress-energy tensor and investigate the stability of sound modes depending on the size of the cavity. There, we argue that the real link is between unstable hydrodynamic modes (usually, but not necessarily, accompanied with a static zero mode) and local thermodynamic instability. This relation is in fact direct in the effective fluid description.

1.2 Flowing horizons

The event horizon of most stationary black holes studied in textbooks and in a vast majority of papers are Killing horizons. Those black hole spacetimes have Killing vector fields $K_{(i)}^\mu$ (let us label them by (i)) which are associated with the symmetries of the solution (generally time translation and axial symmetry). Killing

⁷Notice that this is just taking into account the redshift factor so that $T_R = \frac{T_{\text{Schw}}}{\sqrt{-g_{tt}}}|_{r \rightarrow R}$, where T_{Schw} is the Hawking temperature measured by an asymptotic observer and T_R is the temperature measured by an observer at fixed $r = R$.

vectors obey Killing's equation

$$\nabla_{(\mu} K_{\nu)} = 0 \quad (1.19)$$

and for each Killing vector there is an associated quantity $\epsilon_{(i)}$ which is conserved along geodesics (with tangent vector p^μ)

$$\epsilon_{(i)} = K_{(i)}^\mu p_\mu, \quad p^\mu \nabla_\mu \epsilon_{(i)} = 0. \quad (1.20)$$

A Killing horizon is a null hypersurface Σ whose null generators are parallel to a null Killing vector field. A surface gravity κ can be defined for every Killing horizon as the non-affinity coefficient of the Killing horizon generators⁸

$$K_{(\Sigma)}^\mu \nabla_\mu K_{(\Sigma)}^\nu = -\kappa K_{(\Sigma)}^\nu. \quad (1.21)$$

It can be proven (under some assumptions) that κ is constant on Σ , both along the horizon generators and in the spatial directions orthogonal to them. The surface gravity in stationary horizons can be interpreted as the horizon temperature, hence black holes with Killing horizons have a constant temperature.

In thermodynamics of conventional systems, not all stationary situations are in thermal equilibrium. Consider for example, two infinite heat reservoirs at different temperatures that are connected by a heat conducting bar. The heat flux through the bar will be stationary even though the system is clearly not in thermal equilibrium. In black hole physics, stationary black hole solutions featuring non-Killing horizons can be found⁹. Like in the example of the bar connecting two heat reservoirs, these horizons can support a temperature gradient along them that remains constant in time. Chapter 3 contains a publication in which, inspired by black funnels, we construct analytically such a flowing horizon.

Black funnels are stationary black hole solutions in AdS spacetime which can feature non-Killing horizons. They have a boundary black hole that extends into the bulk in a stringlike manner and that deeper in the bulk merges smoothly with a planar brane; see Fig. 1.4 for a schematic representation. The existence of black funnels was first proposed in the context of AdS/CFT to study strongly coupled field theories in black hole backgrounds. Most of the studies regarding quantum field theories in curved spacetimes had been traditionally addressed with free field theories and it was not clear how much of what we knew was due to the weakly-interacting character of the field theory.

The AdS/CFT correspondence permits (among other things) the study of strongly coupled field theories through their gravity duals. The authors in Ref. [20], with the goal of studying strongly coupled field theories in black hole backgrounds, began examining the possible gravity solutions dual to a black hole immersed in a strongly interacting plasma. In order to accomplish the task they had to seek for AdS solutions that had a black hole at the boundary metric and a planar black

⁸Notice that κ depends on the normalization of the Killing vector. For stationary solutions, however, it is easy to fix the normalization in a sensible way.

⁹There are theorems that say that stationary horizons must be Killing's but these solutions evade those theorems by rendering non-compact horizons.

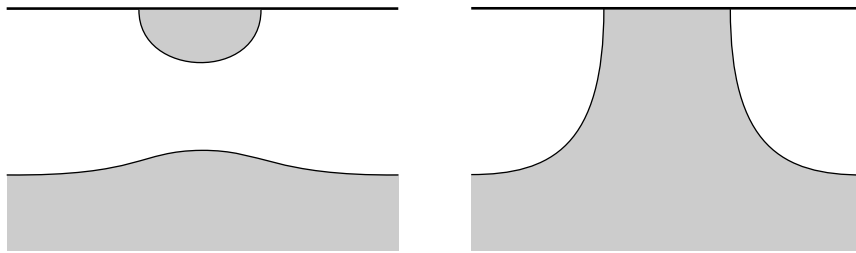


Figure 1.4: Schematic representation of the black droplet over a deformed black brane (left) and the black funnel (right) solutions.

brane asymptotically in the bulk¹⁰. The black hole at the boundary, for continuity of the full solution, had to extend smoothly into the bulk.

Two gravity duals were proposed to exist for such a setting: *black funnels* and *black droplets*¹¹; see Fig. 1.4 for a schematic representation. Both of them feature a black hole metric at the boundary which extends into the bulk. In the case of black droplets the solution contains two disconnected horizons, the droplet that hangs from the boundary and closes up smoothly in the bulk, and a deformed black brane. Black funnels, on the other hand, have one non-compact horizon that merges the black hole at the boundary with a planar brane in the bulk. Black funnel solutions for which the boundary black hole and the asymptotic planar brane are at different temperature exhibit a stationary heat flow along the horizon. This might seem strange but one needs to bear in mind that the boundary metric is a boundary condition for the full solution.

Several black funnels have been constructed over the years. The construction of analytic non-flowing funnels in three and four dimensions was realised in Ref. [23]. Analytic construction of flowing funnels in three dimensions was addressed in Ref. [24]. Numerical non-flowing funnels in five dimensions were found in Ref. [25]. The funnels studied in this last reference, are of the kind depicted in Fig. 1.4 where a stringlike horizon connects smoothly with a planar brane (both having the same temperature). Numerical¹² flowing funnels in global AdS in 4 dimensions were constructed in Ref. [26]. These last funnels have two boundary black holes connected by a tubular horizon through the bulk.

Plenty of work had been done in the field but still a study of a (hot) stringlike horizon merging smoothly with a (cold) planar one was missing. This is precisely the issue addressed in the publication contained in Ch. 3. There we give an analytic construction of a flowing horizon in an arbitrary number of dimensions $d \geq 5$. It features a hot black string freely falling into a cold big black hole. This situation is certainly not stationary unless one considers the limit in which the big black hole is infinitely big. We also show that AdS asymptotics are not necessary for having black hole solutions with non-Killing horizons.

¹⁰The planar brane solution in AdS, was known to be equivalent to a deconfined phase of the strongly coupled field theory in the boundary.

¹¹Black droplets had already been studied in the context of brane worlds [21, 22].

¹²An analytic description was also given in a perturbative analysis.

1.3 Rotating black holes

General collapse situations occurring in nature are expected to end up forming stationary black holes with a certain angular momentum. For vacuum GR in four dimensions the only stationary solution has spherical topology and is given by the Kerr solution

$$ds^2 = - \left(1 - \frac{2Mr}{\rho} \right) dt^2 - \frac{4Mar \sin^2 \theta}{\rho} dt d\phi + \frac{\rho}{\Delta} dr^2 + \rho d\theta^2 + \frac{\sin^2 \theta}{\rho} \left((r^2 + a^2)^2 - a^2 \Delta \sin^2 \theta \right) d\phi^2, \quad (1.22)$$

where

$$\Delta = r^2 - 2Mr + a^2 \quad \text{and} \quad \rho = r^2 + a^2 \cos^2 \theta. \quad (1.23)$$

Kerr solution depends on two parameters, M and a , that correspond respectively to the black hole's mass and angular momentum per unit mass. Its horizons

$$r_{\pm} = M \pm \sqrt{M^2 - a^2}, \quad (1.24)$$

(inner and outer horizons) are found by solving $\Delta(r) = 0$.

There seems to be a maximum value for the amount of angular momentum per unit mass, $a_{\max} = M$, that a solution can have while remaining regular. Notice that beyond this value, for $a > a_{\max}$, the solution does not have a horizon (there is no real solution for $\Delta(r) = 0$) and hence exhibits a naked singularity¹³. The solution with $a = M$ (extremal Kerr) has both horizons coinciding and its associated surface gravity/temperature is equal to zero.

When gravity is extended to higher dimensions, rotating black holes acquire properties only possible in this new setup. The non-trivial higher-dimensional generalisation of Kerr black hole, the Myers-Perry (MP) solution [27], already exhibits some of these. Due to the higher amount of spatial directions, rotating black holes can have several angular momenta; one for every independent rotation plane¹⁴. In this thesis, however, we have restricted ourselves to the investigation of black holes with a single spin.

Other new features of gravity in higher dimensions are *non-uniqueness*, *i.e.*, the fact that more than one solution is possible for the same asymptotic charges and the possibility of stationary AF vacuum solutions with *non-spherical horizon topology*. The first example of black hole non-uniqueness and non-spherical horizon topology was the five dimensional rotating black ring [28]. The black ring is a black hole solution whose event horizon has a $\mathbb{S}^1 \times \mathbb{S}^2$ topology and rotates along the \mathbb{S}^1 in order to sustain itself. For a certain range of masses and angular momenta three solutions were shown to be compatible: two different black rings and a MP black hole.

¹³The bound on the maximum amount of angular momentum per unit mass that a black hole can have is known as the Kerr bound. The existence of this bound, as we will see, depends on the number of dimensions.

¹⁴This is the same as saying that the rank of the group of rotations increases with the number of dimensions.

Further investigation along these lines led to the construction of black saturns [29] (black ring with a black hole in the middle), di rings [30] (two concentric black rings), doubly spinning black rings [31] (black ring with two angular momentum), etc. Even if the mentioned solutions were constructed originally in five dimensions, there were good arguments, together with blackfold constructions, to believe that these and other solutions, with more intricate topologies, existed also in higher dimensions.

Non-uniqueness was found to be a characteristic feature of gravity higher dimensions and its “discovery” raised many questions: *What is the final state in a dynamical collapse situation if the final mass and angular momentum are compatible with several black holes? Are some of the solutions unstable? Is cosmic censorship violated in these setups? Which is the thermodynamically preferred solution? Are there intermediate stationary black hole solutions connecting between the known solutions?* Most of these questions have been addressed over the years in the literature and we have also dealt with some of them in the publication contained in Ch. 4. In particular, we constructed stationary black hole solutions in six dimensions that connect (in the space of single spin stationary solutions) between MP black holes and black rings, black saturns and di rings; we have also studied their stability properties. In order to motivate their existence, let us begin with the single spin MP black hole in d dimensions

$$ds^2 = -dt^2 + \frac{\mu}{r^{d-5}\rho} (dt - a \sin^2 \theta d\phi)^2 + \frac{\rho}{\Delta} dr^2 + \rho d\theta^2 + (r^2 + a^2) \sin^2 \theta d\phi^2 + r^2 \cos^2 \theta d\Omega_{(d-4)}^2, \quad (1.25)$$

with

$$\Delta = r^2 + a^2 - \frac{\mu}{r^{d-5}} \quad \text{and} \quad \rho = r^2 + a^2 \cos^2 \theta. \quad (1.26)$$

The first thing to notice is that $\Delta = 0$ has always one real and positive solution for $d \geq 6$ if $\mu > 0$. Intuitively, this change comes from the fact that the centrifugal barrier (as it refers to motion in a plane) does not depend on the number of dimensions while the gravitational potential does. As opposed to the four dimensional counterpart, there is no longer a Kerr bound. For very large a we can always find a small enough $r = r_h$ that gives the horizon position

$$r_h \approx \left(\frac{\mu}{a^2} \right)^{1/(d-5)}. \quad (1.27)$$

MP black holes in the ultraspinning regime are then characterised by two very different lengths

$$\ell_{\parallel} \sim a \quad \text{and} \quad \ell_{\perp} \sim r_h \approx \left(\frac{\mu}{a^2} \right)^{1/(d-5)}. \quad (1.28)$$

One of these lengths, ℓ_{\parallel} , is the invariant radius of the rotating \mathbb{S}^1 . The other, ℓ_{\perp} , is the invariant radius of the (transverse to rotation) \mathbb{S}^{d-4} . The horizon of ultraspinning MP black holes is then pancaked, see Fig. 1.5. It extends in the rotation plane and contracts in the directions perpendicular to it. The area of these horizons vanishes as $a \rightarrow \infty$. This might seem surprising because they can extend arbitrarily in the rotation plane. Notice, however, that the small radius of

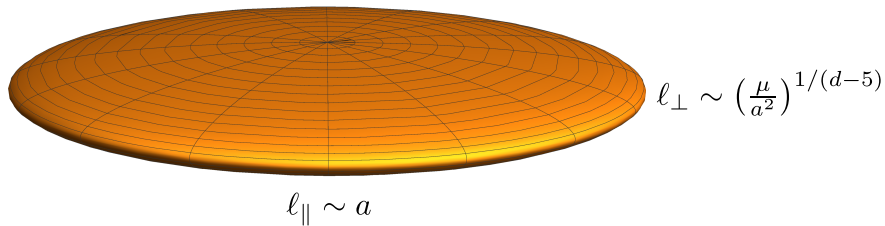


Figure 1.5: Schematic representation of the pancaked horizon of ultraspinning MP black holes. The horizon expands in the direction parallel to the rotation plane and shrinks in the direction perpendicular to the rotation plane. That is $\ell_{\parallel} \gg \ell_{\perp}$.

the \mathbb{S}^{d-4} contributes more to the horizon area than the arbitrarily large radius of the \mathbb{S}^1 . Notice also that these black holes have a very large angular momentum per unit mass due to the fact that they are very extended in the rotation plane and not due to a very fast rotation. In fact, their angular velocity goes to zero as $a \rightarrow \infty$; in turn, their metric close to the rotation axis is that of a black brane.

It was argued in Ref. [32] that ultraspinning MP black holes are unstable. So even if for $d \geq 6$ there is no bound on the angular momentum, the conjectured instability acts as a dynamical decay mechanism, thus providing an effective Kerr bound. Since ultraspinning MP black holes are similar to black branes, the conjectured instability was of GL type, *i.e.*, ripples along the horizon. In this case, since the horizon is rotating and compact, the GL-like instability would have two main differences: it should respect the axial symmetry and it would arise for specific wavelengths (the ones that fit in the compact horizon). Reference [32] also proposed that these black holes could suffer of non-axisymmetric instabilities known as bar-mode instabilities. Both axisymmetric and bar-mode instabilities have been investigated numerically in Refs. [33–36] and it has been found that bar-mode instabilities are present for lower values of the angular momentum than axisymmetric ones. These two instabilities are of different nature. Axisymmetric instabilities can give rise to new stationary solutions while non-axisymmetric ones, due to the emission of gravitational radiation, can not.

These new axisymmetric solutions, which in Ch. 4 we call *bumpy black holes*, branch off the MP solution in the space of stationary solutions (see Fig. 1.6). The point labelled by a $\mathbf{0}$ marks the beginning of the ultraspinning regime. At this point and for larger J the moment of inertia becomes negative. References [33, 34] found the specific values of J at which branching points \mathbf{A} , \mathbf{B} , \mathbf{C} occurred. This was done numerically for $6 \leq d \leq 11$ through a perturbative study. They also found the shape of the perturbation associated to each of the modes. This confirmed that the new families of solutions connect the MP branch with the black ring, black saturn, etc. Notice that there is an infinite number of these branching points as J is increased. The first branch of bumpy black holes as well as the black ring in six and seven dimensions were constructed numerically in Ref. [37]. This first branch is the one that connects the MP and the black ring in the space of stationary solutions¹⁵. It came as a surprise, though it should have been expected,

¹⁵Notice that the fact that different branches are connected in the space of stationary solutions, does not mean that a dynamical evolution will follow such paths.

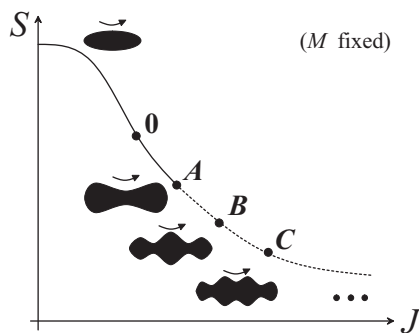


Figure 1.6: Sketch of the S (entropy) vs. J (angular momentum) for fixed mass M for the MP black hole in $d \geq 6$. The first point that appears in the curve, labelled with a $\mathbf{0}$, corresponds to the point at which the MP black hole enters the ultraspinning regime. The following points, labeled by \mathbf{A} , \mathbf{B} , \mathbf{C} , etc. correspond to branching points due to the GL-like instability. Figure was taken from Ref. [33].

that two branches of different bumpy black holes emerged from that branching point. At the linearised level, close to the branching point, these new solutions are obtained just by considering the perturbation with the opposite sign. While the endstate of the (+)-branch¹⁶ was clear, little was known about the how other solutions (consequently we will refer to these as the (-)-branches) evolved in solution space.

The publication contained in Ch. 4 goes in a similar direction. We construct numerically the first three branches of bumpy black holes, both the (+) and the (-), in six dimensions. In order to construct them we solve Einstein-DeTurck's equations

$$R_{\mu\nu}^H = R_{\mu\nu} - \nabla_{(\mu}\xi_{\nu)} = 0, \quad \xi^\mu = g^{\alpha\beta}(\Gamma_{\mu\nu}^\alpha - \bar{\Gamma}_{\mu\nu}^\alpha) \quad (1.29)$$

subject to specific boundary conditions. Here $R_{\mu\nu}^H$ is the Einstein-DeTurck tensor, ξ is the DeTurck vector and $\bar{\Gamma}$ is a reference connection compatible with a reference metric $\bar{g}_{\mu\nu}$ that needs to satisfy the same boundary conditions as the actual metric $g_{\mu\nu}$. The reason for using these equations instead of the usual Ricci flat equations ($R_{\mu\nu} = 0$) is that these have been shown to be elliptic for a class of Lorentzian stationary metrics (with horizons and ergospheres) [38] into which bumpy black holes fall. Since these equations are elliptic, one can then use standard numerical techniques to solve boundary value problems. Notice that there might be solutions to Einstein-DeTurck's equations which are not Ricci-flat, these are called Ricci solitons. Since we were not interested in them, after solving Einstein-DeTurck's equations we checked that the DeTurck vector vanished.

In Ch. 4 we extend the (+) and (-) branches very far in deformation and analyse the changes in the horizon geometry. This allows us to confirm the expected presence of cone-like geometries close to the pinch-off for the (+)-branches [39, 40]. On the other hand we explain that (-)-branches probably end as singular solutions not connecting to any known black holes. We study and discuss their stability properties. In order to do that we compute the spectrum of the Lichnerowicz

¹⁶From now on we will refer to the bumpy solutions that connect to other known families of rotating black holes as (+)-branches.

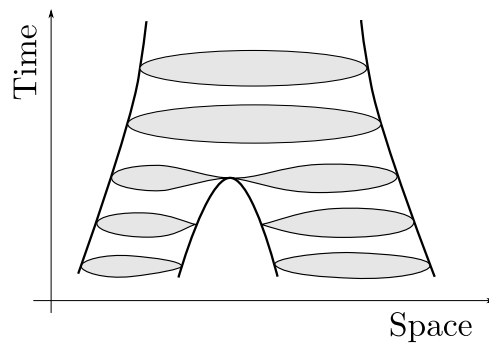


Figure 1.7: Sketch of a null surface representing the event horizon of a black hole merger. Constant time slices are highlighted.

operator and look for negative eigenvalues. We also compute the specific heat and the moment of inertia and check that the number of negative eigenvalues matches the expected value according to the known instabilities.

1.4 Black hole mergers

The direct detection of gravitational waves by LIGO [41] showed that black hole mergers occur in Nature. A black hole merger is an event in which two black holes fuse into one. Black hole spacetimes are characterised by having an event horizon, which is a null hypersurface in spacetime. In a four dimensional spacetime the event horizon is a three dimensional null hypersurface and is traced by a two-parameter family of null geodesics. In a spacetime in which two black holes merge, constant time slices of the event horizon contain two disconnected spatial surfaces in the asymptotic past; posterior constant time slices describe how the two disconnected surfaces merge with one another, see Fig. 1.7.

The null geodesics that generate the horizon are the light rays in a black hole spacetime that mark the boundary between light rays that reach null asymptotic infinity and those that do not. For static and stationary solutions, such as Schwarzschild's and Kerr's, the event horizon is a Killing horizon¹⁷ and its generators are Killing vectors. Future and past developments of such generators never abandon the horizon hypersurface.

In more general spacetimes, with no timelike Killing vectors, the horizons are not Killing horizons. The future development of the generators of the null hypersurface will however still stay in the horizon. In merger horizons there will in general be points in the hypersurface, named *caustic points*, through which null rays enter the horizon; hence the past development of some generators does not belong to the horizon. In Fig. 1.8 we show a sketch of the event horizon of a head on collision of two black holes. There we highlight the presence of a caustic line (thick dark red curve, collection of caustic points) through which some generators (red curves) enter the hypersurface.

¹⁷Killing horizons are discussed in Sec. 1.2

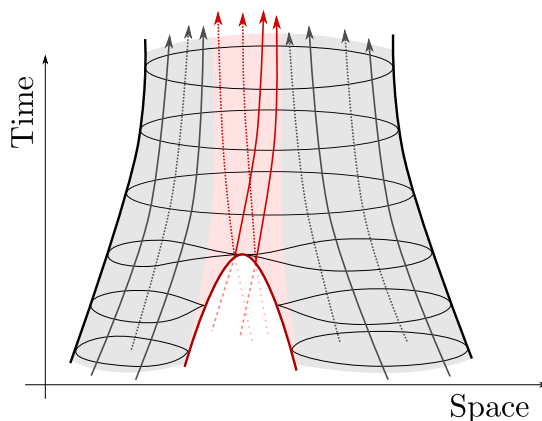


Figure 1.8: Sketch of null surface representing the event horizon of a black hole merger. Dark grey curves indicate horizon generators that have always belonged to the horizon. Red curves, on the other hand, indicate generators that have entered the horizon at some point in spacetime through a caustic line (thick dark red curve).

Dynamical situations are in general complicated and numerical computations are usually unavoidable. The first step, defining the initial data, is already a hard problem. Afterwards, the system is evolved by solving nonlinearly Einstein’s equations; this demands a huge amount of computational resources and sophisticated numerical techniques. Once the spacetime solution is obtained, it is analysed in the far future, where the system has reached a practically stationary situation (if the evolution has run for long enough). The light rays belonging to a practically stationary event horizon are then identified. In order to obtain the event horizon of the merger, those light rays are then propagated back in time through the previously computed numerical spacetime.

Notice that the event horizon is defined from future to past; this fact has curious repercussions in its features. In dynamical situations involving mergers, conical structures appear in the constant time slices of the event horizon even when the two original black holes are very far apart. The presence of caustics, a characteristic feature in these horizons, is the reason for the appearance of such cones.

Black hole mergers have been traditionally treated within the field of numerical relativity and it might seem that there is no hope for an analytic description of a black hole merger. There is however one limiting — but still realistic — instance in which the event horizon of the merger of a black hole binary becomes so simple that it can be described in an exact analytic way. This is precisely the work contained in the publication in Ch. 5. Our limiting construction, furthermore, only involves elementary techniques and ideas that lie at the core of GR and have been well understood for many decades: the Equivalence Principle, the Schwarzschild solution and its null geodesics, and the notion of Event Horizon.

The limit we consider is that of extreme-mass ratio (EMR) in which one black hole is much smaller than the other. Given the findings of Ref. [41], it does seem possible that black hole binary mergers with mass ratios $\lesssim 1/30$ will be detected in ground-based observatories — and with much smaller ratios in space-based ones.

The EMR limit is often taken as one where the size of the large black hole, M ,

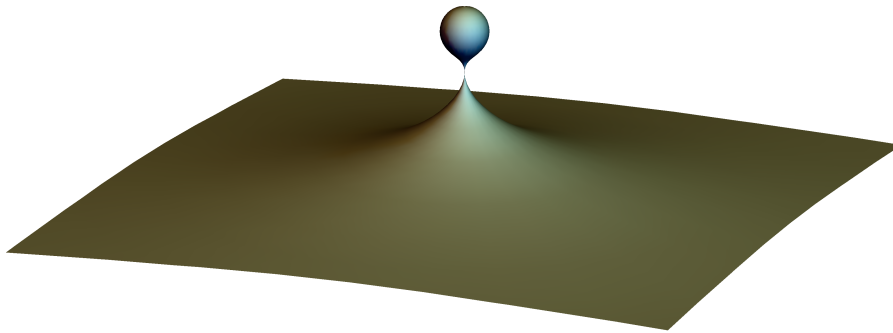


Figure 1.9: 3D plot for pinch-on instant of the event horizon computed in Ch. 5. This image has been generated from analytic results for the exact EMR merger.

is fixed; while the small black hole is regarded as a point-like object of size $m \rightarrow 0$. This is appropriate for extracting the gravitational waves from the collision (with wavelengths $\sim M$), but not details on the scale of m , such as the event horizon when the two black holes fuse with each other. For this, we must keep m fixed while $M \rightarrow \infty$. As a result, in our construction, gravitational radiation decouples and fine details of the horizon hypersurface, such as caustic structure, generators, relaxation time scales, etc., are exactly captured. See Fig. 1.9 for a constant time slice of the event horizon we have constructed. This constant time slice is precisely that of the pinch-on instant. It is important to stress that Fig. 1.9 has been generated from the analytic expressions.

Consider now the last moments before the merger, *i.e.*, when the small black hole is at a distance $\ll M$ from the large one. The equivalence principle asserts that we can always place ourselves in the rest frame of the small black hole, and that the curvature of the large black hole can be neglected over distances much smaller than M . The spacetime around the small black hole should be then well approximated by the Schwarzschild geometry [42]. Although the curvature created by the large black hole vanishes in this limit, its horizon is still present: it becomes an infinite, Rindler-type, acceleration horizon that reaches asymptotic null infinity as a planar null surface. Therefore, in the EMR limit on scales much smaller than M , the event horizon of the black hole merger can be found by tracing in the Schwarzschild geometry a family of null geodesics that approach a planar horizon at a large distance from the small black hole.

The publication in Ch. 5 contains the construction of the event horizon of such a setting. The results are obtained by capturing the appropriate family of null geodesics in Schwarzschild solution. We extract a number of parameters that characterise the merger. We identify the line of caustics, the critical radius at which both horizons touch, the critical growth of the throat formed just after the two horizon touch, etc.

The equivalence principle — Einstein’s first and firmest intuition about gravity — lies at the heart of General Relativity. A notion so deep is not easily exhausted even after a century of use. In a beautiful sleight of hand, it has allowed us to accurately capture a phenomenon that involves two black holes, using a geometry that seemingly would contain only one.

REFERENCES

- [1] J. D. Bekenstein, “Black holes and entropy,” *Phys. Rev.* **D7** (1973) 2333–2346.
- [2] S. W. Hawking, “Particle Creation by Black Holes,” *Commun. Math. Phys.* **43** (1975) 199–220. [[167\(1975\)](#)].
- [3] S. W. Hawking, “Breakdown of Predictability in Gravitational Collapse,” *Phys. Rev.* **D14** (1976) 2460–2473.
- [4] A. Strominger and C. Vafa, “Microscopic origin of the Bekenstein-Hawking entropy,” *Phys. Lett.* **B379** (1996) 99–104, [arXiv:hep-th/9601029](#) [[hep-th](#)].
- [5] R. Emparan and H. S. Reall, “Black Holes in Higher Dimensions,” *Living Rev. Rel.* **11** (2008) 6, [arXiv:0801.3471](#) [[hep-th](#)].
- [6] T. Kaluza, “On the Problem of Unity in Physics,” *Sitzungsber. Preuss. Akad. Wiss. Berlin (Math. Phys.)* **1921** (1921) 966–972.
- [7] R. Gregory and R. Laflamme, “Black strings and p-branes are unstable,” *Phys. Rev. Lett.* **70** (1993) 2837–2840, [arXiv:hep-th/9301052](#) [[hep-th](#)].
- [8] L. Lehner and F. Pretorius, “Final State of Gregory-Laflamme Instability,” [arXiv:1106.5184](#) [[gr-qc](#)].
- [9] E. Sorkin, “A Critical dimension in the black string phase transition,” *Phys. Rev. Lett.* **93** (2004) 031601, [arXiv:hep-th/0402216](#) [[hep-th](#)].
- [10] R. Emparan, R. Suzuki, and K. Tanabe, “Evolution and End Point of the Black String Instability: Large D Solution,” *Phys. Rev. Lett.* **115** no. 9, (2015) 091102, [arXiv:1506.06772](#) [[hep-th](#)].
- [11] R. Suzuki and K. Tanabe, “Non-uniform black strings and the critical dimension in the $1/D$ expansion,” *JHEP* **10** (2015) 107, [arXiv:1506.01890](#) [[hep-th](#)].
- [12] R. Emparan, T. Harmark, V. Niarchos, and N. A. Obers, “World-Volume Effective Theory for Higher-Dimensional Black Holes,” *Phys. Rev. Lett.* **102** (2009) 191301, [arXiv:0902.0427](#) [[hep-th](#)].
- [13] R. Emparan, T. Harmark, V. Niarchos, and N. A. Obers, “Essentials of Blackfold Dynamics,” *JHEP* **03** (2010) 063, [arXiv:0910.1601](#) [[hep-th](#)].
- [14] J. D. Brown and J. W. York, Jr., “Quasilocal energy and conserved charges derived from the gravitational action,” *Phys. Rev.* **D47** (1993) 1407–1419, [arXiv:gr-qc/9209012](#) [[gr-qc](#)].
- [15] J. Camps and R. Emparan, “Derivation of the blackfold effective theory,” *JHEP* **03** (2012) 038, [arXiv:1201.3506](#) [[hep-th](#)]. [Erratum: *JHEP*06,155(2012)].
- [16] J. Camps, R. Emparan, and N. Haddad, “Black Brane Viscosity and the Gregory-Laflamme Instability,” *JHEP* **05** (2010) 042, [arXiv:1003.3636](#) [[hep-th](#)].

- [17] S. S. Gubser and I. Mitra, “The Evolution of unstable black holes in anti-de Sitter space,” *JHEP* **08** (2001) 018, [arXiv:hep-th/0011127](#) [hep-th].
- [18] J. W. York, Jr., “Black hole thermodynamics and the Euclidean Einstein action,” *Phys. Rev.* **D33** (1986) 2092–2099.
- [19] J. P. Gregory and S. F. Ross, “Stability and the negative mode for Schwarzschild in a finite cavity,” *Phys. Rev.* **D64** (2001) 124006, [arXiv:hep-th/0106220](#) [hep-th].
- [20] V. E. Hubeny, D. Marolf, and M. Rangamani, “Hawking radiation in large N strongly-coupled field theories,” *Class. Quant. Grav.* **27** (2010) 095015, [arXiv:0908.2270](#) [hep-th].
- [21] A. Chamblin, S. W. Hawking, and H. S. Reall, “Brane world black holes,” *Phys. Rev.* **D61** (2000) 065007, [arXiv:hep-th/9909205](#) [hep-th].
- [22] R. Emparan, R. Gregory, and C. Santos, “Black holes on thick branes,” *Phys. Rev.* **D63** (2001) 104022, [arXiv:hep-th/0012100](#) [hep-th].
- [23] V. E. Hubeny, D. Marolf, and M. Rangamani, “Hawking radiation in large N strongly-coupled field theories,” *Class. Quant. Grav.* **27** (2010) 095015, [arXiv:0908.2270](#) [hep-th].
- [24] S. Fischetti and D. Marolf, “Flowing Funnel: Heat sources for field theories and the AdS_3 dual of CFT_2 Hawking radiation,” *Class. Quant. Grav.* **29** (2012) 105004, [arXiv:1202.5069](#) [hep-th].
- [25] J. E. Santos and B. Way, “Black Funnel,” *JHEP* **12** (2012) 060, [arXiv:1208.6291](#) [hep-th].
- [26] S. Fischetti, D. Marolf, and J. E. Santos, “AdS flowing black funnels: Stationary AdS black holes with non-Killing horizons and heat transport in the dual CFT,” *Class. Quant. Grav.* **30** (2013) 075001, [arXiv:1212.4820](#) [hep-th].
- [27] R. C. Myers and M. J. Perry, “Black Holes in Higher Dimensional Space-Times,” *Annals Phys.* **172** (1986) 304.
- [28] R. Emparan and H. S. Reall, “A Rotating black ring solution in five-dimensions,” *Phys. Rev. Lett.* **88** (2002) 101101, [arXiv:hep-th/0110260](#) [hep-th].
- [29] H. Elvang and P. Figueras, “Black Saturn,” *JHEP* **05** (2007) 050, [arXiv:hep-th/0701035](#) [hep-th].
- [30] H. Iguchi and T. Mishima, “Black di-ring and infinite nonuniqueness,” *Phys. Rev.* **D75** (2007) 064018, [arXiv:hep-th/0701043](#) [hep-th]. [Erratum: *Phys. Rev.* **D78**, 069903(2008)].
- [31] A. A. Pomeransky and R. A. Sen’kov, “Black ring with two angular momenta,” [arXiv:hep-th/0612005](#) [hep-th].
- [32] R. Emparan and R. C. Myers, “Instability of ultra-spinning black holes,” *JHEP* **09** (2003) 025, [arXiv:hep-th/0308056](#) [hep-th].
- [33] O. J. C. Dias, P. Figueras, R. Monteiro, J. E. Santos, and R. Emparan, “Instability and new phases of higher-dimensional rotating black holes,” *Phys. Rev.* **D80** (2009) 111701, [arXiv:0907.2248](#) [hep-th].
- [34] O. J. C. Dias, P. Figueras, R. Monteiro, and J. E. Santos, “Ultraspinning instability of rotating black holes,” *Phys. Rev.* **D82** (2010) 104025, [arXiv:1006.1904](#) [hep-th].

- [35] M. Shibata and H. Yoshino, “Nonaxisymmetric instability of rapidly rotating black hole in five dimensions,” *Phys. Rev.* **D81** (2010) 021501, [arXiv:0912.3606](#) [gr-qc].
- [36] M. Shibata and H. Yoshino, “Bar-mode instability of rapidly spinning black hole in higher dimensions: Numerical simulation in general relativity,” *Phys. Rev.* **D81** (2010) 104035, [arXiv:1004.4970](#) [gr-qc].
- [37] O. J. C. Dias, J. E. Santos, and B. Way, “Rings, Ripples, and Rotation: Connecting Black Holes to Black Rings,” *JHEP* **07** (2014) 045, [arXiv:1402.6345](#) [hep-th].
- [38] A. Adam, S. Kitchen, and T. Wiseman, “A numerical approach to finding general stationary vacuum black holes,” *Class. Quant. Grav.* **29** (2012) 165002, [arXiv:1105.6347](#) [gr-qc].
- [39] B. Kol, “Topology change in general relativity, and the black hole black string transition,” *JHEP* **10** (2005) 049, [arXiv:hep-th/0206220](#) [hep-th].
- [40] R. Emparan and N. Haddad, “Self-similar critical geometries at horizon intersections and mergers,” *JHEP* **10** (2011) 064, [arXiv:1109.1983](#) [hep-th].
- [41] **Virgo, LIGO Scientific** Collaboration, B. P. Abbott *et al.*, “Observation of Gravitational Waves from a Binary Black Hole Merger,” *Phys. Rev. Lett.* **116** no. 6, (2016) 061102, [arXiv:1602.03837](#) [gr-qc].
- [42] K. Schwarzschild, “On the gravitational field of a mass point according to Einstein’s theory,” *Sitzungsber. Preuss. Akad. Wiss. Berlin (Math. Phys.)* **1916** (1916) 189–196, [arXiv:physics/9905030](#) [physics].

Collection of Articles

BLACK BRANES IN A BOX: HYDRODYNAMICS, STABILITY, AND CRITICALITY

This chapter contains the publication:

- R. Emparan and M. Martinez,
“Black Branes in a Box: Hydrodynamics, Stability, and Criticality,”
JHEP **1207**, 120 (2012), [arXiv:1205.5646 \[hep-th\]](#).

Black branes in a box: hydrodynamics, stability, and criticality

Roberto Emparan^{a,b} and Marina Martínez^b

^a*Institució Catalana de Recerca i Estudis Avançats (ICREA),
Passeig Lluís Companys 23, E-08010 Barcelona, Spain*

^b*Departament de Física Fonamental and Institut de Ciències del Cosmos, Universitat de Barcelona,
Martí i Franquès 1, E-08028 Barcelona, Spain*

E-mail: emparan@ub.edu, marinamartinez89@gmail.com

ABSTRACT: We study the effective hydrodynamics of neutral black branes enclosed in a finite cylindrical cavity with Dirichlet boundary conditions. We focus on how the Gregory-Laflamme instability changes as we vary the cavity radius R . Fixing the metric at the cavity wall increases the rigidity of the black brane by hindering gradients of the redshift on the wall. In the effective fluid, this is reflected in the growth of the squared speed of sound. As a consequence, when the cavity is smaller than a critical radius the black brane becomes dynamically stable. The correlation with the change in thermodynamic stability is transparent in our approach. We compute the bulk and shear viscosities of the black brane and find that they do not run with R . We find mean-field theory critical exponents near the critical point.

KEYWORDS: p-branes, Black Holes, Black Holes in String Theory

ARXIV EPRINT: [1205.5646](https://arxiv.org/abs/1205.5646)

Contents

1	Introduction and conclusions	1
2	Static black brane in a cylindrical cavity	4
2.1	Geometry	4
2.2	Physical magnitudes	5
2.3	No subtraction required	6
3	Fluctuating black brane	6
4	Hydrodynamics and stability	9
4.1	Perfect fluid dynamics	9
4.2	Black brane hydrodynamics	9
4.3	Correlated dynamical and thermodynamic stability	12
5	Viscous hydrodynamics	12
5.1	Bulk and shear viscosities do not run	12
5.2	Spectrum of unstable modes	13
5.3	Critical behavior	14
A	Solution with finite-cavity boundary conditions	16
B	Connection on the wall	18

1 Introduction and conclusions

The complex non-linear dynamics of black holes and black branes, governed by Einstein's equations, can in some regimes be efficiently captured by an effective theory for collective degrees of freedom. Some of these degrees of freedom are worldvolume embedding coordinates, associated to the elastic dynamics characteristic of brane-like objects, but there are also hydrodynamic degrees of freedom — e.g., pressure and velocity — associated to horizon dynamics. The hydrodynamic approach dates back to [1] and has been greatly extended following the fluid/gravity correspondence of [2]. In the context of asymptotically flat black branes, it features within the effective blackfold theory of [3–5]. A framework for relating all these approaches is presented in [6].

Here we are interested in using the hydrodynamic methods for investigating a peculiar effect of black branes: the classical instability of their horizons to the formation of ripples along their worldvolume, discovered by Gregory and Laflamme in [7]. Refs. [4, 8] have shown how this phenomenon is very neatly captured in the hydrodynamic theory of blackfolds: it is simply an instability of fluctuations of the pressure of the effective black

brane fluid, i.e., a sound-mode instability. In this paper we investigate it further by introducing an additional parameter to gain control over the stability of the system. To do so, we place the black brane inside a finite cylindrical cavity of fixed radius R . Then we find the solution for a fluctuating black brane, with regularity conditions at the horizon, in the hydrodynamic limit. We analyze how the effective black brane theory, in particular its stability under hydrodynamic fluctuations, changes as the cavity radius R is varied. This allows us to study several issues:

Correlated instabilities — ghosts vs. tachyons. One reason to expect that enclosing the black brane in a cavity should have an effect on its stability comes from the Correlated Stability Conjecture (CSC) [9], which links classical dynamical stability to local thermodynamical stability. Since it is known that the specific heat of the black brane in a cavity changes from negative for cavity radii greater than a critical value, $R > R_c$, to positive when $R < R_c$ [10], the validity of the conjecture requires that the Gregory-Laflamme instability of the black brane disappears at the critical radius $R = R_c$.

To put our study in the right context, it is worth discussing the status and proper interpretation of the CSC. This has often been taken as the statement that

- (CSC:) translationally invariant horizons have a tachyonic perturbation mode if and only if they are locally thermodynamically unstable.

Indeed, a large part of the studies of the CSC have focused on the presence or absence of a static, zero-mode perturbation of finite wavelength (a tachyon) that would mark the onset of the instability [11, 12]. In particular, ref. [13] studied the static zero-mode for the black brane in a cavity and showed that it disappears precisely when the cavity size reaches $R = R_c$.

This form of the CSC, however, is incorrect: examples of black branes are known which are thermodynamically stable but nevertheless have tachyonic instabilities [15]. Instead, the local thermodynamical stability of black branes is more appropriately related to the presence of massless *ghost* excitations, rather than tachyons. These two kinds of unstable modes are quite different. For excitations that in some range of wavenumbers k have a dispersion relation approximately of the type

$$\omega^2 = c^2 k^2 + m^2, \tag{1.1}$$

we say we have a tachyon when $m^2 < 0$. The static zero-mode corresponds to $k = k_0 = \sqrt{-m^2/c^2}$ and $\omega = 0$. Instead, we say we have a ghost when $c^2 < 0$, and in particular a massless ghost has $\Omega = \text{Im } \omega = \sqrt{-c^2} k$.

The argument why thermodynamical instabilities of a translation-invariant horizon are connected to massless ghosts is simple [4, 14, 15]. A horizon that is translationally invariant can support perturbations of arbitrarily long wavelength. In the cases where the frequency of these perturbations vanishes as the wavelength diverges, they are hydrodynamic modes, which are either fluctuations of conserved quantities or Goldstone modes. Both of them feature in the local thermodynamics of the fluid. In the case of main interest to us here, the conserved quantity is the energy, and it is an old result (which we reproduce in section 4

below) that small fluctuations in the energy density propagate along the fluid with squared velocity

$$v_s^2 = \frac{s}{C_V}, \quad (1.2)$$

where s is the entropy density of the fluid and C_V its specific heat at fixed volume. Obviously, a local thermodynamic instability, with $C_V < 0$, results in unstable perturbations of wavenumber k whose amplitude grows exponentially in time like $\exp(\sqrt{-v_s^2} kt)$. More generally, any local thermodynamic instability of the black brane gives rise to a long-wavelength, hydrodynamic instability. In the terms used above, we have a massless ghost with $c^2 = v_s^2 < 0$.

Then, the CSC as stated above must be replaced by a statement of *Correlated Hydrodynamic Stability*:

- (CHS:) translationally invariant horizons have massless ghost excitations if and only if they are locally thermodynamically unstable. The ghost is a long-wavelength, low imaginary frequency, hydrodynamic instability of the horizon.

Since horizons are stable to fluctuations of very short wavelength,¹ the ghost instability at small k must disappear at some larger $k = k_0 > 0$, i.e., $\text{Im}\omega(k_0) = 0$. If also $\text{Re}\omega(k_0) = 0$, then this is a zero-mode. In other words, a hydrodynamic ghost instability (and hence a local thermodynamic instability) of the horizon will typically be accompanied by a tachyonic zero-mode at finite k . This is indeed the case for the GL instability of neutral black branes (also when in a cavity). But the converse need not be true: a tachyonic instability need not turn into a hydrodynamic ghost instability at very long wavelengths,² and hence need not be related to a local thermodynamic instability.

In this paper we construct explicitly the ghost, hydrodynamic unstable perturbation of the black brane in a cavity, and show that it turns into an oscillatory (damped) sound wave when $R < R_c$.

Increasing rigidity. Our analysis of the effective hydrodynamic theory also gives a concrete intuitive picture of why and how the instability disappears as the cavity size is reduced. The squared speed of sound of the effective theory at finite R is a monotonic increasing function of decreasing R . A larger speed of sound reflects a higher rigidity of the system. This comes about because fixing the metric on the cavity wall at finite R makes it harder for the geometry to fluctuate, and in particular prevents the creation of worldvolume gradients of the redshift on the wall. In the hydrodynamic theory, these gradients have the effect of an acceleration of the fluid that opposes the creation of inhomogeneities along the worldvolume. This works to make the system more rigid and therefore less unstable, until the instability disappears.

Viscosities do not run with R . The solution for the spacetime metric for a fluctuating black brane in a cavity of radius R , to first-derivative order in the fluctuations, allows us

¹On very short scales the horizon is indistinguishable from Minkowski space, which in any healthy gravitational theory is stable at sufficiently short wavelengths.

²For instance, it can become a homogeneous tachyonic mode with $\text{Im}\omega(k=0) = \sqrt{-m^2}$.

to compute the stress-energy tensor of the effective fluid including dissipative effects. The values we obtain for the shear and bulk viscosities (and for their ratios to the entropy density) are *the same at all values of R* . This is very likely related to a similar result obtained in the context of black branes in AdS₅ in [16], and may be a feature of a larger class of black branes.

Spectrum and criticality. The inclusion of dissipative terms in the fluid equations gives us an improved approximation for the spectrum of unstable modes. The dispersion curves show clearly that the instability weakens as the critical point is approached. Although the hydrodynamical theory cannot capture all the physics of the critical state, it nevertheless indicates that critical exponents are of mean-field theory type, a result which is borne out by the numerical computations of [13].

In the remainder of the paper we elaborate on all these points in detail. Section 2 introduces the black brane in a cavity as a static system. The solution for its fluctuations to first-derivative order is discussed in section 3. This solution forms the basis for the study in section 4 of stability from a hydrodynamical perspective, and its connection to local thermodynamic stability. Section 5 computes the effective viscosities of the black brane in the cavity of radius R , and then uses them for obtaining the dispersion relation for unstable modes. We conclude with a brief discussion of the critical point and the appearance of mean-field critical exponents.

2 Static black brane in a cylindrical cavity

2.1 Geometry

We write the metric of a black p -brane in $D = 3 + p + n$ spacetime dimensions in the form

$$ds^2 = (-f(r)u_a u_b + P_{ab})d\sigma^a d\sigma^b + \frac{dr^2}{f(r)} + r^2 d\Omega_{(n+1)} \quad (2.1)$$

with

$$f(r) = 1 - \frac{r_0^n}{r^n}, \quad (2.2)$$

and where

$$P_{ab} = \eta_{ab} + u_a u_b \quad (2.3)$$

is the projector onto spatial directions orthogonal to the timelike vector u^a with normalization $\eta_{ab}u^a u^b = -1$.

We put the black brane inside a cylindrical cavity bounded by a ‘wall’ that extends along the brane worldvolume directions σ^a and which, in the transverse directions, is a sphere S^{n+1} at finite radius $r = R$. We denote quantities measured on the cavity wall with a caret. The metric induced on the wall is

$$\hat{h}_{\mu\nu} dx^\mu dx^\nu = \hat{h}_{ab} d\sigma^a d\sigma^b + R^2 d\Omega_{(n+1)} \quad (2.4)$$

with

$$\begin{aligned} \hat{h}_{ab} &= -f(R)u_a u_b + P_{ab} \\ &= -\hat{u}_a \hat{u}_b + \hat{P}_{ab}. \end{aligned} \quad (2.5)$$

Indices of hatted tensors will be raised and lowered with this metric. The velocity

$$\hat{u}_a = \sqrt{f(R)} u_a \quad (2.6)$$

is unit-normalized with respect to this metric by absorbing the redshift factor on the wall. The orthogonal projector, instead, is not modified,

$$\hat{P}_{ab} = P_{ab}, \quad (2.7)$$

since in the geometry (2.1) the spatial worldvolume directions do not suffer any gravitational deformation.

The geometry of the wall of the cavity is characterized by giving, in addition to the induced metric, the extrinsic curvature tensor

$$\Theta_{\mu\nu} = -\frac{1}{2}\sqrt{f(R)}\partial_R\hat{h}_{\mu\nu}. \quad (2.8)$$

Out of this we obtain the Brown-York quasilocal stress-energy tensor on the wall. Since we are only interested in the dynamics of the worldvolume, we only consider the components of the tensor along the directions σ^a , and we integrate them over the transverse S^{n+1} of radius R . The result is that

$$\begin{aligned} \hat{T}_{ab} &= \frac{\Omega_{n+1}}{8\pi G} R^{n+1} (\Theta_{ab} - \hat{h}_{ab}\Theta) \\ &= \frac{\Omega_{n+1}}{8\pi G} \left[-(n+1)R^n\sqrt{f(R)}\hat{u}_a\hat{u}_b + \partial_R(R^{n+1}\sqrt{f(R)})\hat{P}_{ab} \right]. \end{aligned} \quad (2.9)$$

2.2 Physical magnitudes

Eq. (2.9) is a perfect-fluid stress-energy tensor

$$\hat{T}_{ab} = \hat{\varepsilon}\hat{u}_a\hat{u}_b + \hat{P}\hat{P}_{ab} \quad (2.10)$$

with energy density and pressure

$$\hat{\varepsilon} = -\frac{\Omega_{n+1}}{8\pi G}(n+1)R^n\sqrt{f(R)}, \quad (2.11)$$

$$\hat{P} = -\hat{\varepsilon} + \frac{\Omega_{n+1}}{8\pi G}R^{n+1}\partial_R\sqrt{f(R)} = -\hat{\varepsilon} + \frac{\Omega_{n+1}}{16\pi G}\frac{nr_0^n}{\sqrt{f(R)}}. \quad (2.12)$$

In addition, we can assign an entropy density and temperature to the system

$$s = \frac{\Omega_{n+1}}{4\pi G}r_0^{n+1}, \quad (2.13)$$

$$\hat{\mathcal{T}} = \frac{n}{4\pi r_0\sqrt{f(R)}}. \quad (2.14)$$

The temperature is modified relative to its asymptotic value by the redshift factor at the wall, but the entropy density does not depend on R : it is obtained as $s = S/\hat{V}$, where the total entropy S is computed from the horizon area, and the spatial volume \hat{V} does not undergo any variation as R changes.

The system satisfies the thermodynamic Euler relation

$$\hat{\varepsilon} + \hat{P} = \hat{\mathcal{T}}_s, \quad (2.15)$$

and the first law

$$d\hat{\varepsilon} = \hat{\mathcal{T}} ds, \quad (2.16)$$

for variations that keep fixed the cavity radius R .

For the record, we note that when R is allowed to vary, the first law becomes

$$d\hat{\varepsilon} = \hat{\mathcal{T}} ds - \sigma_w da_w \quad (2.17)$$

where the wall area-density a_w and tension σ_w are

$$a_w = \Omega_{n+1} R^{n+1}, \quad \sigma_w = \frac{n}{16\pi G} \frac{1 + f(R)}{R\sqrt{f(R)}}. \quad (2.18)$$

When R can vary the wall is regarded as a dynamical object, and one gets the coupled dynamics of the black brane/wall system. However, although this might be of interest, for the remainder of the paper we will regard the wall only as a non-dynamical boundary condition.

2.3 No subtraction required

When $R \rightarrow \infty$ both $\hat{\varepsilon}$ and \hat{P} diverge, owing to the non-compactness of the space. A simple remedy to this is to subtract the stress-energy tensor associated to a surface in Minkowski space with the same induced metric $\hat{h}_{\mu\nu}$. However, we do not need this for our purposes. The reason is not merely that we keep R finite and thus divergences are absent. More important, the intrinsic worldvolume dynamics that we are interested in is not affected by the subtraction. A surface at constant $r = R$ in Minkowski spacetime has $\Theta_{ab} = 0$ and the stress-energy tensor $T_{ab}^{(M)}$ comes entirely from the curvature Θ of the S^{n+1} of radius R . Then

$$T_{ab}^{(M)} = \frac{\Omega_{n+1}}{8\pi G} (n+1) R^n \hat{h}_{ab}. \quad (2.19)$$

Since we keep R fixed, this stress-energy tensor is of ‘vacuum-type’, i.e., proportional to the worldvolume metric \hat{h}_{ab} and with constant energy density. This is inert: it lacks any hydrodynamic behavior, which is associated with a breakdown of local Lorentz invariance and the presence of inhomogeneities on the worldvolume.

Therefore, the subtraction does not affect the hydrodynamics of the brane, and we shall not implement it.³

3 Fluctuating black brane

We promote the parameters u_a and r_0 in the solution to worldvolume collective degrees of freedom, i.e., slowly-varying functions of σ^a . The remaining parameter, R , is kept fixed.

³It would affect, though, the system in which the wall is dynamical and R varies along the worldvolume.

Following [2], to the now fluctuating metric (2.1) we add correcting functions $f_{\mu\nu}$ such that the total metric

$$ds^2 = \left(\eta_{ab} + \frac{r_0(\sigma)^n}{r^n} u_a(\sigma) u_b(\sigma) \right) d\sigma^a d\sigma^b + \frac{dr^2}{1 - \frac{r_0(\sigma)^n}{r^n}} + r^2 d\Omega_{(n+1)} + f_{\mu\nu} dx^\mu dx^\nu \quad (3.1)$$

is a solution to the field equations. We fix the radial coordinate by choosing it to be orthogonal to the worldvolume and normalized to measure the S^{n+1} -area-radius. Then $f_{\Omega\mu} = 0$. Working to leading order in derivatives, the correcting functions

$$f_{\mu\nu} dx^\mu dx^\nu = f_{ab} d\sigma^a d\sigma^b + 2f_{ar} d\sigma^a dr + f_{rr} dr^2, \quad (3.2)$$

can be decomposed into $\text{SO}(p)$ -algebraically-irreducible terms in the form

$$\begin{aligned} f_{ab} &= \theta u_a u_b \mathfrak{s}_1(r) + \frac{1}{p} \theta P_{ab} \mathfrak{s}_2(r) + a_{(a} u_{b)} \mathfrak{v}_1(r) + \sigma_{ab} \mathfrak{t}(r), \\ f_{ar} &= \theta u_a \mathfrak{s}_3(r) + a_a \mathfrak{v}_2(r), \\ f_{rr} &= \theta \left(1 - \frac{r_0^n}{r^n} \right)^{-1} \mathfrak{s}_4(r), \end{aligned} \quad (3.3)$$

where

$$\theta = \nabla_a u^a, \quad a_a = u^b \nabla_b u_a, \quad \sigma_{ab} = P_a^c P_b^d \nabla_{(c} u_{d)} - \frac{\theta}{p} P_{ab} \quad (3.4)$$

are respectively the expansion, acceleration, and shear of the flow of u^a in the metric η_{ab} . Since these terms are algebraically independent, each of the sets of functions, \mathfrak{s}_i (scalar sector), \mathfrak{v}_i (vector sector), and \mathfrak{t} (tensor sector) decouple from the others in the linearized equations and can be studied separately.

The Einstein equations $R^r_a = 0$ do not involve the $f_{\mu\nu}$ and are independent of r . Thus they are ‘constraint equations’, and can be written in the form

$$\nabla_a \ln r_0^{n+1} = \theta u_a + (n+1) a_a. \quad (3.5)$$

These equations allow to eliminate the derivatives of $r_0(\sigma)$ in terms of velocity gradients. Below we will return to their interpretation in fluid-dynamical terms.

In order to specify boundary conditions at $r = R$, we demand that the induced metric remains fixed and uncorrected to the order we are working,

$$\hat{h}_{ab} = -\hat{u}_a \hat{u}_b + P_{ab} + O(\partial^2). \quad (3.6)$$

This requires that

$$\mathfrak{s}_1(R) = \mathfrak{s}_2(R) = \mathfrak{v}_1(R) = \mathfrak{t}(R) = 0. \quad (3.7)$$

In addition, we ask that the stress-energy tensor is in ‘Landau frame’, defined such that the corrections $\hat{T}_{ab}^{(1)}$ to the leading order value lie entirely along spatial directions, i.e.,

$$\hat{u}^a \hat{T}_{ab}^{(1)} = 0. \quad (3.8)$$

A brief calculation shows that this implies the conditions

$$v_1'(R) = 0, \quad s_2'(R) = \frac{n+1}{R} s_4(R). \quad (3.9)$$

The construction of the solution to the Einstein equations for $f_{\mu\nu}$ that satisfies these boundary conditions and in addition is regular at the horizon, is done in appendix A using the results of [8]. The explicit results are in eqs. (A.4). This provides the complete metric for the fluctuating black brane, to first-derivative order, for any solution of the equations (3.5).

The solution, however, is written in terms of the velocity field u_a and the connection ∇_a for the metric η_{ab} , which is not the physical metric on the wall at $r = R$.⁴ Nevertheless, we can readily find the relation of the latter to quantities on the wall. We do this in appendix B, where we find that

$$\begin{aligned} \hat{u}^a &= \frac{u^a}{\sqrt{f(R)}}, & \hat{\theta} &= \frac{\theta}{\sqrt{f(R)}}, & \hat{\sigma}_{ab} &= \frac{\sigma_{ab}}{\sqrt{f(R)}}, \\ \hat{a}_a &= a_a + \frac{1}{\sqrt{f(R)}} P_a^b \partial_b \sqrt{f(R)}. \end{aligned} \quad (3.10)$$

The change in the velocity, expansion and shear in (3.10) is simply a local redshift. The acceleration is not redshifted, but it is affected by the spatial variation of the redshift along the worldvolume. The point is clearer if we introduce the Newtonian potential ϕ ,

$$f(R) = e^{2\phi}, \quad (3.11)$$

which depends on σ^a through r_0 . Its spatial gradient is

$$\nabla_a \phi \equiv P_a^b \partial_b \phi, \quad (3.12)$$

and we see that the modification of the acceleration is due to a ‘force’ term,

$$\hat{a}_a = a_a + \nabla_a \phi. \quad (3.13)$$

Now using these relations we write the metric in terms of wall quantities as

$$\begin{aligned} ds^2 &= \left(-\frac{f(r)}{f(R)} \hat{u}_a \hat{u}_b + P_{ab} + \frac{\hat{\theta}}{\sqrt{f(R)}} \hat{u}_a \hat{u}_b s_1(r) + \frac{\sqrt{f(R)}}{p} \hat{\theta} P_{ab} s_2(r) \right. \\ &\quad \left. + \frac{1}{\sqrt{f(R)}} (\hat{a}_a - \nabla_a \phi)_{(a} \hat{u}_{b)} v_1(r) + \sqrt{f(R)} \hat{\sigma}_{ab} t(r) \right) d\sigma^a d\sigma^b \\ &\quad + 2(\hat{\theta} \hat{u}_a s_3(r) + (\hat{a}_a - \nabla_a \phi) v_2(r)) d\sigma^a dr \\ &\quad + \frac{dr^2}{f(r)} (1 + \sqrt{f(R)} \hat{\theta} s_4(r)) + r^2 d\Omega_{(n+1)}. \end{aligned} \quad (3.14)$$

As we will see in the next section, the most consequential effect is the modification of the acceleration.

⁴It is neither the metric on the surface at $r \rightarrow \infty$, since with our boundary conditions the functions $s_{1,2}$ and t do not vanish there.

4 Hydrodynamics and stability

For later reference we review briefly some generic features of the dynamics of perfect fluids.

4.1 Perfect fluid dynamics

The hydrodynamic equations $\nabla_a T^{ab} = 0$ for a generic relativistic perfect fluid with stress-energy tensor

$$T_{ab} = \varepsilon u_a u_b + P P_{ab} \quad (4.1)$$

are

$$u^a u^b \nabla_b \varepsilon + P^{ab} \nabla_b P + (\varepsilon + P)(\theta u^a + a^a) = 0. \quad (4.2)$$

The fluid is assumed to satisfy the local thermodynamical relations $\varepsilon + P = T s$ and $d\varepsilon = T ds$. Defining also

$$v_s^2 = \frac{dP}{d\varepsilon}, \quad (4.3)$$

we can write the fluid equations (4.2) in a conveniently simple form

$$\nabla_a \ln s = \theta u_a - \frac{1}{v_s^2} a_a. \quad (4.4)$$

Consider now a fluid state initially in static homogeneous equilibrium in its rest frame, and introduce a small perturbation,

$$s \rightarrow s + \delta s e^{i\omega t + i\mathbf{k}\cdot\mathbf{x}}, \quad u^a = (1, \mathbf{0}) \rightarrow (1, \delta \mathbf{u} e^{i\omega t + i\mathbf{k}\cdot\mathbf{x}}). \quad (4.5)$$

Then the solution to the linearized eqs. (4.4) gives fluctuations with dispersion relation

$$\omega(k) = \sqrt{v_s^2} k + O(k^2), \quad (4.6)$$

where $k = |\mathbf{k}|$. Hence v_s is the velocity of propagation of small density fluctuations, i.e., the speed of sound.

4.2 Black brane hydrodynamics

In the black brane fluid, the entropy density s is directly related to the horizon thickness r_0 by (2.13). Therefore, density fluctuations in the fluid are variations of the horizon radius.

We can immediately see the hydrodynamic Gregory-Laflamme instability in the simplest case in which the cavity wall is removed, $R \rightarrow \infty$ [4, 8]. In this case the induced metric is η_{ab} , the effective fluid velocity is u_a and, comparing to (4.4), we see that the constraint eqs. (3.5) are the equations of the effective relativistic fluid at asymptotic infinity. The effective speed of sound is

$$v_s^2 = -\frac{1}{n+1}, \quad (4.7)$$

which is imaginary and therefore fluctuations of r_0 grow exponentially in time instead of oscillating as sound waves. This is the Gregory-Laflamme instability in the regime of long wavelengths and small (imaginary) frequencies.

Finite cavity: effect of redshift gradients. When we insert the cavity wall at finite R , the gradient term in (3.13) modifies the acceleration with which the effective fluid responds to a change in r_0 . A local fluctuation $\delta r_0 > 0$ results in a smaller ϕ , which tends to push the effective fluid *away* from the region of increased r_0 . Conversely, a region of locally smaller r_0 gives a gradient term that accelerates the fluid towards that region. Therefore, as a consequence of fixing the metric on the cavity wall, the creation of inhomogeneities along the worldvolume is hindered. The result is to make the fluid more stable. Moreover, the effect is more pronounced as the cavity radius R gets closer to the brane, since the redshift becomes stronger.⁵

We can be more quantitative if we use (3.5) to write

$$P_a{}^b \nabla_b \ln r_0 = a_a \quad (4.8)$$

and then

$$\nabla_a \phi = -\frac{n}{2f(R)} \frac{r_0^{n-1}}{R^n} P_a{}^b \nabla_b r_0 = -\frac{n}{2} \left(\frac{1}{f(R)} - 1 \right) a_a. \quad (4.9)$$

Since $f(R) < 1$, we see that $\nabla_a \phi$ is directed opposite to a_a and therefore opposes the unstable growth of inhomogeneities. If, by decreasing R , the gradient grows to a value such that

$$\nabla_a \phi = -a_a, \quad (4.10)$$

then in this state the acceleration of the fluid on the wall vanishes, $\hat{a}_a = 0$: the black brane does not react to a density fluctuation, and the instability disappears. This happens when

$$\frac{n}{2} \left(\frac{1}{f(R)} - 1 \right) = 1, \quad (4.11)$$

that is, when

$$R = R_c = r_0 \left(\frac{n+2}{2} \right)^{1/n}. \quad (4.12)$$

If we reduce R below R_c , the acceleration \hat{a}_a will be directed against the inhomogeneities, and the black brane will be stable.

Effective fluid equations and speed of sound. We can frame this discussion in more fluid-dynamical terms. From (4.9), the relation between the accelerations (3.13) in the black brane fluid is

$$\hat{a}_a = a_a \frac{\hat{v}_s^2}{v_s^2}, \quad (4.13)$$

where

$$\begin{aligned} \hat{v}_s^2 &= -\frac{1}{n+1} \left(1 - \frac{n}{2} \left(\frac{1}{f(R)} - 1 \right) \right) \\ &= -\frac{1}{n+1} \frac{1 - (R_c/R)^n}{f(R)}. \end{aligned} \quad (4.14)$$

⁵Note that the effect is the opposite of what would occur to a material fluid localized on a brane at finite R : this would be gravitationally pulled *towards* larger local mass densities, i.e., larger r_0 . Instead, our effective fluid is not any matter in the spacetime, but rather it is a ‘holographic’ description of the black brane.

Now the constraint equations (3.5) written in terms of the effective fluid velocity on the wall become

$$\hat{\nabla}_a \ln r_0^{n+1} = \hat{\theta} \hat{u}_a - \frac{1}{\hat{v}_s^2} \hat{a}_a. \quad (4.15)$$

Comparing to the general form of the perfect fluid equations (4.4), we see that (4.15) are the equations $\hat{\nabla}_a \hat{T}^{ab} = 0$ for the stress-energy tensor (2.9) and $\hat{v}_s^2 = (d\hat{P}/d\hat{\varepsilon})_R$ is indeed the speed of sound. The quasilocal stress-energy tensor is known to be conserved on general grounds [17], so the result is not surprising. What we have done here is to see explicitly how these conservation equations emerge, on walls at finite R , from the Einstein constraint equations.

The explicit form of eqs. (4.15) is in any case very illustrative. They show clearly that, to the order we work, all the flow with R of the black brane dynamics is due to the modified acceleration term. Since the entropy density is independent of R , the change of the effective fluid with R can be fully accounted for by the change of \hat{v}_s^2 .

The sound velocity \hat{v}_s is imaginary for large R , but it vanishes when the cavity reaches the critical radius R_c in (4.12), and then becomes real for cavity radii $R \in (r_0, R_c)$. This change in stability works in the direction expected from our argument above.

Intuitively, the speed of sound is a measure of the rigidity of the system to worldvolume fluctuations. For very large cavities, the geometry is excessively soft, indeed ‘anti-rigid’, to the point of being unstable to deformations. The cavity wall, by fixing the geometry at a finite distance from the black brane, increases its stiffness and can even render it stable when the cavity is small enough. In fact, \hat{v}_s^2 grows without bound as the wall approaches the horizon, thus making the effective fluid incompressible in that limit.⁶

The growing stiffness of the system caused by worldvolume gradients of the redshift is also apparent in the expressions for the extrinsic curvature, (2.8), and the pressure, (2.12). Thus, the effective hydrodynamic theory explains in a simple manner why and how the black brane turns from unstably soft to stably stiff.

Unstable perturbation. It is now easy to give the complete form of the unstable black brane solution in the cavity. We illustrate it, for simplicity, in the case of a black string with worldsheet coordinates $\sigma^a = (t, x)$. Take a velocity profile of the form

$$\hat{u}_t = -1, \quad \hat{u}_x = \exp(\sqrt{-\hat{v}_s^2} kt) \cos(kx) \delta u, \quad (4.16)$$

and work to linear order in the small amplitude δu . The metric is given by (3.14), with the functions $s_i(r)$, $v_i(r)$ as in eqs. (A.4), and with

$$\hat{P}_{xx} = 1, \quad \hat{\sigma}_{xx} = 0, \quad (4.17)$$

$$\hat{\theta} = -k \exp(\sqrt{-\hat{v}_s^2} kt) \sin(kx) \delta u, \quad (4.18)$$

$$\hat{a}_x = \sqrt{-\hat{v}_s^2} k \exp(\sqrt{-\hat{v}_s^2} kt) \cos(kx) \delta u, \quad (4.19)$$

⁶The fact that $\hat{v}_s \rightarrow \infty$ as $R \rightarrow r_0$ does not necessarily entail any violation of causality. Hydrodynamic fluctuations are low-frequency modes, and causality is controlled by modes in the high-frequency end of the spectrum, see e.g., the discussion in [18].

and

$$\hat{a}_x - \nabla_x \phi = \frac{v_s^2}{\hat{v}_s^2} \hat{a}_x = \frac{f(R)}{1 - (R_c/R)^n} \hat{a}_x. \quad (4.20)$$

4.3 Correlated dynamical and thermodynamic stability

We can easily see that the change in dynamical stability at $R = R_c$ corresponds precisely to the change in the local thermodynamic stability of the black brane, i.e., in the thermodynamic stability of the black hole that one obtains at any given point on the worldvolume. Since (2.15) and (2.16) imply $d\hat{P} = sd\hat{T}$ we have

$$\left(\frac{d\hat{P}}{d\hat{\varepsilon}} \right)_R = \frac{s}{\hat{C}_V} \quad (4.21)$$

where \hat{C}_V is the specific heat at fixed volume. Since the sign of \hat{C}_V determines the local thermodynamic stability, the connection between the latter and the dynamical stability of the brane, in the hydrodynamic regime, is obvious. This is nothing but the fact that stability of hydrodynamic modes associated to conserved quantities is governed by the local thermodynamic properties of the fluid.

In the calculation of the speed of sound and in eq. (4.21) we only need the static brane solution. What our study of the fluctuating brane shows is that there is indeed an explicit solution for a black brane in a fixed cavity which is regular on the horizon and which is dynamically stable or unstable in accord with its thermodynamical stability.

5 Viscous hydrodynamics

Having the fluctuating black brane geometry to first order in velocity gradients, we extract its quasilocal stress-energy tensor at finite R including dissipative terms.

5.1 Bulk and shear viscosities do not run

The general form of the stress-energy tensor on the cavity wall at finite R , in the spacetime given by (3.1), (3.2), (3.3), and with boundary conditions (3.7) and (3.9), is

$$\begin{aligned} \hat{T}_{ab} = & \frac{\Omega_{n+1}}{8\pi G} \left[- (n+1) R^n \sqrt{f(R)} \hat{u}_a \hat{u}_b + \partial_R (R^{n+1} \sqrt{f(R)}) \hat{P}_{ab} \right] \\ & - \hat{\zeta} \hat{P}_{ab} - 2\hat{\eta} \hat{\sigma}_{ab} + O(\partial^2), \end{aligned} \quad (5.1)$$

with bulk and shear viscosities

$$\hat{\zeta} = \frac{\Omega_{n+1}}{8\pi G} \left[\frac{R^{n+1}}{2} s'_1(R) + \left(\frac{n+1}{2p} (R^n - r_0^n) + \frac{n}{4} r_0^n \right) s_4(R) \right], \quad (5.2)$$

and

$$\hat{\eta} = \frac{\Omega_{n+1}}{8\pi G} \frac{R^{n+1}}{4} f(R) t'(R). \quad (5.3)$$

Substituting the explicit values for the solution that is regular on the horizon, we get

$$\hat{\zeta} = \frac{s}{2\pi} \left(\frac{1}{p} + \frac{1}{n+1} \right) \quad (5.4)$$

and

$$\hat{\eta} = \frac{s}{4\pi}, \quad (5.5)$$

with s the entropy density (2.13).

While the result for the shear viscosity is not surprising, the fact that the bulk viscosity remains the same at all R is probably less obviously expected. In particular, observe that it is of the form

$$\hat{\zeta} = \frac{s}{2\pi} \left(\frac{1}{p} - v_s^2 \right). \quad (5.6)$$

Thus it depends on the asymptotic value of the speed of sound, instead of its value \hat{v}_s^2 at the cavity wall, which one might naively have guessed. Had it been the latter case, $\hat{\zeta}$ would have run with R . Since s is independent of R , we can equivalently say that neither $\hat{\eta}/s$ nor $\hat{\zeta}/s$ run with R .

This absence of running of $\hat{\zeta}$ is most probably related to the one in [16], where it was found that for AdS black branes in a finite cavity the bulk viscosity remains zero at all R , despite the fact that the wall breaks conformal invariance. There exists an explicit mapping between AdS gravity and the sector of vacuum gravity involved in our system [19] which is independent of the cavity wall. Conceivably, it relates our result to that of [16] and possibly makes clearer why $\hat{\zeta}$ depends on v_s^2 instead of \hat{v}_s^2 .

For AdS black branes, ref. [16] found an intriguing relation, $\hat{T}^a{}_a = -d\hat{\epsilon}/d\ln R$, for the running of the energy density with R . For our neutral black branes, the same equation formally applies if we set $n = -p - 1$, which is not any physical black brane, and in fact corresponds to setting $D = 2$. Since, again formally, when $n = -p - 1$ one gets $\hat{\zeta} = 0$, this running is valid including first-derivative corrections. The reason why this result holds in this context is possibly related to properties of analytic continuation in n , but at present its ultimate meaning is unclear to us.

5.2 Spectrum of unstable modes

With $\hat{\zeta}$ and $\hat{\eta}$ we can compute the corrections to the fluid equations due to the viscous damping of density fluctuations. This gives us a better approximation for the spectrum of unstable modes at finite R .

Solving the fluid equations to quadratic order in momenta k , the unstable modes of the black brane in a cavity with $R > R_c$ have imaginary frequency

$$\begin{aligned} \Omega(k) &= \sqrt{-\hat{v}_s^2} k - \frac{1}{2\hat{T}s} \left[\left(1 - \frac{1}{p} \right) 2\hat{\eta} + \hat{\zeta} \right] k^2 + O(k^3) \\ &= \frac{k}{\sqrt{n+1}} \sqrt{\frac{1 - (R_c/R)^n}{f(R)}} - k^2 r_0 \frac{n+2}{n(n+1)} \sqrt{f(R)} + O(k^3), \end{aligned} \quad (5.7)$$

where R_c is given in (4.12). We illustrate this result in figure 1. As R approaches R_c , the instability gets weaker, having both a smaller rate of growth Ω and a shorter range of unstable wavenumbers k .

While there is no previous calculation of black brane instabilities in a finite cavity that we can match these curves to, we can compare against the computation in ref. [13] of the

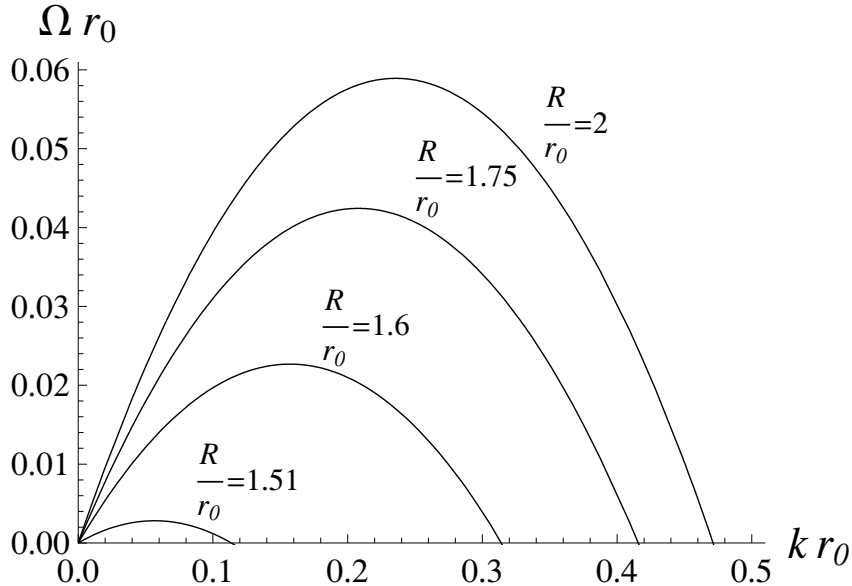


Figure 1. Spectrum of GL unstable modes for a black brane in a cavity of radius R , according to eq. (5.7). The curves correspond to $n = 1$, for which the critical radius is $R_c = 1.5 r_0$.

wavenumber k_{GL} of the zero-mode, for which $\Omega(k_{\text{GL}}) = 0$. Our analytic expression (5.7), truncated to quadratic order, gives

$$k_{\text{GL}} = \frac{1}{r_0} \frac{n\sqrt{n+1}}{n+2} \frac{\sqrt{1 - (R_c/R)^n}}{f(R)}. \quad (5.8)$$

We display this result in figure 2, where we compare it with the corresponding one of figure 3 in [13]. The qualitative agreement between the two graphs is apparent, but one can easily discern quantitative discrepancies. These are expected, since (5.8) has been obtained under the hydrodynamic assumption of small wavenumbers $k/\hat{T} \ll 1$, which is not satisfied in general. As in [8], we may expect the agreement to improve for larger n .

5.3 Critical behavior

Eq. (4.15) implies that when $\hat{v}_s^2 = 0$, the acceleration of the fluid under a density perturbation vanishes, i.e., the fluid does not respond to variations of r_0 . Using (4.21) we see that at that point the effective specific heat \hat{C}_V becomes infinite. This result makes manifest that the divergence of the specific heat is linked to the ghost instability — the hydrodynamic mode is at the threshold of becoming ghost-like. The connection between the divergence of \hat{C}_V and the tachyonic instability is, instead, only indirect: as discussed in the introduction, a hydrodynamic ghost instability of a black hole system is typically accompanied by a tachyonic instability. The hydrodynamic statement that $d\hat{P}/d\hat{\epsilon} \rightarrow 0$ means that the fluid does not react with any pressure gradient to local variations of the energy density. Thermodynamically, the fact that $\hat{C}_V \rightarrow \infty$ means that under these density variations the system does not create any temperature gradients that would restore it back to thermal equilibrium. Both effects, hydrodynamic and thermodynamic, are of course related via

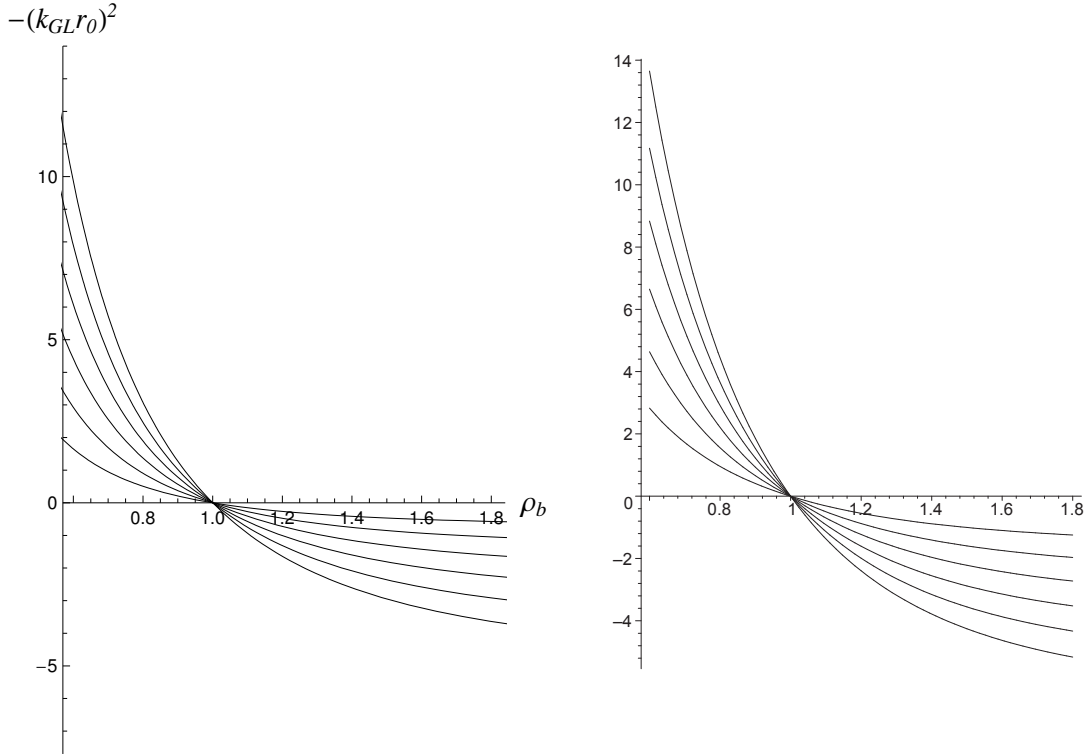


Figure 2. Evolution of the GL zero mode k_{GL} as a function of the cavity radius R . Left: obtained from the approximate analytical expression (5.8). Right: numerical results from [13]. Following [13], in the vertical axis we display the ‘tachyon mass squared’, $-(k_{\text{GL}}r_0)^2$, and in the horizontal axis $\rho_b = (R - r_0)/(R_c - r_0)$, so that the critical radius is always at $\rho_b = 1$. The curves are for $n = 2, \dots, 7$, and lie closer to the horizontal axis the smaller n is. The finite, non-zero slope of the curves at $\rho_b = 1$ indicates mean-field critical behavior (5.9).

$d\hat{P} = sd\hat{\mathcal{T}}$. At the point where $\hat{C}_V \rightarrow \infty$, thermal fluctuations in the fluid have infinite wavelength. Then, this is a thermodynamic critical point.

In the critical state, the tachyonic zero mode becomes massless, i.e., has infinite wavelength, and therefore it must be included alongside with the hydrodynamic modes in the effective low-frequency, long wavelength theory. Note, however, that this tachyon is never a proper hydrodynamic mode: the fluid equations never admit (to any arbitrary derivative order) a non-trivial static solution. The inclusion of the massless tachyon in the effective theory at the critical point cannot be done working solely within hydrodynamics.

Thus, the result (5.8) from a truncated hydrodynamical calculation need not be accurate near the critical point. Note, however, that it predicts a critical behavior

$$k_{\text{GL}} \sim (R - R_c)^{1/2}, \quad (5.9)$$

which has a mean-field theory exponent. This appears to be correct: the numerical curves of [13] for $-k_{\text{GL}}^2$, reproduced in the right-side graph in figure 2, cut the horizontal axis with non-zero, finite slope consistently with the critical behavior (5.9). Perhaps we should not be too surprised: a mean-field theory description of the critical state might be natural in a classical field theory like general relativity and in a state with smooth horizons.

First order transition: inaccessibility of the critical point. The locally-unstable phases of the system of a black brane in a cavity are extremely fine-tuned states, which we have considered not so much for their possible relevance to actual physical phenomena but as being illustrative of the dynamics of black branes. But, actually, even the critical point and the associated second-order phase transition cannot be expected to be reached through any physical process, as they are dominated by a stronger first-order transition.

We have presented the problem starting from the black brane inside a very large cavity and then reduced the size of the cavity until the black brane becomes locally stable. However, from the perspective of a physical process it makes more sense to start from the system in the stable regime of $R \ll R_c$ and then follow it as we increase R . We are imagining that we keep the horizon size r_0 fixed, but one could easily consider other processes, e.g., fix R and change the temperature of the box.

When R reaches the value

$$R_1 = \left(\frac{n+2}{2(n+1)} \right)^{1/n} R_c < R_c, \quad (5.10)$$

the pressure \hat{P} of the black brane becomes equal to that of Minkowski space in the same cavity, (2.19), and for $R > R_1$ the latter has larger pressure. Thus, when the brane is ‘supercooled’ at $R_1 < R < R_c$, even if it is locally stable it will undergo a first-order phase transition and spontaneously nucleate bubbles of the ‘true vacuum’, i.e., hot flat space.⁷ This will form holes in the worldvolume of the brane that then begin to expand. It may be interesting to study further this phenomenon, which shares features with the one studied in [20]. At any rate, it will prevent the observation of the critical state at $R = R_c$, and indeed of all the unstable black brane phases.

Acknowledgments

We are greatly indebted to Joan Camps, Veronika Hubeny, and Mukund Rangamani, for sharing their insights on this problem in many discussions, and for their comments on the manuscript. We are also grateful to Simon Ross for providing and giving permission to use the right-side graph in figure 2. Work supported by MEC FPA2010-20807-C02-02, AGAUR 2009-SGR-168 and CPAN CSD2007-00042 Consolider-Ingenio 2010.

A Solution with finite-cavity boundary conditions

Ref. [8] solved the Einstein equations for the perturbations to first order in derivatives and obtained the general solution that is regular on the future event horizon. The solution, expressed in Eddington-Finkelstein coordinates, contains a number of integration constants that are to be determined by conditions at the spatial boundary. For ease of comparison, we use the same notation for these constants (c_{vr} , c_{ii} , etc.) as in [8]. All the calculations at finite R , including the stress-energy tensor, could be carried out in Eddington-Finkelstein

⁷For the black hole inside a spherical cavity ($p = 0$) this is the analogue of the Hawking-Page transition.

coordinates [6], but here we choose to work in Schwarzschild coordinates to maintain continuity with [5, 8]. In these coordinates the solution is

$$s_1(r) = \frac{n+2}{2(n+1)} \left(f(r) - \frac{n}{n+2} \right) s_2(r) + c_{vv} - 2c_{vr} - f(r)c_{vv}, \quad (\text{A.1a})$$

$$s_2(r) = \frac{2r_0}{n} \ln f(r) + c_{ii}, \quad (\text{A.1b})$$

$$s_3(r) = \frac{1}{2f(r)} \left[\left(\frac{n}{n+1} - f(r) \right) s_2(r) + \frac{2r_0}{n+1} (f(r) - 1) \left(n \frac{r_*}{r_0} + 1 \right) \right] + c_{vv} - c_{vr} - \frac{c_{vv} - 2c_{vr}}{f(r)}, \quad (\text{A.1c})$$

$$s_4(r) = (f(r)^{-1} - 1) \left(\frac{4r_0 - ns_2(r)}{2(n+1)} + c_{vv} - 2c_{vr} \right), \quad (\text{A.1d})$$

$$v_1(r) = c_{vi}^{(2)} + \frac{c_{vi}^{(1)}}{r^n}, \quad (\text{A.1e})$$

$$v_2(r) = \frac{r_* - r + v_1(r)}{f(r)} + f_{rj}(r), \quad (\text{A.1f})$$

$$t(r) = s_2(r) + c_{ij}, \quad (\text{A.1g})$$

where

$$r_* = \int \frac{dr}{1 - \frac{r_0^n}{r^n}}. \quad (\text{A.2})$$

The function $f_{rj}(r)$ is a gauge-dependent function only constrained to be finite on the horizon and thus could be set to zero.

The boundary conditions (3.7), (3.9) are satisfied by choosing

$$c_{vv} = c_{vr} = c_{vi}^{(1)} = c_{vi}^{(2)} = c_{ij} = 0, \quad c_{ii} = -\frac{2r_0}{n} \ln f(R), \quad (\text{A.3})$$

with which

$$s_1(r) = \frac{n+2}{2(n+1)} \left(f(r) - \frac{n}{n+2} \right) s_2(r), \quad (\text{A.4a})$$

$$s_2(r) = \frac{2r_0}{n} \ln \frac{f(r)}{f(R)}, \quad (\text{A.4b})$$

$$s_3(r) = \frac{1}{2f(r)} \left[\left(\frac{n}{n+1} - f(r) \right) s_2(r) + \frac{2r_0}{n+1} (f(r) - 1) \left(n \frac{r_*}{r_0} + 1 \right) \right], \quad (\text{A.4c})$$

$$s_4(r) = (f(r)^{-1} - 1) \left(\frac{4r_0 - ns_2(r)}{2(n+1)} \right), \quad (\text{A.4d})$$

$$v_1(r) = 0, \quad (\text{A.4e})$$

$$v_2(r) = \frac{r_* - r}{f(r)} + f_{rj}(r), \quad (\text{A.4f})$$

$$t(r) = s_2(r). \quad (\text{A.4g})$$

This is the unique solution, up to the gauge choice of $f_{rj}(r)$, that satisfies the regularity condition at the horizon and the boundary conditions on the wall at fixed R .

B Connection on the wall

We present here the relation between the connections ∇_a and $\hat{\nabla}_a$ compatible with, resp., the metrics η_{ab} and \hat{h}_{ab} , and we use this to relate the gradients of the respective velocity vectors, u_a and \hat{u}_a . We decompose these gradients, as usual, into traceless symmetric shear σ_{ab} , expansion θ , acceleration a_a , and antisymmetric vorticity ω_{ab} , so that

$$\nabla_a u_b = \sigma_{ab} + \frac{1}{p}\theta P_{ab} - u_a a_b + \omega_{ab}, \quad (\text{B.1})$$

and similarly for hatted quantities.

We follow the same steps as in [16]. If the difference between the metrics is

$$\gamma_{ab} = \hat{h}_{ab} - \eta_{ab} \quad (\text{B.2})$$

then the difference between the connections, $\tilde{\Gamma}_{ab}^c$, such that

$$\hat{\nabla}_a V_b = \nabla_a V_b - \tilde{\Gamma}_{ab}^c V_c \quad (\text{B.3})$$

is given by

$$\tilde{\Gamma}_{ab}^c = \frac{1}{2}\hat{h}^{cd}(\nabla_a \gamma_{bd} + \nabla_b \gamma_{ad} - \nabla_d \gamma_{ab}). \quad (\text{B.4})$$

In our case,

$$\gamma_{ab} = (1 - f)u_a u_b. \quad (\text{B.5})$$

Here we always take f evaluated on the wall, i.e., $f = f(R)$, which depends on σ through $r_0(\sigma)$. We find

$$\begin{aligned} \tilde{\Gamma}_{ab}^c &= \frac{u^d \partial_d f}{2f} u^c u_a u_b - \frac{1}{f} u^c u_{(a} P_{b)}^d \partial_d f + \frac{1}{2} u_a u_b P^{cd} \partial_d f \\ &\quad + (f^{-1} - 1)u^c \left(\sigma_{ab} + \frac{1}{p}\theta P_{ab} \right) + 2(1 - f)u_{(a} \omega_{b)}^c - (1 - f)a^c u_a u_b. \end{aligned} \quad (\text{B.6})$$

Using this and (2.6) we find that

$$\hat{\nabla}_a \hat{u}_b = \frac{1}{\sqrt{f}} \left(\sigma_{ab} + \frac{1}{p}\theta P_{ab} \right) + \sqrt{f} \omega_{ab} - \hat{u}_a \left(a_b + \frac{1}{2f} P_b^c \partial_c f \right), \quad (\text{B.7})$$

from where we immediately deduce eqs. (3.10) and

$$\hat{\omega}_{ab} = \sqrt{f} \omega_{ab}. \quad (\text{B.8})$$

Note that we have not made use anywhere of the fluid equations of motion for eliminating the derivatives of f in favor of derivatives of the velocity. This is done in section 4.2

An alternative but equivalent way of obtaining the same results is the following. We may regard the two metrics as related, to zeroth derivative order, by the change $\hat{u}_a \hat{\sigma}^a = \sqrt{f(R)} u_a \sigma^a$. Above we have set $\hat{u}_a = \sqrt{f(R)} u_a$ and left the coordinates unchanged. But we could just as well leave $\hat{u}_a = u_a$, perform a coordinate rescaling (of time), and include the derivatives of $f(R)$ that result from this coordinate change into the correction terms $f_{\mu\nu}$.

References

- [1] T. Damour, *Surface effects in black hole physics*, in Proceedings of the *Second Marcel Grossmann Meeting on General Relativity*, R. Ruffini ed., North Holland, Amsterdam Netherlands (1982), pg. 587.
- [2] S. Bhattacharyya, V.E. Hubeny, S. Minwalla and M. Rangamani, *Nonlinear fluid dynamics from gravity*, *JHEP* **02** (2008) 045 [[arXiv:0712.2456](#)] [[INSPIRE](#)].
- [3] R. Emparan, T. Harmark, V. Niarchos and N.A. Obers, *World-volume effective theory for higher-dimensional black holes*, *Phys. Rev. Lett.* **102** (2009) 191301 [[arXiv:0902.0427](#)] [[INSPIRE](#)].
- [4] R. Emparan, T. Harmark, V. Niarchos and N.A. Obers, *Essentials of blackfold dynamics*, *JHEP* **03** (2010) 063 [[arXiv:0910.1601](#)] [[INSPIRE](#)].
- [5] J. Camps and R. Emparan, *Derivation of the blackfold effective theory*, *JHEP* **03** (2012) 038 [*Erratum ibid.* **06** (2012) 155] [[arXiv:1201.3506](#)] [[INSPIRE](#)].
- [6] R. Emparan, V.E. Hubeny and M. Rangamani, to appear.
- [7] R. Gregory and R. Laflamme, *Black strings and p-branes are unstable*, *Phys. Rev. Lett.* **70** (1993) 2837 [[hep-th/9301052](#)] [[INSPIRE](#)].
- [8] J. Camps, R. Emparan and N. Haddad, *Black brane viscosity and the Gregory-Laflamme instability*, *JHEP* **05** (2010) 042 [[arXiv:1003.3636](#)] [[INSPIRE](#)].
- [9] S.S. Gubser and I. Mitra, *The evolution of unstable black holes in anti-de Sitter space*, *JHEP* **08** (2001) 018 [[hep-th/0011127](#)] [[INSPIRE](#)].
- [10] J.W. York Jr., *Black hole thermodynamics and the Euclidean Einstein action*, *Phys. Rev. D* **33** (1986) 2092 [[INSPIRE](#)].
- [11] H.S. Reall, *Classical and thermodynamic stability of black branes*, *Phys. Rev. D* **64** (2001) 044005 [[hep-th/0104071](#)] [[INSPIRE](#)].
- [12] T. Harmark, V. Niarchos and N.A. Obers, *Instabilities of black strings and branes*, *Class. Quant. Grav.* **24** (2007) R1 [[hep-th/0701022](#)] [[INSPIRE](#)].
- [13] J.P. Gregory and S.F. Ross, *Stability and the negative mode for Schwarzschild in a finite cavity*, *Phys. Rev. D* **64** (2001) 124006 [[hep-th/0106220](#)] [[INSPIRE](#)].
- [14] A. Buchel, *A holographic perspective on Gubser-Mitra conjecture*, *Nucl. Phys. B* **731** (2005) 109 [[hep-th/0507275](#)] [[INSPIRE](#)].
- [15] J.J. Friess, S.S. Gubser and I. Mitra, *Counter-examples to the correlated stability conjecture*, *Phys. Rev. D* **72** (2005) 104019 [[hep-th/0508220](#)] [[INSPIRE](#)].
- [16] D. Brattan, J. Camps, R. Loganayagam and M. Rangamani, *CFT dual of the AdS Dirichlet problem: fluid/gravity on cut-off surfaces*, *JHEP* **12** (2011) 090 [[arXiv:1106.2577](#)] [[INSPIRE](#)].
- [17] J.D. Brown and J.W. York Jr., *Quasilocal energy and conserved charges derived from the gravitational action*, *Phys. Rev. D* **47** (1993) 1407 [[gr-qc/9209012](#)] [[INSPIRE](#)].
- [18] D. Marolf and M. Rangamani, *Causality and the AdS Dirichlet problem*, *JHEP* **04** (2012) 035 [[arXiv:1201.1233](#)] [[INSPIRE](#)].
- [19] M. Caldarelli, J. Camps, B. Gouteraux and K. Skenderis, private communication.
- [20] G.T. Horowitz and M.M. Roberts, *Dynamics of first order transitions with gravity duals*, *JHEP* **02** (2007) 076 [[hep-th/0701099](#)] [[INSPIRE](#)].

BLACK STRING FLOW

This chapter contains the publication:

- R. Emparan and M. Martinez,
“Black String Flow,”
JHEP **1309**, 068 (2013), [arXiv:1307.2276](#) [hep-th].

Black string flow

Roberto Emparan^{a,b} and Marina Martínez^b

^a*Institució Catalana de Recerca i Estudis Avançats (ICREA),
Passeig Lluís Companys 23, E-08010 Barcelona, Spain*

^b*Departament de Física Fonamental and Institut de Ciències del Cosmos,
Universitat de Barcelona,
Martí i Franquès 1, E-08028 Barcelona, Spain*

E-mail: emparan@ub.edu, marinamartinez@icc.ub.edu

ABSTRACT: We give an exact description of the steady flow of a black string into a planar horizon. The event horizon is out of equilibrium and provides a simple, exact instance of a ‘flowing black funnel’ in any dimension $D \geq 5$. It is also an approximation to a smooth intersection between a black string and a black hole, in the limit in which the black hole is much larger than the black string thickness. The construction extends easily to more general flows, in particular charged flows.

KEYWORDS: Black Holes, Black Holes in String Theory

ARXIV EPRINT: [1307.2276](https://arxiv.org/abs/1307.2276)

Contents

1	Introduction	1
2	Horizon of black string flow	2
3	Out-of-equilibrium flow	7
4	Charged flows	8
5	Outlook	10
A	Explicit integration of the event horizon	11

1 Introduction

Recent studies of black holes and black branes have sparked an interest in stationary spacetimes admitting event horizons that are not Killing horizons, i.e., the null generators of the horizon are not parallel to the generators of isometric time translations.¹ From a technical viewpoint, the theorems [3–5] that would forbid this possibility are evaded since the horizons are non-compactly generated. From a physical perspective, such horizons connect two asymptotic regions of infinite extent which have different surface gravities, i.e., different temperatures. They can be regarded as describing a steady heat flow between two infinite heat reservoirs that keep a temperature gradient constant in time.

In this article we describe a remarkably simple, exact solution for a ‘flowing horizon’. The explicit nature of the construction allows a detailed study of the properties of the flow. Since the spacetime is Ricci-flat, it shows that, in contrast to previous descriptions of horizon flows (motivated by AdS/CFT) [1, 2, 6–9], a negative cosmological constant is not essential for their existence.

In order to motivate the construction, let us first imagine a thin black string, of thickness r_{bs} , that falls vertically into a very large black hole of radius $r_{bh} \gg r_{bs}$.² The black string has a much larger surface gravity than the black hole. If the string is free-falling into the black hole horizon, then there are no external forces acting on the system and we can expect that the two horizons merge smoothly.³ This is not a stationary configuration: the black hole is accreting mass from the string that flows into it and therefore must grow

¹To the best of our knowledge, horizons with this property were first described, independently, in [1] and [2].

²We may envisage two black strings, falling at antipodal points of the black hole horizon, in order to avoid any total pull on the black hole. Note that the notion of the string falling ‘vertically’ along its length is sensible since the worldsheet of a black string is not Lorentz invariant.

³Instead of meeting at a singular cusp [10], which in the present context would be unphysical.

in size. However, this effect becomes negligible if we take the limit $r_{bh} \rightarrow \infty$ keeping r_{bs} fixed, and focus on the region where the two horizons meet. The black hole horizon then becomes an acceleration, Rindler-type infinite horizon, into which the black string flows by falling freely across it. Going to the rest frame of the falling black string, the acceleration horizon disappears: we are left with the spacetime of a static black string.

In other words, if we take a static black string and view it from a frame that accelerates along the direction of the string, what we observe is a string in free fall into an acceleration horizon. We will construct the event horizon for such accelerated observers (taking also into account their dragging by the string, as we will see), and show that it interpolates smoothly between the Rindler horizon of a ‘cold’, infinitely-large black hole, at large distances from the string, and the Killing horizon of the ‘hot’ black string when far from the acceleration horizon. It is clear that the spacetime has a timelike Killing vector — which defines the rest frame of the string — but the flowing event horizon is not mapped into itself under its action.

The horizon of this ‘black string flow’ is closely similar to the ‘black funnels’ of [7–9, 11–14], where a string-like horizon that in one direction extends towards the AdS boundary, in the other direction smoothly merges with the infinitely extended horizon of an AdS black brane. The two constructions differ in their asymptotics but otherwise describe essentially similar phenomena. Our construction should approximate well the horizon of an AdS funnel much thinner than the AdS radius, in the region where it joins the AdS black brane. Indeed, it should give the universal description of all neutral, non-rotating, thin black funnels over distances sufficiently close to the horizon.

2 Horizon of black string flow

In the rest frame of the free-falling black string, and in $D = n + 4$ spacetime dimensions, the metric is

$$ds^2 = -f(r)dt^2 + dz^2 + \frac{dr^2}{f(r)} + r^2 d\Omega_{n+1}, \quad (2.1)$$

with

$$f(r) = 1 - \left(\frac{r_0}{r}\right)^n. \quad (2.2)$$

In the absence of the string ($f = 1$), the null surfaces $t = z + t_0$, with constant t_0 , are (future) acceleration horizons, i.e., event horizons for trajectories of asymptotically uniform acceleration along z . Often this is made manifest by changing to coordinates adapted to accelerating observers, but this is actually not needed, nor is it very practical in the present case. Instead, it is simpler to trace back an appropriate congruence of null rays from null asymptotic infinity.⁴ In our case, one condition that we clearly want to be satisfied is that the null rays reach the conventional Rindler horizon far from the string, i.e.,

$$\frac{\dot{t}}{\dot{z}} \rightarrow 1 \quad \text{and} \quad \dot{r} \rightarrow 0 \quad \text{for} \quad r \rightarrow \infty, \quad (2.3)$$

⁴An approach similar in essence was previously used in [15].

where the dot denotes derivative with respect to an affine parameter λ . These turn out to be the main conditions that we will need to impose, with all other initial conditions on the geodesics following naturally.

The angles on S^{n+1} remain fixed for each null geodesic so that the event horizon preserves the symmetry $\text{SO}(n+2)$. The equations for $t(\lambda)$, $z(\lambda)$, $r(\lambda)$ are easy to obtain from

$$-ft^2 + \dot{z}^2 + \frac{\dot{r}^2}{f} = 0, \quad (2.4)$$

and

$$\dot{t} = \frac{\epsilon}{f}, \quad \dot{z} = p, \quad (2.5)$$

where ϵ and p are two integration constants coming from the isometries generated by ∂_t and ∂_z . Then (2.3) is satisfied by setting

$$\frac{\epsilon}{p} = 1. \quad (2.6)$$

Null hypersurface \mathcal{H}_f . The null hypersurface ruled by outgoing geodesics can now be characterized by the one-form equation

$$dt = dz + \frac{\sqrt{1-f}}{f} dr, \quad (2.7)$$

i.e.,

$$t = z + t_0 + \int \frac{\sqrt{1-f}}{f} dr, \quad (2.8)$$

each value of t_0 giving a different null hypersurface that ends at a different value of the null coordinate in future null infinity. Obviously, any of them can serve as our event horizon, differing simply by a translation in $t - z$. We shall denote the null hypersurface with $t_0 = 0$ as \mathcal{H}_f — the flowing, or funnel, horizon. Clearly it is not a stationary horizon: the action of ∂_t changes t_0 and therefore it does not map a hypersurface onto itself but rather onto another one. The explicit form of the integral in r in (2.8) is not particularly illuminating and we give it in the appendix. The surface \mathcal{H}_f is plotted in figure 1.

We can introduce coordinates x_{\pm} adapted to these null surfaces, defined by

$$dx_{\pm} = dt \pm \left(dz + \frac{\sqrt{1-f}}{f} dr \right). \quad (2.9)$$

These are null one-forms normal to the hypersurfaces defined by $dx_{\pm} = 0$. The vectors $\partial/\partial x_{\pm} = (\partial_t \pm \partial_z)/2$ are instead spacelike vectors tangent to these hypersurfaces, i.e., $dx_- \cdot (\partial/\partial x_+) = 0$ and $dx_+ \cdot (\partial/\partial x_-) = 0$. Moreover, the hypersurfaces $dx_+ = 0$ (resp. $dx_- = 0$) are symmetric under the action of $\partial/\partial x_-$ (resp. $\partial/\partial x_+$).

The geometry (2.1) written in coordinates (x_-, z, r, Ω) takes the form

$$ds^2 = -f dx_-^2 - 2 dx_- \left(f dz + \sqrt{1-f} dr \right) + \left(dr - \sqrt{1-f} dz \right)^2 + r^2 d\Omega_{n+1}. \quad (2.10)$$

\mathcal{H}_f is the null surface $x_- = 0$. Taking also its time reversal, namely the null surface $x_+ = 0$, we can regard the region $x_- < 0$, $x_+ > 0$ that they bound as the Rindler wedge modified by the presence of the black string, see figure 2.

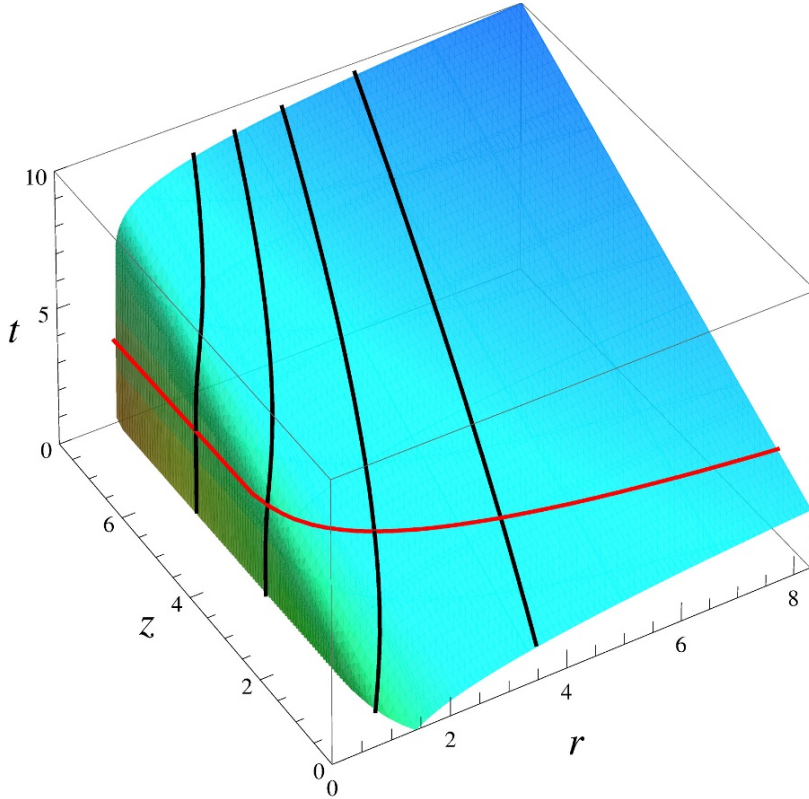


Figure 1. Event horizon \mathcal{H}_f of the black string flow as the hypersurface (2.8) in (t, r, z) space (for $n = 2$ and $r_0 = 1$). It extends along $-\infty < z, t < \infty$ and $1 < r < \infty$. The black string lies at $r = 1$, and is reached at $t \rightarrow -\infty$. At any finite r , the surface tends to $t = z$ at large z . The black curves are null geodesics representative of the congruence that rules the hypersurface, for (left to right) $\zeta = 5, 3, 0, -6$. The red curve is a constant- t section.

Null geodesic congruence. The null geodesics that rule \mathcal{H}_f are easily obtained. Using the freedom to rescale λ we set $\epsilon = p = 1$. Then, since

$$\dot{z} = 1, \quad \dot{r} = \sqrt{1 - f}, \quad (2.11)$$

we have

$$\begin{aligned} z(\lambda) &= \lambda + \zeta, \\ r^{\frac{n+2}{2}}(\lambda) &= r_0^{\frac{n+2}{2}} \left(r_0 + \frac{n+2}{2} \lambda \right), \end{aligned} \quad (2.12)$$

and $t(\lambda)$ is obtained from (A.1). Here ζ is an integration constant that labels each null ray of the congruence. It corresponds to the value of z for the ray when $\lambda = 0$, i.e., when $r = r_0$ and $t \rightarrow -\infty$. We can then take (λ, ζ) as the coordinates on the null hypersurface (together with the angles of S^{n+1}). If we eliminate them we obtain the hypersurface $t(r, z)$ in (2.8).

For each value of ζ we have a light ray outgoing in the r direction, which initially hovers just above the black string horizon, until it escapes out to infinity moving in the r and z directions, see figure 1.

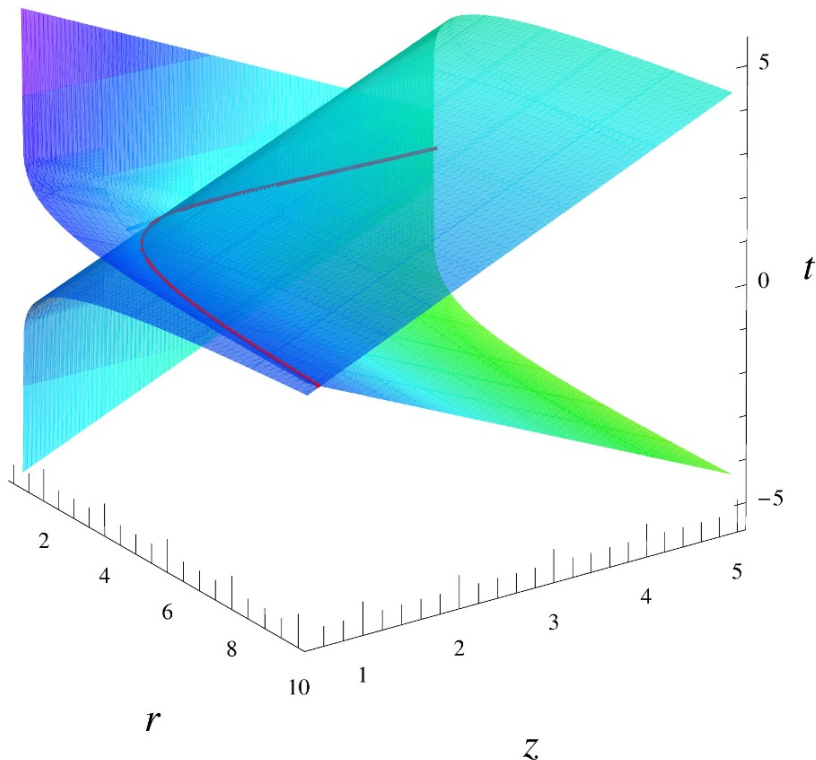


Figure 2. The wedge formed by the null hypersurfaces $x_+ = 0$, $x_- = 0$ (for $n = 3$). The curve at their intersection at $t = 0$ is marked in red.

Note that $r = r_0$ is reached at a finite value of the affine parameter, namely $\lambda = 0$. This is in fact the same as for null outgoing trajectories outside the horizon in the Schwarzschild geometry: they have $\epsilon > 0$ and reach $r = r_0$ in the *past* horizon at a finite affine parameter. In our construction the same happens for the null geodesics in \mathcal{H}_f . Taking $\lambda < 0$ they are extended into the interior of the white hole until they reach at $r = 0$ the past curvature singularity of the solution.

Event horizon and black string drag. \mathcal{H}_f given by (2.8) is a codimension-1 null hypersurface that extends to asymptotic infinity. It is the future null boundary of a region of spacetime, and it is natural to ask what are the timelike trajectories that have \mathcal{H}_f as their event horizon.

According to eq. (2.12), all light rays on \mathcal{H}_f move towards $r \rightarrow \infty$ as the affine parameter grows. Then, any timelike trajectory that remains within bounded values of r will cross \mathcal{H}_f at a finite time. That is, \mathcal{H}_f is *not* an event horizon for observers that remain within a finite range of the black string: they all fall across \mathcal{H}_f eventually.

We interpret this phenomenon physically as a dragging effect. A boosted black string (one that moves at constant velocity) has around itself an ergosurface at a constant radial distance. Observers inside this surface cannot remain static but are dragged along with the string. In our configuration the black string is accelerating, i.e., its velocity grows,

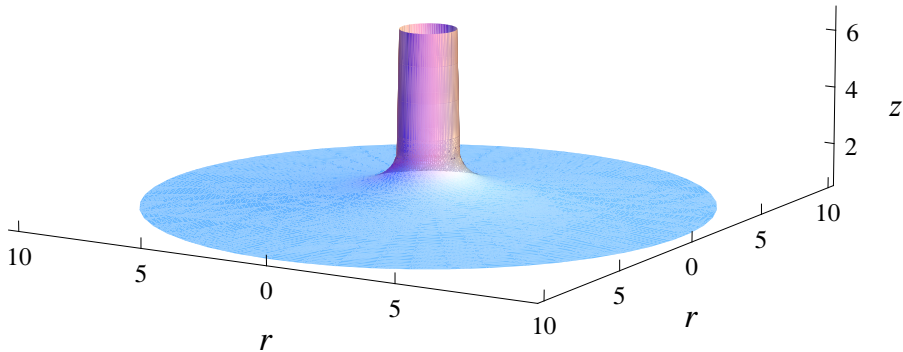


Figure 3. Constant-time cross section of the event horizon (2.14) (for $n = 3$ and $r_0 = 1$), illustrating the funnel-shape that interpolates between the black string and the infinite planar acceleration horizon. The circles at constant z are actually S^{n+1} . The funnel extends infinitely in z and r .

and so the ergoregion grows too. We expect then that any trajectory that remains within a finite distance from the string will be dragged along with it and eventually cross the acceleration horizon, thus moving to the future of \mathcal{H}_f . An observer who wants to avoid crossing \mathcal{H}_f must not only accelerate in the z direction, but it must also move out towards $r \rightarrow \infty$. These are the observers that have \mathcal{H}_f as their event horizon.⁵ It is straightforward to extend this analysis to the class of observers whose motion is confined inside the wedge in figure 2 by considering trajectories which are time-reversal invariant around $t = 0$.

Funnel geometry. Consider a cross-section of this horizon at constant t (or equivalently, at constant x_+). From (2.9) and (2.10), the metric induced on it is

$$ds_{(\text{hor})}^2 = \frac{dr^2}{f^2} + r^2 d\Omega_{n+1}. \quad (2.13)$$

This geometry describes an infinite funnel: at $r \rightarrow \infty$ it becomes flat space, while near $r = r_0$, where f vanishes linearly in r , we find an infinite throat with the geometry $\mathbb{R} \times S^{n+1}$, with sphere radius r_0 .⁶ We can describe this surface as the curve

$$z + \int \frac{\sqrt{1-f}}{f} dr = 0, \quad (2.14)$$

which we represent in figure 3. This illustrates clearly the idea that the black string and the Rindler horizon merge smoothly into a funnel-shaped horizon.

⁵The dragging effect becomes weaker in higher dimensions. For very large n it is only appreciable within a distance r_0/n of the black string [16]. As $n \rightarrow \infty$, the horizon becomes exactly a planar Rindler horizon outside this region.

⁶Coincidentally, this is the same geometry as the spatial section of the extremal Reissner-Nordstrom solution.

3 Out-of-equilibrium flow

The vector

$$\begin{aligned}\frac{d}{d\lambda} &= \dot{t} \frac{\partial}{\partial t} + \dot{z} \frac{\partial}{\partial z} + \dot{r} \frac{\partial}{\partial r} \\ &= \frac{1}{f} \frac{\partial}{\partial t} + \frac{\partial}{\partial z} + \sqrt{1-f} \frac{\partial}{\partial r}.\end{aligned}\tag{3.1}$$

is an affine generator of the null geodesic congruence. It is convenient to consider the following non-affine generator of the future event horizon,

$$\begin{aligned}\ell &= \frac{1}{2} f(r(\lambda)) \frac{d}{d\lambda} \\ &= \frac{1}{2} \left(\frac{\partial}{\partial t} + f \frac{\partial}{\partial z} + f \sqrt{1-f} \frac{\partial}{\partial r} \right).\end{aligned}\tag{3.2}$$

This is normalized in such a way that near and far from the black string we recover the generators of the black string horizon and of the acceleration horizon. Often the Rindler horizon generator is taken to be the boost vector $z\partial_t + t\partial_z$, which at $t = z$ becomes $t(\partial_t + \partial_z)$. However, this is not adequate for us: the boost vector gives a finite, dimensionless surface gravity $\kappa = 1$, to the Rindler horizon. This is the acceleration of observers at unit proper distance from the horizon, and not the surface gravity in the infinite radius limit of a black hole, which is zero.

The surface gravity $\kappa_{(\ell)}$ of ℓ is defined as the non-affinity factor of the geodesics,

$$\nabla_{\ell} \ell = \kappa_{(\ell)} \ell.\tag{3.3}$$

Since λ is an affine parameter we easily find that

$$\begin{aligned}\kappa_{(\ell)} &= \ell^{\mu} \partial_{\mu} \ln f \\ &= \frac{n}{2r} \left(\frac{r_0}{r} \right)^{3n/2}.\end{aligned}\tag{3.4}$$

This surface gravity decreases monotonically from its asymptotic value at the black string horizon at $r = r_0$, where $\kappa_{(\ell)} \rightarrow n/(2r_0)$, down to $\kappa_{(\ell)} \rightarrow 0$ at large r where the horizon approximates the planar Rindler horizon.

Since the horizon is out of equilibrium, we can expect that its expansion be positive. In order to compute it, consider the geometry of sections at constant λ ,

$$ds_{(\text{hor})}^2 = (1 - f(r(\lambda))) d\zeta^2 + r^2(\lambda) d\Omega_{n+1}.\tag{3.5}$$

Here we use the coordinate ζ on the surface, instead of r as in (2.13), since $\partial/\partial r$ does not commute with $d/d\lambda$ and therefore is not a good coordinate for the congruence. The area element on this surface is

$$a = \sqrt{1-f} r^{n+1} \omega_{n+1}\tag{3.6}$$

(where ω_{n+1} is the area element of S^{n+1}) and therefore the expansion of $d/d\lambda$ is

$$\theta_{(\lambda)} = \frac{d \ln a}{d\lambda} = \frac{n+2}{2} \frac{\sqrt{1-f}}{r}.\tag{3.7}$$

This is indeed positive, so the area of the horizon grows to the future. It is also monotonically decreasing, vanishing at $r \rightarrow \infty$.

If we consider the expansion associated to ℓ we get

$$\theta_{(\ell)} = \ell^\mu \partial_\mu \ln a = \frac{1}{2} f \theta_{(\lambda)} = \frac{n+2}{4} f \frac{\sqrt{1-f}}{r}. \quad (3.8)$$

This is again positive, but now it vanishes both at $r = r_0$ and at $r \rightarrow \infty$. Thus the flow of the vector ℓ reflects the property that this event horizon interpolates between two asymptotic horizons, each of which is asymptotically in equilibrium at a different temperature.

Finally, note that not only is the horizon out of global equilibrium, i.e., has non-constant κ , but it is also away from *local* equilibrium. By this we mean that the gradient $r_0 \partial_z \ln \kappa_{(\ell)}$ becomes large in the region $r \gg r_0$. Then the surface gravity at a section of the horizon at constant z , with radius $r(\lambda)$, is not well approximated by the surface gravity of a black string with that horizon radius — as should be clear from figure 3. As a consequence, the flowing horizon cannot be described in the effective hydrodynamic theory for black strings [17, 18].

4 Charged flows

Our previous analysis can be easily extended to more general static black string metrics of the form

$$ds^2 = -T(r)dt^2 + Z(r)dz^2 + \frac{dr^2}{R(r)} + r^2 H(r) d\Omega_{n+1}, \quad (4.1)$$

where all the metric functions are assumed positive outside the black string horizon and tend to 1 at $r \rightarrow \infty$. By a suitable choice of the radial coordinate we could set $H = 1$, or instead $R = T$. Each choice has its virtues, so we shall keep this radial gauge freedom.

Solutions with $T = Z$ are qualitatively different from those with $T < Z$ (and when $T > Z$ there are no null geodesics with $\epsilon/p = 1$). When $T = Z$ the string worldsheet is Lorentz-invariant and the notion of the string falling along its length is not well defined. The black string horizon does not merge with the Rindler horizon, but instead the two just intersect. This can be easily seen by performing the conventional change to Rindler coordinates, $t = \rho \sinh \eta$, $z = \rho \cosh \eta$: the black string horizon at $r = r_0$, where $T(r_0) = 0$, and the Rindler horizon at $\rho = 0$, form two intersecting null surfaces, both with zero expansion. Later we discuss a relevant instance of this.

Henceforth we restrict ourselves to $T < Z$. The flowing event horizon is characterized by

$$dt = dz + dr \sqrt{\frac{Z(r) - T(r)}{T(r)Z(r)R(r)}}, \quad (4.2)$$

and in terms of the coordinates (λ, ζ) on the congruence, where ζ labels different null rays and λ the affine parameter along them, we have

$$dz = Z^{-1} d\lambda + d\zeta, \quad dr = \sqrt{\frac{R(Z - T)}{TZ}} d\lambda. \quad (4.3)$$

The metric on a constant- t section (or constant λ) of this horizon is

$$\begin{aligned} ds_{(\text{hor})}^2 &= \frac{Z}{TR} dr^2 + r^2 H(r) d\Omega_{n+1} \\ &= (Z - T) d\zeta^2 + r^2 H(r) d\Omega_{n+1}. \end{aligned} \quad (4.4)$$

For the non-affine null geodesic generator

$$\ell = \frac{1}{2} \left(\partial_t + \frac{T}{Z} \partial_z + \sqrt{(Z - T) \frac{RT}{Z}} \partial_r \right) \quad (4.5)$$

the surface gravity is

$$\kappa_{(\ell)} = \sqrt{(Z - T) \frac{R}{TZ}} \frac{\partial_r T}{2}. \quad (4.6)$$

This vanishes as $r \rightarrow \infty$, while close to $T = 0$ it reproduces the surface gravity of the event horizon of the black string,

$$\kappa_{(\ell)} \rightarrow \sqrt{\frac{R}{T}} \frac{\partial_r T}{2}. \quad (4.7)$$

The expansion is

$$\theta_{(\ell)} = \frac{1}{2} \left(\frac{\partial_r Z - \partial_r T}{Z - T} + \frac{n+1}{r} + \frac{n+1}{2} \frac{\partial_r H}{H} \right) \sqrt{(Z - T) \frac{RT}{Z}}. \quad (4.8)$$

The first term inside the brackets is due to the expansion along the string direction, while the latter two correspond to the spherical expansion in the radial direction. The last factor comes from $\ell^\mu \partial_\mu r$.

A natural class of solutions to study are charged strings, in particular electrically charged ones. The qualitative properties differ depending on whether the charge is string-charge, i.e., the strings are electric sources of a 2-form potential $B_{\mu\nu}$, or 0-brane charge, which sources a Maxwell 1-form potential A_μ .

String charge. Configurations with string charge are of interest for several reasons. The neutral black string flow of previous sections is unstable, since the spacetime (2.1) is itself unstable [19]. However, string-charged black strings that are sufficiently close to extremality, but not necessarily extremal, are stable.

An interesting instance are black strings with fundamental string charge, i.e., black F-strings. Above extremality the horizon can be regarded as the gravitational description of a thermal spectrum of excitations on a stack of fundamental strings. The ‘F-string flow’ horizon then describes, in gravitational terms, the flow of these excitations down a very large black hole that the string intersects. Even if the F-string charge allows to tune down the temperature of the black string, only at extremality can it be in thermal equilibrium with the infinitely large black hole. This extremal limit has Lorentz-invariance along z , with $T = Z$, so in this case there is actually no flow. Above extremality the string excitations are at a higher temperature than the black hole, and the system appears to differ from those in which the string excitations are in thermal equilibrium with a finite-temperature horizon (as studied in a worldsheet approach, e.g., [20–23], or in the blackfold approach [24, 25]). In our construction, when the black string is not extremal it is not mining energy from the black hole, but rather dumping it.

0-brane charge. 0-brane charge on a black string breaks Lorentz symmetry on the worldsheet at any temperature, including at extremality. The horizons of these strings can then merge smoothly with the Rindler horizon and there is always a non-zero flow. For extremal string flows the surface gravity associated to ℓ is zero only at the black string, where (4.7) vanishes, and at the Rindler horizon at $r \rightarrow \infty$. Inbetween them, the surface gravity is generically non-zero, as is also the expansion $\theta_{(\ell)}$. So these are always out-of-equilibrium configurations.

One may wonder what drives the flow when both its endpoints are at zero temperature. It is easy to see that it is driven by a gradient of the electric potential, i.e., an electric field along the horizon. The charge on the string is in free fall across the acceleration horizon. On the event horizon, this phenomenon is a charge current from the black string to the planar horizon, driven by an electric field. This field on the event horizon is the projection (pullback) of the spacetime electric field that the static black string creates. Clearly this field points in the direction of increasing r , and thus, on the event horizon, it points from the black string towards the planar horizon. It may be interesting to understand better these charge flows. In particular the appearance of a temperature on the horizon of the extremal string flow, in which the asymptotic endpoints are at zero temperature, is suggestive of resistive (Joule) dissipation of the electric current on the horizon.

Finally, 0-brane charge does not prevent the instability of the black string, as this charge can be redistributed along the horizon. However, the addition of string charge can make these solutions stable, even supersymmetric. In the latter case, the flowing horizon is not parallel to the timelike vector associated to the Killing spinors, and therefore need not be an extremal horizon.

5 Outlook

The black string flow studied above approximates a system where a very thin black string smoothly pierces a black hole. A similar-looking configuration has been found in the late-time evolution of the black string instability [26] — including a flow from the string that makes the black hole grow. It would be interesting to study in more detail the geometry in the latter case, near the region where the ‘black hole’ and ‘black string’ meet, to see if it conforms to the flowing horizon we have constructed.

Black funnels in AdS can be interpreted holographically in dual terms as a flow of Hawking radiation in the boundary theory, emitted from a black hole through a thermal radiation fluid that extends to infinity [1, 7]. For our flowing geometries, a similar interpretation is also possible — although only to some extent, since the quantum degrees of freedom of the dual radiation are not known. In order to understand how this works, consider first the Rindler horizon, without the string. If we impose Dirichlet boundary conditions on a timelike surface \mathcal{S} at a fixed, finite proper distance from the horizon, then the gravitational dynamics of the system can be described in terms of a dual thermal ‘Rindler fluid’ on \mathcal{S} [27]. If we introduce the black string, then there will be a black hole horizon on \mathcal{S} where it intersects the black string. The dual description, in terms of the quasilocal stress-energy tensor on \mathcal{S} , will then exhibit a flow of the Rindler fluid qualitatively similar

to that in AdS. Note also that in this Rindler-fluid set up, the C-metric yields an exact droplet solution in a four-dimensional bulk. The construction is like that of a black hole on a thin, planar domain wall in [28].

The method we have employed of finding non-equilibrium acceleration horizons in stationary black hole spacetimes can be extended to other situations of interest, for instance: (i) rotating black strings, to yield rotating string flows; (ii) black strings in AdS, to obtain black funnels in (hyperbolic) AdS black branes; (iii) Schwarzschild black holes, to find the event horizon in the final plunge of extreme-mass-ratio black hole collisions. We plan to report on these systems elsewhere.

Acknowledgments

We gratefully acknowledge conversations with Pau Figueras, Veronika Hubeny, and Don Marolf. Work supported by MEC FPA2010-20807-C02-02, AGAUR 2009-SGR-168 and CPAN CSD2007-00042 Consolider-Ingenio 2010.

A Explicit integration of the event horizon

Setting for simplicity $r_0 = 1$, the event horizon (2.8) is the surface

$$\begin{aligned} t - t_0 &= z + \int \frac{dr}{r^{n/2} - r^{-n/2}} \\ &= z - \frac{2r^{(2-n)/2}}{n-2} {}_2F_1\left(\frac{n-2}{2n}, 1, \frac{3n-2}{2n}; r^{-n}\right). \end{aligned} \quad (\text{A.1})$$

When $n = 2$ we find

$$t - t_0 = z + \frac{1}{2} \ln(r^2 - 1). \quad (\text{A.2})$$

The expression simplifies for other values of n , e.g.,

$$t - t_0 = z + 2\sqrt{r} + \ln \frac{\sqrt{r} - 1}{\sqrt{r} + 1} \quad (n = 1), \quad (\text{A.3})$$

$$t - t_0 = z + \frac{1}{2} \arctan r + \frac{1}{4} \ln \frac{r-1}{r+1} \quad (n = 4). \quad (\text{A.4})$$

At large values of r the surface tends to

$$t - t_0 \rightarrow z - \frac{2r^{(2-n)/2}}{n-2}, \quad (\text{A.5})$$

so for larger n the horizon asymptotes more rapidly to $t = z$. In fact for $n = 1, 2$, the limit of $r \rightarrow \infty$ at fixed z or fixed t does not tend to $t = z$ (although it is always the case that $dt \rightarrow dz$ at $r \rightarrow \infty$). The interpretation is that, as might be expected, low-codimension black string flows spread much more in the transverse directions than higher-codimension flows. Nevertheless, the spatial geometry of the horizon (2.13) is asymptotically flat in all dimensions.

References

- [1] V.E. Hubeny, D. Marolf and M. Rangamani, *Hawking radiation in large- N strongly-coupled field theories*, *Class. Quant. Grav.* **27** (2010) 095015 [[arXiv:0908.2270](#)] [[INSPIRE](#)].
- [2] S. Khlebnikov, M. Kruczenski and G. Michalogiorgakis, *Shock waves in strongly coupled plasmas*, *Phys. Rev. D* **82** (2010) 125003 [[arXiv:1004.3803](#)] [[INSPIRE](#)].
- [3] S. Hawking, *Black holes in general relativity*, *Commun. Math. Phys.* **25** (1972) 152 [[INSPIRE](#)].
- [4] S. Hollands, A. Ishibashi and R.M. Wald, *A higher dimensional stationary rotating black hole must be axisymmetric*, *Commun. Math. Phys.* **271** (2007) 699 [[gr-qc/0605106](#)] [[INSPIRE](#)].
- [5] V. Moncrief and J. Isenberg, *Symmetries of higher dimensional black holes*, *Class. Quant. Grav.* **25** (2008) 195015 [[arXiv:0805.1451](#)] [[INSPIRE](#)].
- [6] S. Khlebnikov, M. Kruczenski and G. Michalogiorgakis, *Shock waves in strongly coupled plasmas II*, *JHEP* **07** (2011) 097 [[arXiv:1105.1355](#)] [[INSPIRE](#)].
- [7] S. Fischetti and D. Marolf, *Flowing funnels: heat sources for field theories and the AdS_3 dual of CFT_2 Hawking radiation*, *Class. Quant. Grav.* **29** (2012) 105004 [[arXiv:1202.5069](#)] [[INSPIRE](#)].
- [8] P. Figueras and T. Wiseman, *Stationary holographic plasma quenches and numerical methods for non-Killing horizons*, *Phys. Rev. Lett.* **110** (2013) 171602 [[arXiv:1212.4498](#)] [[INSPIRE](#)].
- [9] S. Fischetti, D. Marolf and J.E. Santos, *AdS flowing black funnels: stationary AdS black holes with non-Killing horizons and heat transport in the dual CFT* , *Class. Quant. Grav.* **30** (2013) 075001 [[arXiv:1212.4820](#)] [[INSPIRE](#)].
- [10] R. Emparan and N. Haddad, *Self-similar critical geometries at horizon intersections and mergers*, *JHEP* **10** (2011) 064 [[arXiv:1109.1983](#)] [[INSPIRE](#)].
- [11] V.E. Hubeny, D. Marolf and M. Rangamani, *Black funnels and droplets from the AdS C -metrics*, *Class. Quant. Grav.* **27** (2010) 025001 [[arXiv:0909.0005](#)] [[INSPIRE](#)].
- [12] V.E. Hubeny, D. Marolf and M. Rangamani, *Hawking radiation from AdS black holes*, *Class. Quant. Grav.* **27** (2010) 095018 [[arXiv:0911.4144](#)] [[INSPIRE](#)].
- [13] M.M. Caldarelli, O.J. Dias, R. Monteiro and J.E. Santos, *Black funnels and droplets in thermal equilibrium*, *JHEP* **05** (2011) 116 [[arXiv:1102.4337](#)] [[INSPIRE](#)].
- [14] J.E. Santos and B. Way, *Black funnels*, *JHEP* **12** (2012) 060 [[arXiv:1208.6291](#)] [[INSPIRE](#)].
- [15] P. Figueras, V.E. Hubeny, M. Rangamani and S.F. Ross, *Dynamical black holes and expanding plasmas*, *JHEP* **04** (2009) 137 [[arXiv:0902.4696](#)] [[INSPIRE](#)].
- [16] R. Emparan, R. Suzuki and K. Tanabe, *The large D limit of general relativity*, *JHEP* **06** (2013) 009 [[arXiv:1302.6382](#)] [[INSPIRE](#)].
- [17] R. Emparan, T. Harmark, V. Niarchos and N.A. Obers, *Essentials of blackfold dynamics*, *JHEP* **03** (2010) 063 [[arXiv:0910.1601](#)] [[INSPIRE](#)].
- [18] J. Camps, R. Emparan and N. Haddad, *Black brane viscosity and the Gregory-Laflamme instability*, *JHEP* **05** (2010) 042 [[arXiv:1003.3636](#)] [[INSPIRE](#)].
- [19] R. Gregory and R. Laflamme, *Black strings and p -branes are unstable*, *Phys. Rev. Lett.* **70** (1993) 2837 [[hep-th/9301052](#)] [[INSPIRE](#)].
- [20] A.E. Lawrence and E.J. Martinec, *Black hole evaporation along macroscopic strings*, *Phys. Rev. D* **50** (1994) 2680 [[hep-th/9312127](#)] [[INSPIRE](#)].

- [21] V.P. Frolov and D. Fursaev, *Mining energy from a black hole by strings*, *Phys. Rev. D* **63** (2001) 124010 [[hep-th/0012260](#)] [[INSPIRE](#)].
- [22] A. Kaya, *Open cosmic strings in black hole space-times*, *Phys. Rev. D* **67** (2003) 024013 [[hep-th/0210275](#)] [[INSPIRE](#)].
- [23] J. de Boer, V.E. Hubeny, M. Rangamani and M. Shigemori, *Brownian motion in AdS/CFT*, *JHEP* **07** (2009) 094 [[arXiv:0812.5112](#)] [[INSPIRE](#)].
- [24] G. Grignani, T. Harmark, A. Marini, N.A. Obers and M. Orselli, *Heating up the BIon*, *JHEP* **06** (2011) 058 [[arXiv:1012.1494](#)] [[INSPIRE](#)].
- [25] G. Grignani, T. Harmark, A. Marini, N.A. Obers and M. Orselli, *Thermodynamics of the hot BIon*, *Nucl. Phys. B* **851** (2011) 462 [[arXiv:1101.1297](#)] [[INSPIRE](#)].
- [26] L. Lehner and F. Pretorius, *Black strings, low viscosity fluids and violation of cosmic censorship*, *Phys. Rev. Lett.* **105** (2010) 101102 [[arXiv:1006.5960](#)] [[INSPIRE](#)].
- [27] I. Bredberg, C. Keeler, V. Lysov and A. Strominger, *Wilsonian approach to fluid/gravity duality*, *JHEP* **03** (2011) 141 [[arXiv:1006.1902](#)] [[INSPIRE](#)].
- [28] R. Emparan, R. Gregory and C. Santos, *Black holes on thick branes*, *Phys. Rev. D* **63** (2001) 104022 [[hep-th/0012100](#)] [[INSPIRE](#)].

BUMPY BLACK HOLES

This chapter contains the publication:

- R. Emparan, P. Figueras and M. Martinez,
“Bumpy black holes,”
JHEP **1412**, 072 (2014), [arXiv:1410.4764](https://arxiv.org/abs/1410.4764) [hep-th].

Bumpy black holes

Roberto Emparan,^{a,b} Pau Figueras^c and Marina Martínez^b

^a*Institució Catalana de Recerca i Estudis Avançats (ICREA)
Passeig Lluís Companys 23, E-08010 Barcelona, Spain*

^b*Departament de Física Fonamental, Institut de Ciències del Cosmos, Universitat de Barcelona,
Martí i Franquès 1, E-08028 Barcelona, Spain*

^c*DAMTP, Centre for Mathematical Sciences,
Wilberforce Road, Cambridge CB3 0WA, U.K.*

E-mail: emparan@ub.edu, pf289@cam.ac.uk, marinamartinez@ub.edu

ABSTRACT: We study six-dimensional rotating black holes with *bumpy* horizons: these are topologically spherical, but the sizes of symmetric cycles on the horizon vary non-monotonically with the polar angle. We construct them numerically for the first three bumpy families, and follow them in solution space until they approach critical solutions with localized singularities on the horizon. We find strong evidence of the conical structures that have been conjectured to mediate the transitions to black rings, to black Saturns, and to a novel class of bumpy black rings. For a different, recently identified class of bumpy black holes, we find evidence that this family ends in solutions with a localized singularity that exhibits apparently universal properties, and which does not seem to allow for transitions to any known class of black holes.

KEYWORDS: Black Holes, Black Holes in String Theory

ARXIV EPRINT: [1410.4764](https://arxiv.org/abs/1410.4764)

Contents

1	Introduction and main results	1
2	Construction of the Solutions	4
2.1	Boundary conditions	6
2.2	Physical magnitudes	7
3	Geometry of bumpy black holes	8
3.1	(+)-branch bumpy black holes	9
3.1.1	Critical cone geometries	9
3.1.2	(+) ₃ : transition to bumpy black rings	12
3.2	(-)-branch bumpy black holes	13
4	Phase diagrams, thermodynamic stability, and negative modes	15
A	Numerics	19

1 Introduction and main results

In spite of the lack of effective solution-generating methods, the exploration of black hole solutions of the vacuum Einstein equations in $D \geq 6$ has made significant strides through the complementary use of approximate analytical methods and numerical calculations. One line of study follows the observation that rapidly spinning Myers-Perry (MP) black holes in $D \geq 6$ [1] approach black membranes, so they can be expected to admit, as black branes do, stationary deformations that ripple the horizon [2]. Such *bumpy black hole* solutions would naturally connect to black rings, black Saturns, and multi-ring solutions through topology-changing transitions in solution space [3, 4]. Evidence for this picture has been provided in [5–9]. In this article we confirm, refine, and extend aspects of it through a detailed numerical investigation of bumpy black holes in $D = 6$.

Bumpy black holes, like MP black holes (in the singly-spinning case that will be the focus of this article), have horizon topology S^{D-2} with spatial symmetry group $U(1) \times SO(D-3)$. What distinguishes them from the “smooth” MP black holes is that the size of the S^{D-4} symmetry orbits on their horizon varies in a non-monotonic fashion from the axis of rotation to the equator.

The different families of bumpy black holes are conveniently identified by the way they branch off the MP family. Refs. [5, 6] identified linearized zero-mode perturbations of singly-rotating MP black holes, to which we can assign an ‘overtone’ number $i = 1, 2, \dots$ ¹

¹We ignore the “ $i = 0$ ” zero mode [5] since it stays on the MP family and does not give rise to new branches of solutions.

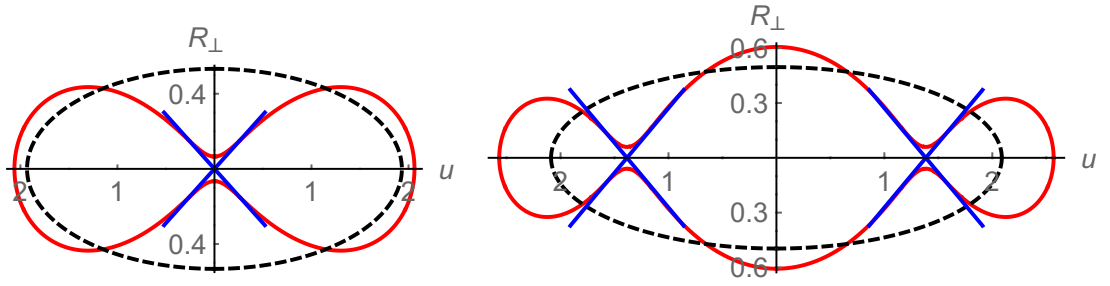
that, for fixed mass, grows with the spin. Let us conventionally fix the sign of the zero-mode so that the i -th mode wavefunction at the axis of rotation has sign $(-1)^i$. By adding or subtracting the zero-mode perturbation to the MP black hole, we obtain two different branches, $(+)_i$ and $(-)_i$, of solutions emerging from the branching point. The evolution of the solutions along the $(+)$ -branches was anticipated in [3]: the horizon develops bumps that grow until a S^{D-4} cycle pinches down to zero size, naturally suggesting a topology-changing transition to other black holes: black rings for $i = 1$, black Saturns for $i = 2$, and multi-ring configurations for $i > 2$. The $(-)$ -branches of solutions were only identified recently in [8], and as we will see, they seem to terminate without any plausible connection to other black hole solutions.

Ref. [8] has studied the $(+)_1$ and $(-)_1$ branches in six and seven dimensions. Here we extend the analysis in the six-dimensional case to higher branches, $i = 1, 2, 3$, while pushing both the $(+)$ and $(-)$ branches closer to their ends in phase space at singular solutions. We also perform a detailed investigation of the geometrical properties of these bumpy black holes. Our main conclusions, partly illustrated in figures 1 and 2, are:

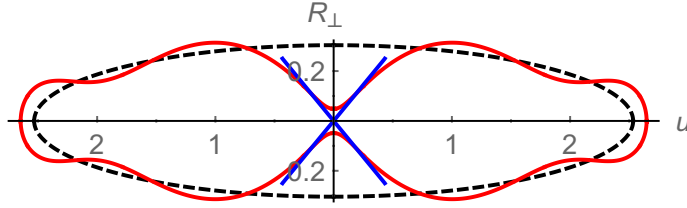
1. The $(+)$ branches terminate at critical solutions with conifold-type singularities localized on the horizon of precisely the kind predicted in [10] (following [11]).
2. The $(+)_3$ solutions pinch on the horizon at two places, on the rotation axis and off the axis, with the on-axis pinch growing deeper than the off-axis one. This strongly suggests that these solutions connect to a family of ‘bumpy black rings’ not yet constructed. We expect that these rings eventually pinch off to connect to black di-rings.
3. The $(-)$ branches terminate at solutions with a curvature singularity localized at the equator of the horizon. The structure of the singularity appears to be locally the same for all i : the S^2 on the horizon shrinks to zero at the equator in a manner that resembles the cone that appears in the $(+)_2$ branch, while the length of the equatorial circle diverges. However, we are unable to provide an explicit local model for this singularity. We do not find any plausible extension of this branch to other singly-spinning black hole solutions.

The conclusion in point 2 eliminates the possibility, considered as an alternative in [3], that the connection to black di-rings occurs through a phase of ‘bumpy black Saturns’. We give a simple argument to suggest that, as we move away of the MP solutions, the horizons in higher- i branches pinch-off in succession from the rotation axis to the equator. Let us also remark that the divergent length of the equatorial circle mentioned in point 3 is not visible in figure 2, but will be made apparent in figure 8 below.

These results are explained in detail in section 3, after having outlined in section 2 the construction of the solutions. In addition, in section 4 we compute the thermodynamic properties of these solutions and draw phase diagrams. We also analyze the spectrum of the Lichnerowicz operator, and relate the number of negative eigenvalues to the thermodynamic stability of the solutions. The details of our numerics are relegated to appendix A.



(a) $(+)_1$ -branch black hole at $j = 1.13$, close to the transition to a black ring. (b) $(+)_2$ -branch black hole at $j = 1.20$, close to the transition to a black Saturn.



(c) $(+)_3$ -branch black hole at $j = 1.55$, close to the transition to a bumpy black ring.

Figure 1. Embedding diagrams of bumpy black hole horizons of the $(+)_1,2,3$ branches (red curves), for the largest deformations we have obtained. The value of R_\perp gives the size of the spheres S^2 transverse to the rotation plane. The vertical axis $u = 0$ is the rotation axis, but u does not measure the radius of the rotation circles. We superimpose the embeddings of MP black holes with the same mass and spin (dashed black), and of the cones proposed for a local model of the critical singularity, eq. (3.9) (blue). The angular momentum j is normalized as in (2.19). In this and all subsequent plots, units are $GM = 1$.

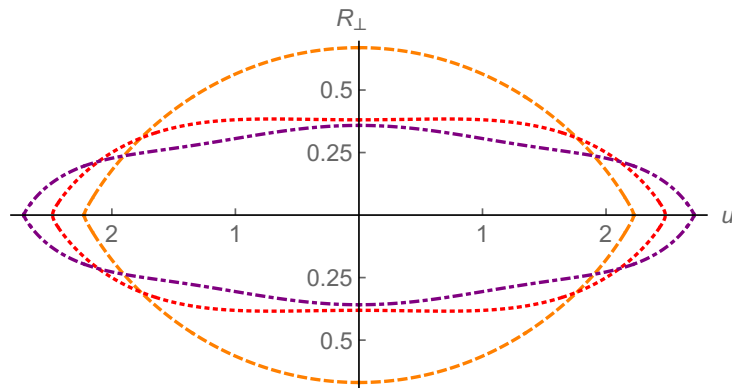


Figure 2. Embedding diagrams for $(-)_1,2,3$ branch black holes (1: orange long-dash; 2: red short-dash; 3: purple dot-dash) at the largest deformations we have obtained. All branches exhibit the same singular conical shape near the equator (reflecting the rate at which the S^2 shrink there), with the same opening angle as in the critical $(+)_2$ solutions.

We remark that all these bumpy black holes are expected to be dynamically unstable; their importance lies in what they reveal about the possible geometries of black hole horizons in higher dimensions and the rich web of interconnections among them.

2 Construction of the Solutions

In order to construct deformed rotating black holes in six dimensions we solve the Einstein-DeTurck equations $R_{ab}^H = 0$ where

$$R_{ab}^H = R_{ab} - \nabla_{(a}\xi_{b)} \quad \text{and} \quad \xi^a = g^{bc}(\Gamma_{bc}^a - \bar{\Gamma}_{bc}^a). \quad (2.1)$$

Γ is the usual Levi-Civita connection compatible with the spacetime metric g and $\bar{\Gamma}$ is the Levi-Civita connection compatible with some reference metric \bar{g} that satisfies the same boundary conditions as the spacetime metric g but needs not be a solution to Einstein's equations. This is a standard method used in numerical General Relativity to find static and stationary solutions [12–14]: the equations are manifestly elliptic and one can then use conventional numerical techniques for solving such partial differential equations. For asymptotically flat (AdS or Kaluza-Klein) static metrics [13] proved that the solutions to the Einstein-DeTurck equations must in fact be Einstein. This result is yet to be extended to the stationary case, and hence, since we are interested in Einstein metrics, we must check that the DeTurck vector ξ vanishes. For the solutions presented in this article we have checked that this is indeed the case, within our numerical accuracy.

The solutions we study are stationary and with only one of the two possible rotations turned on. Thus the rotation group $\text{SO}(5)$ is broken down to $\text{U}(1) \times \text{SO}(3)$, which act on the direction of rotation ϕ and on the spheres S^2 transverse to the rotation plane. The metric can then be written in the form

$$g_{ab}dx^a dx^b = -T(r, x)dt^2 + P(r, x)(d\phi + W(r, x)dt)^2 + S(r, x)d\Omega_{(2)}^2 \\ + A(r, x)dr^2 + B(r, x)dx^2 + 2F(r, x)drdx \quad (2.2)$$

and we denote the reference metric as

$$\bar{g}_{ab}dx^a dx^b = -T_0(r, x)dt^2 + P_0(r, x)(d\phi + W_0(r, x)dt)^2 + S_0(r, x)d\Omega_{(2)}^2 \\ + A_0(r, x)dr^2 + B_0(r, x)dx^2. \quad (2.3)$$

The compact radial direction $r \in [0, 1)$ covers the region from the horizon at $r = 0$, to infinity at $r = 1$. We seek solutions with horizons that are topologically S^4 , so we choose sections at constant t and r to also be topological S^4 's. The size of the ϕ -circles and of the symmetric S^2 's varies along the polar angular direction $x \in [0, 1]$, with $x = 0$ corresponding to the rotation axis (where ϕ -circles shrink to zero) and $x = 1$ to the equatorial plane (where S^2 spheres shrink to zero). The ‘‘bumpiness’’ of the horizon corresponds to non-monotonicity (of, say, the size of the S^2 on the horizon) along this polar direction.

We write the metric functions as

$$\begin{aligned}
T(r, x) &= T_0(r, x)Q_1(r, x), \\
W(r, x) &= W_0(r, z)Q_2(r, x), \\
P(r, x) &= P_0(r, x)Q_3(r, x), \\
S(r, x) &= S_0(r, x)Q_4(r, x), \\
A(r, x) &= A_0(r, x)Q_5(r, x), \\
B(r, x) &= B_0(r, x)Q_6(r, x), \\
F(r, x) &= \frac{rx(1-x^2)}{(1-r^2)^3}Q_7(r, x)
\end{aligned} \tag{2.4}$$

and the reference metric is the MP metric with a small modification that enables us to control the temperature of the solutions.

In order to obtain the functions (T_0, W_0, \dots etc.) for the reference metric we begin with the single-spin MP metric in standard Boyer-Lindquist-like coordinates (here \bar{r} , ϕ , \bar{t} and θ)

$$\begin{aligned}
ds^2 &= -d\bar{t}^2 + \frac{r_0^3}{\bar{r}\rho^2} (d\bar{t} + a \sin^2 \theta d\bar{\phi})^2 + (\bar{r}^2 + a^2) \sin^2 \theta d\bar{\phi}^2 \\
&+ \frac{\rho^2}{\Delta} d\bar{r}^2 + \rho^2 d\theta^2 + \bar{r}^2 \cos^2 \theta d\Omega_{(2)}^2
\end{aligned} \tag{2.5}$$

where

$$\rho^2 = \bar{r}^2 + a^2 \cos^2 \theta, \quad \Delta = \bar{r}^2 + a^2 - \frac{r_0^3}{\bar{r}} \tag{2.6}$$

and the $d\Omega_{(2)}^2$ is the line element of a 2-sphere. The horizon ($\bar{r} = r_+$) is found by solving

$$\Delta(r_+) = r_+^2 + a^2 - \frac{r_0^3}{r_+} = 0, \tag{2.7}$$

the mass and angular momentum are

$$M_{MP} = \frac{r_0^3 \Omega_{(4)}}{4\pi G}, \quad J_{MP} = \frac{aM_{MP}}{2}, \tag{2.8}$$

where $\Omega_{(4)}$ is the area of a unit 4-sphere, and the temperature and angular velocity are

$$\mathcal{T}_{MP} = \frac{1}{4\pi} \left(\frac{2r_+^2}{r_0^3} + \frac{1}{r_+} \right), \quad \Omega_H = \frac{a}{a^2 + r_+^2}. \tag{2.9}$$

We perform the changes of coordinates

$$\bar{r} = \frac{r_+}{1-r^2}, \quad \cos \theta = 1-x^2, \quad \bar{\phi} = \phi + \Omega_H t, \quad \bar{t} = t. \tag{2.10}$$

The first two are made so that the ranges of the coordinates are $0 < r, x < 1$ and the third change, to co-rotating coordinates, is made because otherwise the W_0 function goes to zero too fast at infinity, which is inconvenient for numerical calculation. In co-rotating coordinates the function W_0 is 0 at the horizon and Ω_H asymptotically.

The MP metric then takes the form

$$ds_{MP}^2 = -T_{MP}(r, x)dt^2 + P_0(r, x)(d\phi + W_0(r, x)dt)^2 + A_0(r, x)dr^2 + B_0(r, x)dx^2 + S_0d\Omega_{(2)}^2 \quad (2.11)$$

with

$$T_{MP}(r, x) = \frac{r^2 (f(r)^2 r_0^3 + g(r)r_+^3) (f(x)^2 (f(r)^2 r_0^3 + r^2 g(r)r_+^3) + r^2 x^2 g(x)r_+^3)}{(f(r)^2 r_0^3 + r^2 g(r)r_+^3)^2 - r^2 x^2 f(r)^2 g(x) (r_0^3 - r_+^3) (f(r)^2 r_0^3 + g(r)r_+^3)}, \quad (2.12)$$

where

$$f(r) = 1 - r^2, \quad g(r) = 2 - r^2. \quad (2.13)$$

We will find bumpy black hole solutions with given values of the temperature and angular velocity. It is convenient to specify these in terms of parameters of the reference metric. In order to control the temperature, we introduce a parameter k in the reference metric

$$T_0(r, x) = \frac{r^2 (f(r)^2 r_0^3 k + g(r)r_+^3) (f(x)^2 (f(r)^2 r_0^3 + r^2 g(r)r_+^3) + r^2 x^2 g(x)r_+^3)}{(f(r)^2 r_0^3 + r^2 g(r)r_+^3)^2 - r^2 x^2 f(r)^2 g(x) (r_0^3 - r_+^3) (f(r)^2 r_0^3 + g(r)r_+^3)} \quad (2.14)$$

so that the surface gravity κ of the reference metric is given by

$$\kappa^2 = \left. \frac{T_0(r, x)}{r^2 A_0(r, x)} \right|_{r \rightarrow 0} = \frac{1}{4r_+^2} (r_0^3 k + 2r_+^3) (r_0^3 + 2r_+^3). \quad (2.15)$$

Obviously, whenever $k \neq 1$ the reference metric is not a solution of Einstein's equations but nonetheless it has a smooth horizon. However, k allows us to move along the branches of solutions by varying it as a parameter in the reference metric. We will choose boundary conditions on the Q 's at the horizon in such a way that the surface gravity of the bumpy black holes is also given by (2.15). Note that by modifying k not only the temperature but also the mass and angular momentum of the solutions change. However, with the appropriate boundary conditions, Ω_H remains unchanged.

2.1 Boundary conditions

The conditions we impose on the Q 's at each of the boundaries of our domain in order to get regular solutions are

Horizon ($r = 0$): the reference metric is already regular on the horizon. Since the spacetime metric is the reference metric multiplied by the Q 's, we ensure regularity on the horizon by imposing Neumann boundary conditions $\partial_r Q|_{r=0} = 0$. In addition we impose $Q_1(0, x) = Q_5(0, x)$, which fixes the surface gravity to the value (2.15).

Axis ($x = 0$): the reference metric is already regular on the axis of rotation so again we impose Neumann boundary conditions $\partial_x Q|_{x=0} = 0$. The ϕ circle goes to zero at this boundary and in order to avoid a conical singularity we impose $Q_3(r, 0) = Q_6(r, 0)$.

Equator ($x = 1$): the boundary conditions are again Neumann $\partial_x Q|_{x=1} = 0$. Since here the radius of the S^2 shrinks to zero size, we impose $Q_4(r, 1) = Q_6(r, 1)$ to avoid a conical singularity.

Infinity ($r = 1$): for asymptotically flat (AF) solutions, since the reference metric is already AF, we impose the Dirichlet boundary conditions

$$Q_{i=1,\dots,6}(1, x) = 1, \quad Q_7(1, x) = 0, \quad (2.16)$$

so that the asymptotics are unchanged by the Q 's. Since we are in co-rotating coordinates the horizon angular velocity relative to infinity is given by the asymptotic value of $W(r, x)$. Then the condition $Q_2(1, x) = 1$ ensures that Ω_H is given by the same expression as in the MP black hole.

2.2 Physical magnitudes

Given our choice of boundary conditions, the temperature and the angular velocity at the horizon are easily extracted in terms of quantities present in the reference metric, namely, r_0 , k and r_+ , so that

$$\mathcal{T} = \frac{1}{4\pi r_+} \sqrt{(r_0^3 k + 2r_+^3)(r_0^3 + 2r_+^3)}, \quad \Omega_H = \frac{\sqrt{r_+(r_0^3 - r_+^3)}}{r_0^3}. \quad (2.17)$$

Since we work with vacuum solutions, we can obtain the mass and angular momentum by evaluating their Komar integrals at the horizon,

$$M = \frac{1}{12\pi G} \int_H *d\chi, \quad J = \frac{-1}{16\pi G} \int_H *d\zeta, \quad (2.18)$$

where χ is the 1-form dual to the asymptotic time-translation Killing vector $\partial_t - \Omega_H \partial_\phi$, and ζ is dual to the axial Killing vector ∂_ϕ . In addition to these quantities we also compute the area of the horizon. In order to compare different solutions that have the same mass we use the dimensionless quantities

$$\begin{aligned} a_H^{D-3} &= c_a \frac{\mathcal{A}_H^{D-3}}{(GM)^{D-2}}, & j^{D-3} &= c_j \frac{J^{D-3}}{GM^{D-2}}, \\ \omega_H &= c_\omega \Omega_H (GM)^{1/(D-3)}, & t_H &= c_t \mathcal{T} (GM)^{1/(D-3)}, \end{aligned} \quad (2.19)$$

with the numerical factors c_a, c_j, c_ω, c_t chosen as in [3].

Other geometric invariant quantities that are of interest for characterizing the solutions are the radii on the horizon ($r = 0$) of the circles parallel to the plane of rotation, $R_{\parallel}(x)$, and of the spheres S^2 orthogonal to it, $R_{\perp}(x)$. They are given by

$$R_{\parallel}(x) = \sqrt{P(0, x)}, \quad R_{\perp}(x) = \sqrt{S(0, x)}. \quad (2.20)$$

We render these dimensionless by dividing them by $(GM)^{1/(D-3)}$ without any additional factors.

We will often use j as the ‘control parameter’ that changes along a branch of solutions. The bumpy branches extend over rather narrow ranges of j . They originate at bifurcation points in the MP family given respectively by

$$(\pm)_{1,2,3} \text{ beginning : } j = 1.20, 1.41, 1.57. \quad (2.21)$$

The (+)-branches initially extend towards larger values of j , but then bend backwards towards decreasing j , which we have followed down to

$$(+)_{1,2,3} \text{ end : } j = 1.13, 1.20, 1.55. \quad (2.22)$$

Along the (−)-branches, j decreases away from the bifurcation, and the lowest values we have attained are

$$(-)_{1,2,3} \text{ end : } j = 1.11, 1.36, 1.53. \quad (2.23)$$

3 Geometry of bumpy black holes

In this section we explore the geometry of the solutions, in particular of their horizons. Since we have pushed the new branches close to their endpoints in solution space, one purpose is to examine whether the critical solutions of (+) branches have singularities modeled by Ricci-flat double-cone geometries that can mediate the transitions to black ring, black Saturn, and multi-ring solutions [10]. Such structures in topology-changing transitions were first argued to be present in the context of Kaluza-Klein black holes [11] and have been extensively studied, see [12, 16–29], and [30] for a recent review of the subject.

Another aim is to get a better understanding of the solutions in the (−) branches, in particular where and how these branches end.

The spatial horizon geometry, $r = 0$, $t = \text{constant}$, is

$$ds_H^2 = B(0, x)dx^2 + R_{\parallel}^2(x)d\phi^2 + R_{\perp}^2(x)d\Omega_{(2)}^2. \quad (3.1)$$

In order to gain some intuitive understanding of these geometries, we perform two kinds of plots: embedding diagrams of sections of the horizon into Euclidean space, and plots of the invariant radii of the S^1 and S^2 symmetry cycles.

Embedding diagrams. Embeddings in Euclidean space provide useful and intuitive visualizations of the geometry. Here we use the same type of embeddings as ref. [15] presented for black rings. On the spatial horizon geometry we choose a section $\phi = \text{const.}$,

$$ds_{sec}^2 = B(0, x)dx^2 + R_{\perp}^2(x)d\Omega_{(2)}^2, \quad (3.2)$$

and embed it in \mathbf{E}_4

$$ds_{\mathbf{E}_4}^2 = du^2 + d\rho^2 + \rho^2 d\Omega_{(2)}^2 \quad (3.3)$$

as a surface of the form

$$\rho = R_{\perp}(x), \quad u = u(x), \quad (3.4)$$

so the induced geometry is

$$ds_{emb}^2 = (R'_\perp(x)^2 + u'(x)^2)dx^2 + R_\perp^2(x)d\Omega_{(2)}^2. \quad (3.5)$$

The embedding is found by integrating

$$u(x) = \int_0^x d\bar{x} \sqrt{B(0, \bar{x}) - R'_\perp(\bar{x})^2}, \quad (3.6)$$

which is possible since $B(0, x) \geq R'_\perp(x)^2$ for all our solutions. In our plots we present $R_\perp(x)$ versus $u(x)$.

The coordinate u does not have any invariant meaning as the radius of the rotational S^1 's, since this representation misses the information about $R_\parallel(x)$. For this, we employ a different type of plot.²

Invariant-radii plots. These are plots of $R_\perp(x)$ versus $R_\parallel(x)$. Information about the length in the polar direction is lost now, which makes the horizon shapes in these plots look somewhat peculiar.

3.1 (+)-branch bumpy black holes

Representative solutions of these branches are depicted in embedding diagrams in figure 3 and in invariant-radii diagrams in figure 4. Observe that, contrary to what may seem from the embedding diagrams, the radius R_\parallel of the S^1 near the equator is larger in MP black holes than in the bumpy solutions with the same mass and angular momentum.

Near the values (2.22) the solutions clearly approach configurations where a symmetric S^2 on the horizon pinches down to zero size, developing a singularity whose structure we analyze next.

3.1.1 Critical cone geometries

Depending on whether the singular pinch-off occurs along the rotation axis or on a circle away from the axis, the geometries are expected to be locally Lorentzian double-cones of the form

$$ds_{\text{on-axis}}^2 = dz^2 + \frac{2z^2}{D-2} \left(-\cos^2 \chi dt^2 + d\chi^2 + \sin^2 \chi d\phi^2 + \frac{D-5}{2} d\Omega_{(D-4)}^2 \right), \quad (3.7)$$

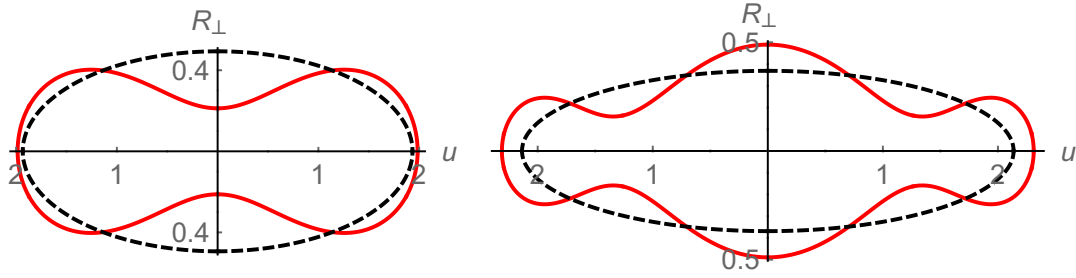
$$ds_{\text{off-axis}}^2 = dz^2 + L^2 d\phi^2 + \frac{z^2}{D-3} \left(-\cos^2 \chi dt^2 + d\chi^2 + (D-5) d\Omega_{(D-4)}^2 \right), \quad (3.8)$$

with horizons at $\chi = \pi/2$, and where L is the radius of the circle where the S^2 pinch to zero [10].

If we embed the section $t = \text{const}$, $\chi = \pi/2$ of these geometries in Euclidean space as above, then it is easy to see that they are represented as the cones

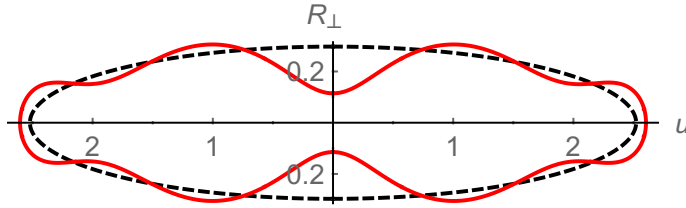
$$\text{on-axis: } u = \sqrt{\frac{3}{D-2}} z, \quad \text{off-axis: } u = \sqrt{\frac{2}{D-3}} z. \quad (3.9)$$

²Embedding the (x, ϕ) part of the horizon in this manner fails at large rotations, as in the case of the Kerr solution. A different kind of embedding is nevertheless possible [6].



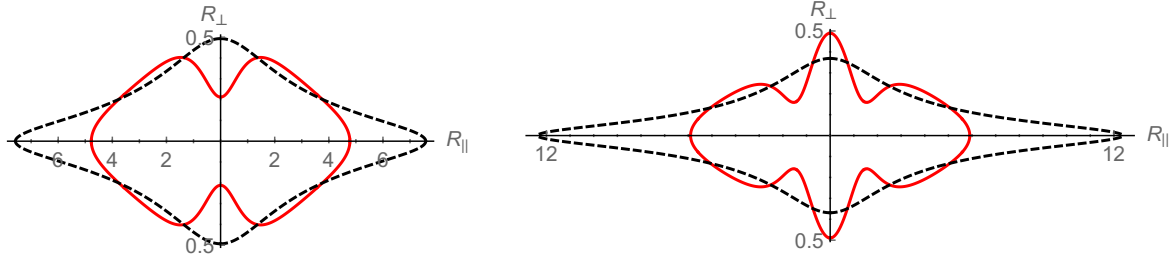
(a) $(+)_1$ black hole at $j = 1.17$.

(b) $(+)_2$ black hole at $j = 1.36$.



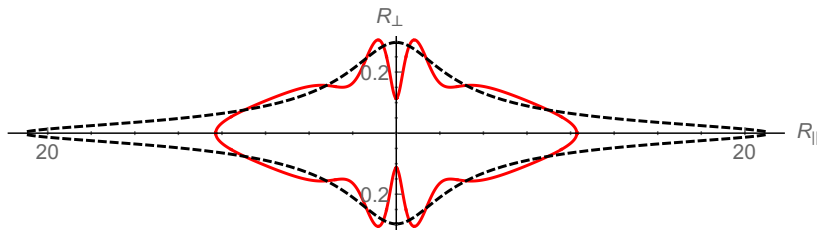
(c) $(+)_3$ black hole at $j = 1.56$.

Figure 3. Isometric embeddings for representative black holes in the $(+)_1,2,3$ branches. R_\perp is the radius of the S^2 orthogonal to the rotation plane and u is a coordinate of Euclidean flat space, see (3.3) and (3.6). The dashed black curve shows the embedding of a MP black hole of the same mass and angular momentum.



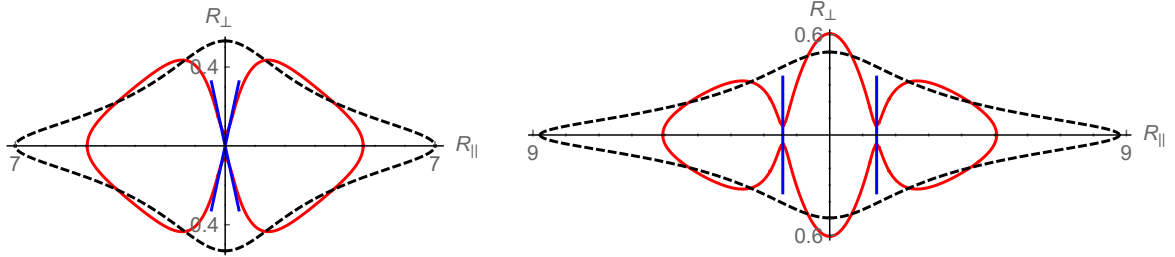
(a) $(+)_1$ black hole at $j = 1.17$.

(b) $(+)_2$ black hole at $j = 1.36$.



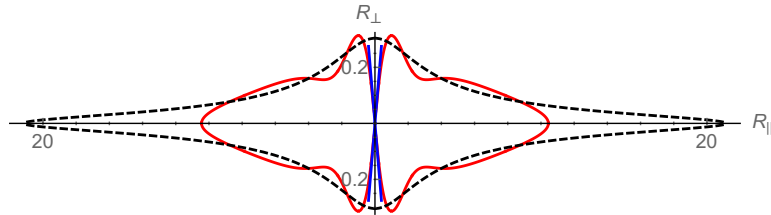
(c) $(+)_3$ black hole at $j = 1.56$.

Figure 4. Invariant-radii plots for the same black holes as in figure 3. R_\parallel is the radius of circles parallel to the rotation plane and R_\perp is the radius of the orthogonal S^2 . The black dashed curve shows a MP black hole of the same mass and angular momentum.



(a) $(+)_1$ -branch black hole at $j = 1.13$, close to the transition to a black ring.

(b) $(+)_2$ -branch black hole at $j = 1.20$, close to the transition to a black Saturn.



(c) $(+)_3$ -branch black hole at $j = 1.55$, close to the transition to a bumpy black ring.

Figure 5. Invariant-radii diagrams of bumpy black hole horizons of the $(+)_1,2,3$ branches (red curves), for the largest deformations we have obtained. We superimpose the MP black holes with the same mass and spin (dashed black), and the plots for the conifolds eq. (3.10) (blue).

We can superimpose these on the most deformed solutions we have obtained in these branches. Figure 1 shows excellent agreement with the prediction of [10].

The invariant-radii plots probe complementary geometric aspects of the horizon. The geometries (3.7), (3.8) have slopes

$$\text{on-axis: } \frac{dR_{\perp}}{dR_{\parallel}} = \sqrt{\frac{D-5}{2}}, \quad \text{off-axis: } \frac{dR_{\perp}}{dR_{\parallel}} \rightarrow \infty, \quad (3.10)$$

which are also very well reproduced on-axis for $(+)_1,3$, see figure 5, but less well so off-axis for $(+)_2$, reflecting (maybe unsurprisingly) a remaining small dependence of R_{\parallel} on the polar angle that would become negligible only much closer to the critical singularity.

We also compare the Kretschmann scalar

$$K = R_{\mu\nu\rho\sigma}R^{\mu\nu\rho\sigma} \quad (3.11)$$

of both geometries, following the study in [18] of the conical waist of inhomogeneous black strings. For the cones, K depends only on the ‘polar’ coordinate z while for the black holes it depends not only on x but also on r . In order to make the comparison we must specify a way to map points between the two geometries, i.e., a function $z(r, x)$. This involves a certain arbitrariness, which we fix by equating the radius of the 2-sphere in both geometries. Then (in six dimensions)

$$\text{on-axis: } S(r, x) = \frac{z^2}{4}, \quad \text{off-axis: } S(r, x) = \frac{z^2}{3} \quad (3.12)$$

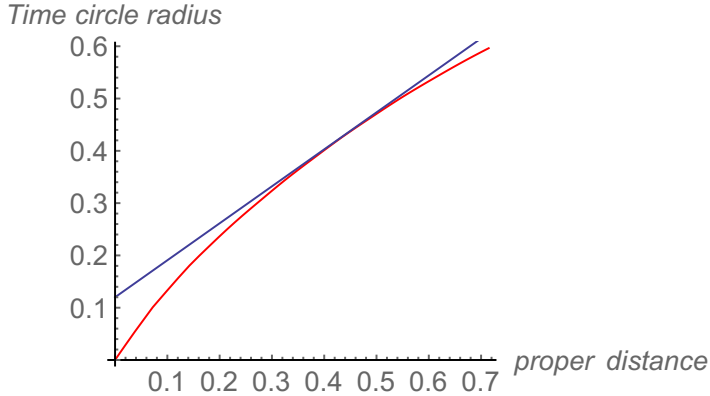


Figure 6. Circular-radius of the Euclidean time circle as a function of the proper distance to the horizon along the rotation axis, in the $(+)_1$ black hole at $j = 1.13$. The slope matches well that of the cone geometry (blue) as the black hole is approached, although not very close to the horizon where the singular cone is smoothed in our solution.

and so

$$K_{\text{on-axis cone}} = \frac{72}{z^4} = \frac{9}{2S(r, x)^2}, \quad K_{\text{off-axis cone}} = \frac{48}{z^4} = \frac{16}{3S(r, x)^2}. \quad (3.13)$$

These comparisons are dominated by how the size of the S^2 shrink close to the singularity, including away from the horizon, but they do not test the length of the equatorial S^1 , to which K is largely insensitive.

We have computed the discrepancy between the Kretschmann scalars of both geometries, $\left| \frac{K_{\text{bh}}}{K_{\text{cone}}} - 1 \right|$, for the three branches and it is less than 10% (often less than 5%) in the region near the singularity. Therefore, we conclude that the critical cones are locally a good description of the singular region.

Finally, we have also checked the appearance of a conical structure in the Euclidean time direction. Figure 6 shows the rate at which the Euclidean time circle shrinks along the axis of rotation in our nearest-to-critical $(+)_1$ solution.³ The slope in this curve fits well the slope of the conical solution over a range of distances close to the black hole. It departs from it very near the horizon, as it must since the cone is smoothed in our solution.⁴

3.1.2 $(+)_3$: transition to bumpy black rings

It was naturally conjectured in ref. [3] that black holes along the $(+)_1, 2$ branches would pinch to zero and transition to black ring and black Saturn phases, respectively. However, higher branches $(+)_i, i \geq 2$ have multiple pinches and it was less clear what their fate could be. If pinch-down occurred first on a circle off-axis, then the branch $(+)_3$ would transition to a black Saturn configuration with a bumpy central black hole. However, the deformation of $(+)_3$ black holes is expected to be larger on-axis than off-axis. The reason is that in the black membrane limit of the MP black holes, and for small, linearized perturbations, the

³Close to the horizon, and in corotating coordinates, the geometry is very approximately static and one can sensibly talk about the Euclidean time circle.

⁴In fact, very close to the horizon the slope in this plot must become the same as the surface gravity.

axisymmetric Gregory-Laflamme-type perturbation takes the form [2]

$$\delta g_{\mu\nu} \sim J_0(x)h_{\mu\nu}(r), \quad (3.14)$$

where x is the distance from the rotation axis in directions parallel to the horizon, and hence plays the role of the polar angle. The Bessel function $J_0(x)$ yields larger deformations close to the axis of rotation at $x = 0$, and decays away from it. Figures 1 and 3 show that this behavior persists when the deformations are not small.

This evolution of the $(+)_3$ branch has a natural end at a topology-changing transition to a branch of *bumpy black rings*, of horizon topology $S^1 \times S^{D-3}$, with a deformed S^{D-3} . These have not been constructed yet, and our arguments are the first clear indication of their existence. It is also natural to expect that the bumpy black ring branch will connect, at its other end, to black di-rings. Indeed it seems implausible that they smooth out their deformations and connect to the known (smooth) black ring solutions, since these two branches are very far apart in solution space (see figure 10 below).

The argument also suggests that the same behavior occurs in higher branches, with pinches being larger closer to the axis, and pinching-down sequentially at increasing values of the polar angle x . The conifold-type transition then connects them to new families of multiply-bumpy black rings, which eventually, through several transitions, connect to multi-ring configurations.

3.2 $(-)$ -branch bumpy black holes

Figures 7 and 8 show the previous two types of graphics for the horizon geometry of these black holes at their largest deformation, (2.23) (these were also shown in figure 2).

From figure 8 we see that these horizons spread in the rotation plane more than the MP black holes of the same mass and spin. This could be anticipated near the bifurcation point, where the deformation is controlled by a zero-mode with $i + 1$ nodes: since the $(-)_i$ zero mode wavefunctions have sign $(-1)^{i+1}$ at the rotation axis, then the wavefunction at the equator must always be positive, i.e., the bumpy black hole bulges out.⁵ At least for the $i = 1$ solutions, we can also understand this in more physical terms: close to the branching point both solutions have the same mass, angular momentum and angular velocity. If the MP black hole is perturbed in such a way that some of its mass is concentrated closer to the axis of rotation, then in order to maintain the angular momentum constant (with the same angular velocity) some mass must also be moved farther along the rotation plane, preferably around the equator.

Further along the branch the horizons stretch a lot on the rotation plane, see figure 8, and get highly pancaked, $R_\perp \ll R_\parallel$. Nevertheless, in contrast to ultraspinning MP black holes, they do not seem to approach black membranes in the limit, and in particular (as we will see in section 4) they do not develop the Gregory-Laflamme zero modes of the Lichnerowicz operator characteristic of black membranes that would signal the appearance of new branches of solutions [31].

⁵The same argument implies that $(+)$ -branch black holes bulge out less at the equator than MP black holes of the same mass and spin, see figure 4.

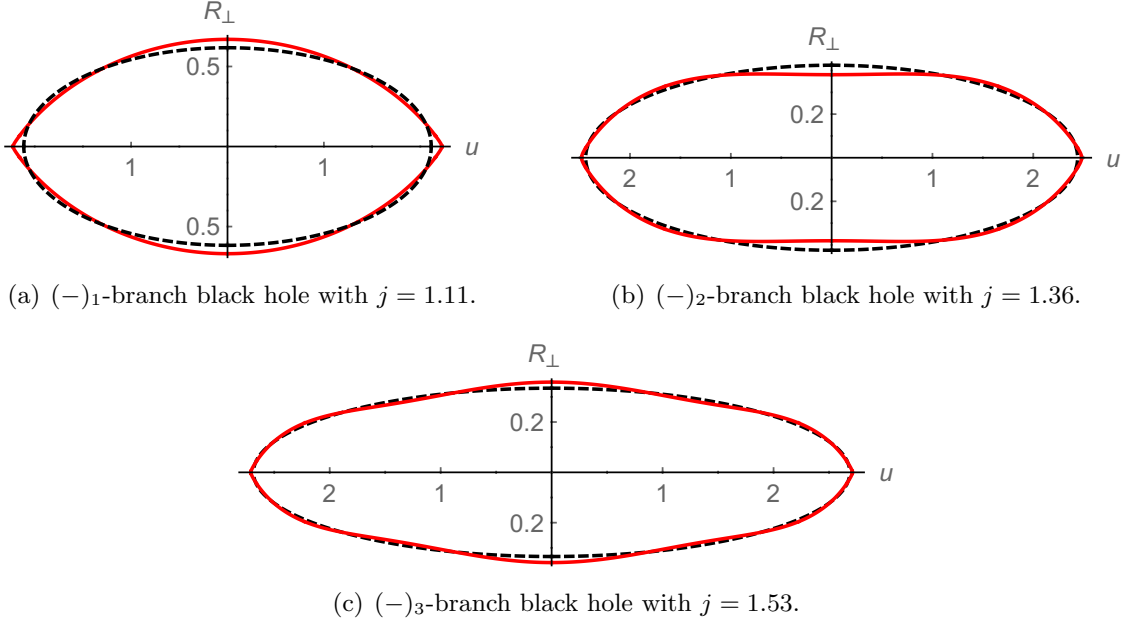


Figure 7. Isometric embeddings for bumpy black holes near the termination of the $(-)$ branches. R_{\perp} is the radius of the transverse S^2 and u is a coordinate of Euclidean flat space. The black dashed curve shows the embedding of a MP black hole of the same mass and angular momentum. The conical shapes at the equator have the same opening angle for the three branches, $u = \sqrt{2/3} z$.

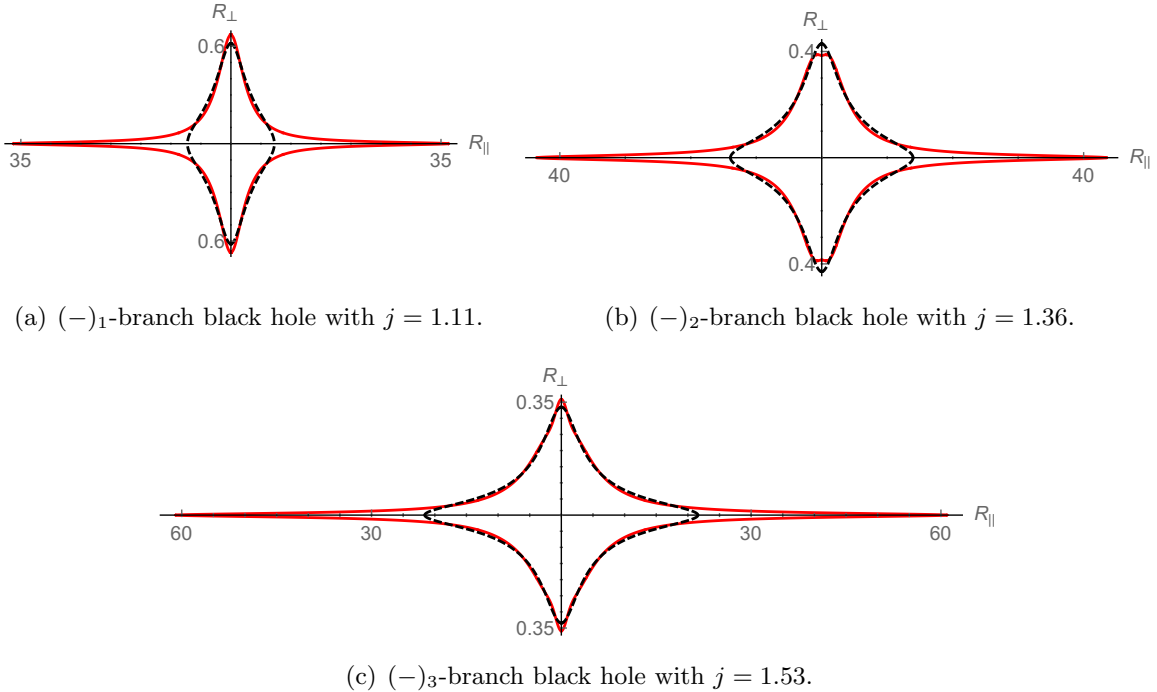


Figure 8. Invariant-radii plots for the same black holes as in figure 7. R_{\parallel} is the radius of circles parallel to the rotation plane and R_{\perp} is the radius of the orthogonal S^2 . The black dashed curve shows a MP black hole of the same mass and angular momentum.

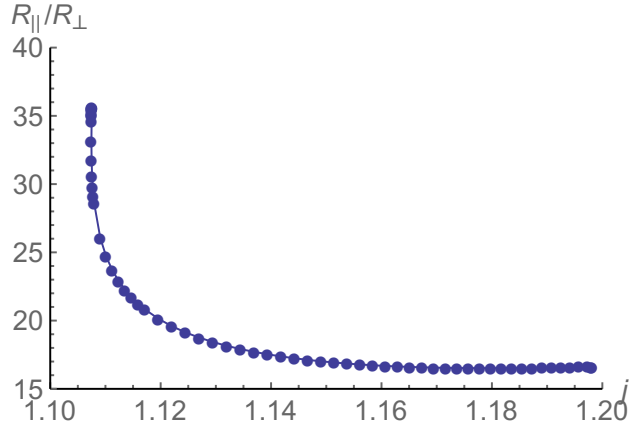


Figure 9. R_{\parallel}/R_{\perp} for $(-)_1$ bumpy black holes as a function of j . Note that j decreases as the solutions get farther from the MP bifurcation point. Close to the limiting value $j \approx 1.11$ the equatorial radius R_{\parallel} appears to diverge, both for fixed R_{\perp} and for fixed mass. The $(-)_2,3$ branches show similar behavior.

Figure 9 strongly suggests that the length of the equatorial circle diverges in the limiting solutions — even though the radial distance to the equator remains finite. This behavior is known to occur for the extremal limit of the five-dimensional MP black hole, although in the latter case the extremal solution has zero temperature and area, whereas these remain finite in the critical $(-)$ solutions.

The S^2 's on the equator shrink to zero in the limiting solutions in a singular way, causing the Kretschmann scalar to diverge. The effect seems to be the same in all three branches, being well reproduced on sections of constant t and ϕ on the horizon (such as are captured in figure 7, and by the Kretschmann scalar) by the geometry

$$ds^2 = dz^2 + \frac{z^2}{3}d\Omega_{(2)}, \quad (3.15)$$

which is also present in off-axis cones (3.8).

This suggests that the local structure of the singularity at the equator in these solutions may be universal for all $(-)$ branches: the S^2 shrink to zero along the horizon like in (3.15), while the length of the equatorial S^1 diverge.

Although we do not have a local model for the full singularity, it is not one of the conical geometries that effect a transition to another branch of black holes. In fact it seems unlikely that the singularity is a Ricci-flat scaling geometry. In view of this, and in the absence of a plausible candidate for a merger transition, we are led to conjecture that the $(-)$ branches of black holes terminate in phase space without continuing into any other singly-spinning stationary black hole solutions.

4 Phase diagrams, thermodynamic stability, and negative modes

In figure 10 we show the area, temperature and angular velocity as a function of the angular momentum for fixed mass. We can see the two different families of solutions branching off

from each of the perturbative zero modes. Since in figure 11 it is difficult to distinguish the two branches in the (j, a_h) plane, we also show plots of the area difference between the bumpy black holes and the MP solutions for values of j close to each branching point. The black ring phases obtained in [8] are also included in these plots, and it is apparent that the $(+)_1$ solutions tend to a merger point with the black rings. Although our results suggest that solution-trajectories inspiral close to this transition (which would lead to infinite discrete non-uniqueness of the kind found in [32–34]), our accuracy in this region is not enough to reach a definite conclusion.

Thermodynamic stability of these black holes in the grand-canonical ensemble is obtained when the specific heat at constant angular momentum \mathcal{C}_j and the isothermal moment of inertia ϵ are both positive [35]

$$\mathcal{C}_j = \left. \frac{dM}{dT} \right|_J > 0, \quad \epsilon = \left. \frac{dJ}{d\Omega_H} \right|_{\mathcal{T}} > 0. \quad (4.1)$$

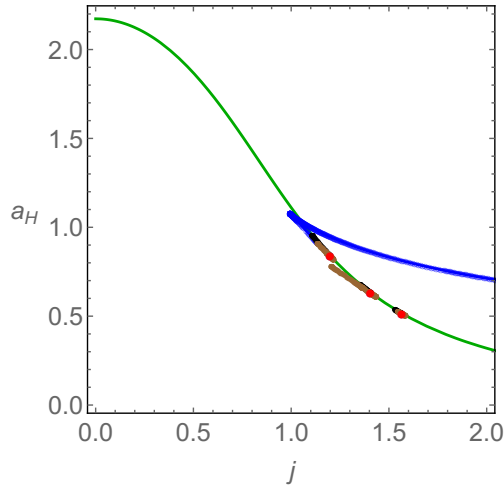
Negative moments of inertia are possible for black holes since they are not rigid bodies. They can reduce their angular velocity while gaining angular momentum by spreading in the rotation plane. This is precisely what happens in ultra-spinning MP black holes. In this case it is impossible for the black hole to remain in equilibrium with a co-rotating radiation reservoir.

The specific heat and moment of inertia can be read off from the slopes of the solution curves in the (\mathcal{T}, M) and (Ω_H, J) planes. The details of the plots for actual solutions are difficult to distinguish, so instead in figure 12 we present sketches of them that capture their qualitative features.

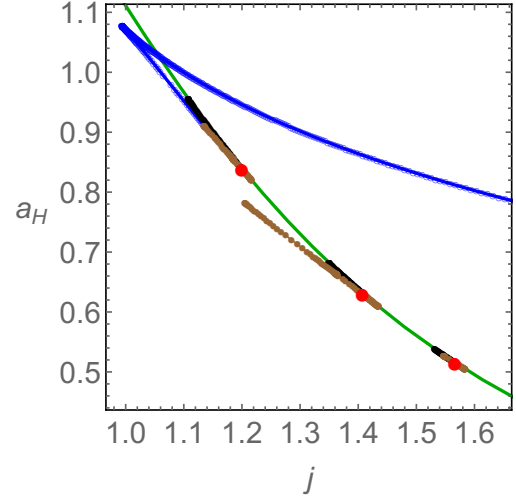
In addition, we have also studied the spectrum of the Lichnerowicz operator, since its negative eigenvalues are directly related to the negative modes of the quasi-Euclidean action. We have checked that the number of negative eigenvalues coincides with the expectations from thermodynamic stability. In particular, along the MP family of solutions in the direction of increasing j , initially the solutions have one negative mode that corresponds to negative specific heat (it is the MP extension of the Euclidean Schwarzschild negative mode), and acquire a second one at the cusp in the (Ω_H, J) plane where the moment of inertia first becomes negative. This is also the minimum of the temperature (see figure 10) which signals the entrance into the ultraspinning regime, and which coincides with the change of sign of ϵ . At higher j one encounters further zero modes that become negative ones. These are not associated to new thermodynamic instabilities, instead they are ‘overtones’ of Gregory-Laflamme-type negative modes.

The thermodynamic stability and negative modes along $(+)$ branches are more complicated, as there are several points where the susceptibilities (4.1) change sign. Here we explain it for $(+)_1$ solutions (higher $(+)$ branches exhibit the same qualitative behavior), referring to figure 12:

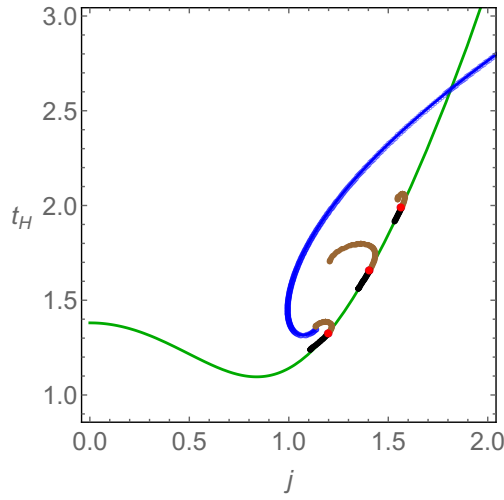
From O_1 to A_1 : Point O_1 is the bifurcation from the MP branch of solutions. The new branch bifurcates with higher area, hence the MP solution is expected to be less stable, and indeed it acquires an extra negative mode, while the bumpy solution keeps the number



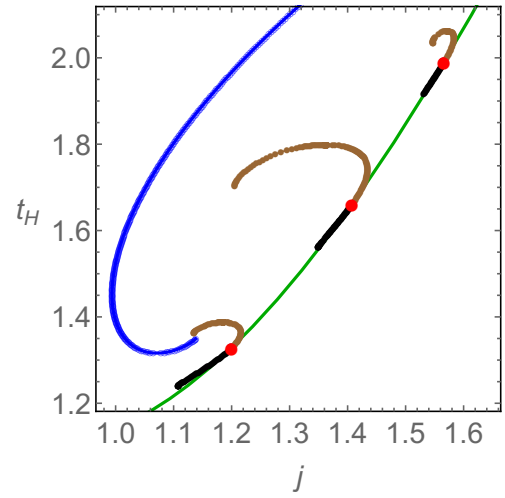
(a) Area a_H vs. spin j



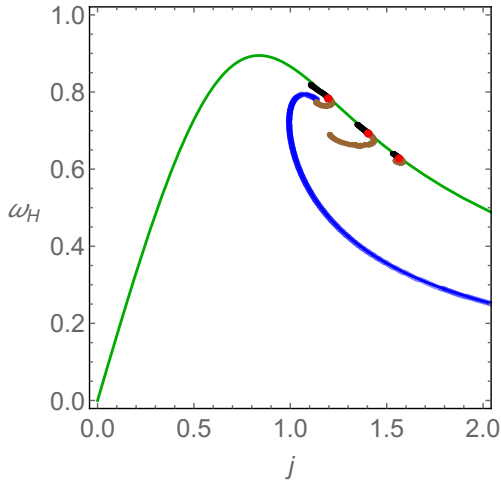
(b) Zoom of (a)



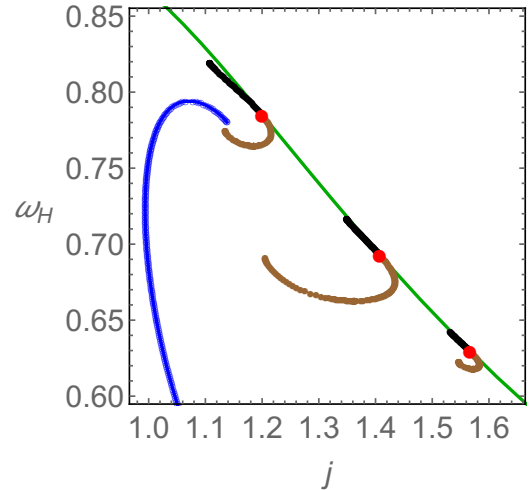
(c) Temperature t_H vs. spin j



(d) Zoom of (c)



(e) Angular velocity ω_H vs. spin j



(f) Zoom of (e)

Figure 10. Thermodynamic quantities. Green: MP black hole. Brown: (+)-branch bumpy black holes. Black: (-)-branch bumpy black holes. Blue: black rings (from [8]). Red dots: branching points from the zero modes found in [6].

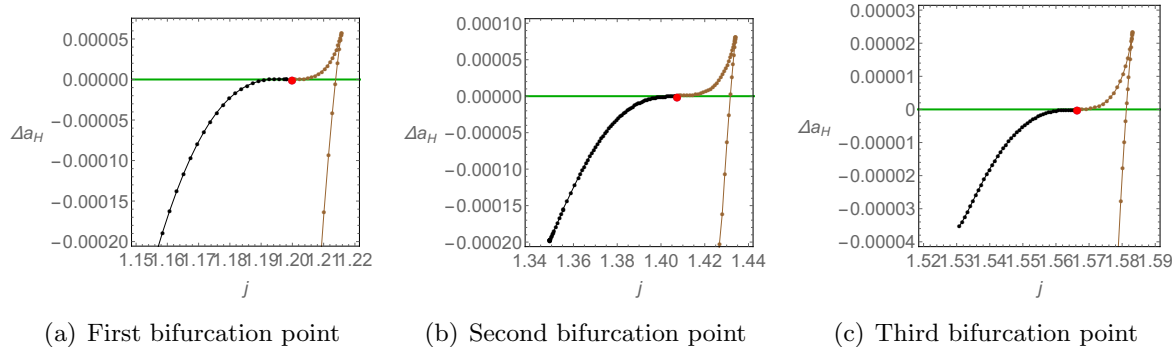


Figure 11. Area difference Δa_H between bumpy and MP black holes vs. angular momentum j . Color coding as in figure 10.

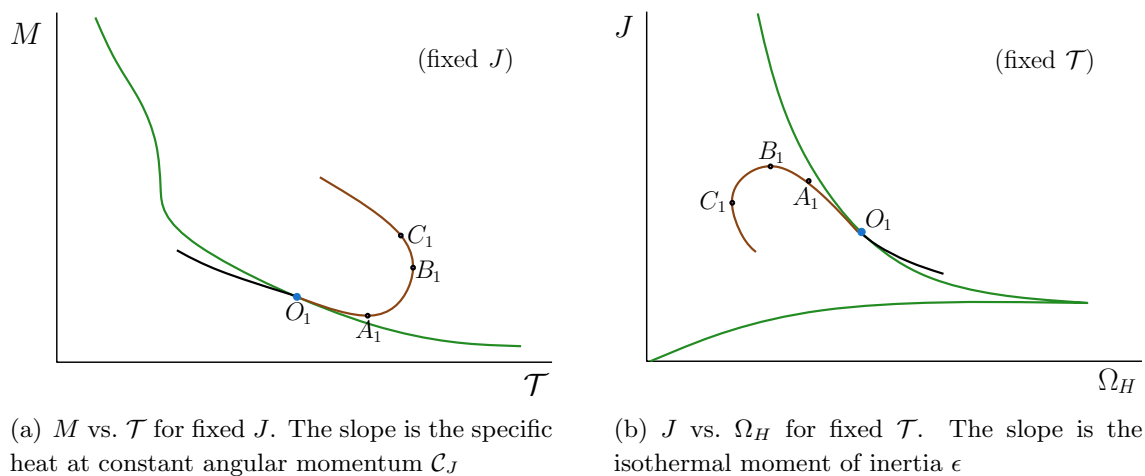


Figure 12. Sketch of phases in the (\mathcal{T}, M) and (Ω_H, J) planes (color coding as in figure 10). We only show the branches $(\pm)_1$, but $(\pm)_{2,3}$ have the same behavior. The branch $(+)_1$ (brown) has two negative modes from O_1 to C_1 and three from C_1 onwards, while the branch $(-)_1$ (black) always has three negative modes.

of negative modes present in the MP solutions just before O_1 . Both the specific heat and the moment of inertia are negative in this segment; accordingly, the Lichnerowicz operator on solutions from O_1 to A_1 has two negative eigenvalues.

From A_1 to B_1 : The point A_1 at which \mathcal{C}_j changes sign from negative to positive passing through zero corresponds to the cusp in the (j, a_h) plane in figure 10, where the branch beyond A_1 has lower area and \mathcal{C}_j remains positive until B_1 . But there is no qualitative change in the spectrum of the Lichnerowicz operator at A_1 . We interpret the two negative eigenvalues present here as due to the negative ϵ and to the fact that there exists another solution with higher area for the same j . Observe that a given negative mode does not strictly correspond to just one instability.

From B_1 to C_1 : At B_1 the sign of \mathcal{C}_j changes from positive to negative and the sign of ϵ from negative to positive. Like before, the number of negative modes is preserved and the

spectrum of the Lichnerowicz operator does not signal these changes in thermodynamic susceptibilities.

From C_1 : At C_1 the sign of ϵ changes from positive to negative going through infinity. The Lichnerowicz operator acquires a third negative mode.

We see that the (+)-branch solutions are always thermodynamically unstable, since either ϵ or \mathcal{C}_J or both are negative. The solutions are likely dynamically unstable to bar-mode perturbations, like MP black holes are at even lower values of j .

Regarding the (−) branches, they all have negative \mathcal{C}_j and ϵ . In addition they come out of the bifurcation with less area than the MP black holes. As expected from the arguments above, the Lichnerowicz operator on these solution has three negative eigenvalues. We also expect them to be dynamically unstable to bar-mode deformations.

Acknowledgments

We are very grateful to Óscar Dias, Jorge Santos and Benson Way for very useful discussions and for generously supplying the numerical data for black rings used in figure 10. This work started during the COST Short Term Scientific Mission COST-STSM-MP1210-15750. MM thanks DAMTP, Cambridge, for kind hospitality during her visit. Part of this work was done during the workshop “Holographic vistas on Gravity and Strings” YITP-T-14-1 at the Yukawa Institute for Theoretical Physics, Kyoto University, whose kind hospitality we all acknowledge. MM is also grateful to the String Theory Group at NTU (Taiwan) for warm hospitality. RE and MM are supported by MEC FPA2010-20807-C02-02, FPA2013-46570-C2-2-P, AGAUR 2009-SGR-168 and CPAN CSD2007-00042 Consolider-Ingenio 2010. PF is supported by the European Research Council grant no. ERC-2011-StG279363-HiDGR and also by the Stephen Hawking Advanced Research Fellowship from Centre for Theoretical Cosmology, University of Cambridge. MM is supported by an FI Fellowship of AGAUR, Generalitat de Catalunya, 2013FI.B 00840.

A Numerics

In this appendix we explain the details of our numerical construction of the bumpy black holes.

Plugging the ansatz (2.2) and the reference metric (2.3) into the Einstein-DeTurck equations gives a system of partial differential equations that we solve numerically.

First we discretize the system using Chebyshev points. We need more resolution in the angular x coordinate than in the radial r one, so we use conforming patches, see figure 13 for an example. This is computationally cheaper than having one bigger grid and gives us the flexibility of increasing the resolution just where it is necessary. This type of patches coincide along one line of points (no overlapping regions), in the present situation they coincided along a line of constant x . We used 2 to 5 patches depending on various factors. Higher zero modes have more bumps (the Q ’s vary more along x) and we need more resolution. Close to transitions the functions become singular and therefore we need

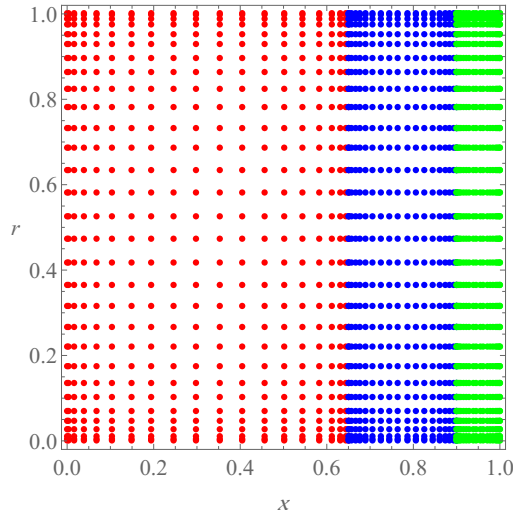


Figure 13. Grid used for some solutions. Each of the three patches (red, blue, green) has 30 points in the r direction and 20 in the x direction.

to concentrate more points in a specific part of the domain. We impose continuity of the functions and the first derivatives as boundary conditions between the patches.

Once discretized, we solve the system by an iterative Newton-Raphson method. Since this method needs a seed, we first solve the linearized problem, find the eigenvectors that correspond to the zero modes and use them (ref. metric perturbed with the eigenvector) as a seed for the first solution in each of the branches. Once we have solved the nonlinear problem, we move along the branch by using the previous solution as a seed and by changing the value of k in the background metric. We keep $r_0 = 1$ in all the solutions.

For the standard branches that connect the MP black hole with the black ring, black Saturn and black diring, we begin by increasing the temperature. At some point the branches reach a maximum of the temperature and in order to go past it we keep k fixed and vary r_+ instead. The solutions close to this maximum are tricky to obtain because the Lichnerowicz operator has a near zero mode, but once we pass it the following solutions are easily obtained by lowering the temperature (decreasing k with fixed r_+). The other type of branches do not have any extrema of the temperature and to obtain them we always decrease k .

As for the resolution used, we began with two patches of 20×20 in the branches $(+)_1,2$ (heading towards the black ring and black saturn) and with four patches of 30×20 for the $(+)_3$ branch (heading towards the diring); we began with similar resolutions for the other branches. In order to know when to increase the resolution we estimated the numerical error in the physical quantities and if it was greater than a few percent we decided that more resolution was needed. We have also checked that our numerical solutions converge to the continuum limit according to our discretization scheme.

Open Access. This article is distributed under the terms of the Creative Commons Attribution License ([CC-BY 4.0](https://creativecommons.org/licenses/by/4.0/)), which permits any use, distribution and reproduction in any medium, provided the original author(s) and source are credited.

References

- [1] R.C. Myers and M.J. Perry, *Black Holes in Higher Dimensional Space-Times*, *Annals Phys.* **172** (1986) 304 [[INSPIRE](#)].
- [2] R. Emparan and R.C. Myers, *Instability of ultra-spinning black holes*, *JHEP* **09** (2003) 025 [[hep-th/0308056](#)] [[INSPIRE](#)].
- [3] R. Emparan, T. Harmark, V. Niarchos, N.A. Obers and M.J. Rodriguez, *The Phase Structure of Higher-Dimensional Black Rings and Black Holes*, *JHEP* **10** (2007) 110 [[arXiv:0708.2181](#)] [[INSPIRE](#)].
- [4] R. Emparan and P. Figueras, *Multi-black rings and the phase diagram of higher-dimensional black holes*, *JHEP* **11** (2010) 022 [[arXiv:1008.3243](#)] [[INSPIRE](#)].
- [5] O.J.C. Dias, P. Figueras, R. Monteiro, J.E. Santos and R. Emparan, *Instability and new phases of higher-dimensional rotating black holes*, *Phys. Rev. D* **80** (2009) 111701 [[arXiv:0907.2248](#)] [[INSPIRE](#)].
- [6] O.J.C. Dias, P. Figueras, R. Monteiro and J.E. Santos, *Ultraspinning instability of rotating black holes*, *Phys. Rev. D* **82** (2010) 104025 [[arXiv:1006.1904](#)] [[INSPIRE](#)].
- [7] B. Kleihaus, J. Kunz and E. Radu, *Black rings in six dimensions*, *Phys. Lett. B* **718** (2013) 1073 [[arXiv:1205.5437](#)] [[INSPIRE](#)].
- [8] O.J.C. Dias, J.E. Santos and B. Way, *Rings, Ripples and Rotation: Connecting Black Holes to Black Rings*, *JHEP* **07** (2014) 045 [[arXiv:1402.6345](#)] [[INSPIRE](#)].
- [9] B. Kleihaus, J. Kunz and E. Radu, *Black ringoids: spinning balanced black objects in $d \geq 5$ dimensions — the codimension-two case*, [arXiv:1410.0581](#) [[INSPIRE](#)].
- [10] R. Emparan and N. Haddad, *Self-similar critical geometries at horizon intersections and mergers*, *JHEP* **10** (2011) 064 [[arXiv:1109.1983](#)] [[INSPIRE](#)].
- [11] B. Kol, *Topology change in general relativity and the black hole black string transition*, *JHEP* **10** (2005) 049 [[hep-th/0206220](#)] [[INSPIRE](#)].
- [12] M. Headrick, S. Kitchen and T. Wiseman, *A New approach to static numerical relativity and its application to Kaluza-Klein black holes*, *Class. Quant. Grav.* **27** (2010) 035002 [[arXiv:0905.1822](#)] [[INSPIRE](#)].
- [13] P. Figueras, J. Lucietti and T. Wiseman, *Ricci solitons, Ricci flow and strongly coupled CFT in the Schwarzschild Unruh or Boulware vacua*, *Class. Quant. Grav.* **28** (2011) 215018 [[arXiv:1104.4489](#)] [[INSPIRE](#)].
- [14] A. Adam, S. Kitchen and T. Wiseman, *A numerical approach to finding general stationary vacuum black holes*, *Class. Quant. Grav.* **29** (2012) 165002 [[arXiv:1105.6347](#)] [[INSPIRE](#)].
- [15] H. Elvang, R. Emparan and A. Virmani, *Dynamics and stability of black rings*, *JHEP* **12** (2006) 074 [[hep-th/0608076](#)] [[INSPIRE](#)].
- [16] T. Wiseman, *Static axisymmetric vacuum solutions and nonuniform black strings*, *Class. Quant. Grav.* **20** (2003) 1137 [[hep-th/0209051](#)] [[INSPIRE](#)].
- [17] T. Wiseman, *From black strings to black holes*, *Class. Quant. Grav.* **20** (2003) 1177 [[hep-th/0211028](#)] [[INSPIRE](#)].
- [18] B. Kol and T. Wiseman, *Evidence that highly nonuniform black strings have a conical waist*, *Class. Quant. Grav.* **20** (2003) 3493 [[hep-th/0304070](#)] [[INSPIRE](#)].

- [19] T. Harmark and N.A. Obers, *New phase diagram for black holes and strings on cylinders*, *Class. Quant. Grav.* **21** (2004) 1709 [[hep-th/0309116](#)] [[INSPIRE](#)].
- [20] T. Harmark and N.A. Obers, *Phase structure of black holes and strings on cylinders*, *Nucl. Phys.* **B 684** (2004) 183 [[hep-th/0309230](#)] [[INSPIRE](#)].
- [21] B. Kol, E. Sorkin and T. Piran, *Caged black holes: black holes in compactified space-times. 1. Theory*, *Phys. Rev.* **D 69** (2004) 064031 [[hep-th/0309190](#)] [[INSPIRE](#)].
- [22] E. Sorkin, B. Kol and T. Piran, *Caged black holes: black holes in compactified space-times. 2. 5 – D numerical implementation*, *Phys. Rev.* **D 69** (2004) 064032 [[hep-th/0310096](#)] [[INSPIRE](#)].
- [23] H. Kudoh and T. Wiseman, *Properties of Kaluza-Klein black holes*, *Prog. Theor. Phys.* **111** (2004) 475 [[hep-th/0310104](#)] [[INSPIRE](#)].
- [24] H. Elvang, T. Harmark and N.A. Obers, *Sequences of bubbles and holes: New phases of Kaluza-Klein black holes*, *JHEP* **01** (2005) 003 [[hep-th/0407050](#)] [[INSPIRE](#)].
- [25] H. Kudoh and T. Wiseman, *Connecting black holes and black strings*, *Phys. Rev. Lett.* **94** (2005) 161102 [[hep-th/0409111](#)] [[INSPIRE](#)].
- [26] B. Kleihaus, J. Kunz and E. Radu, *New nonuniform black string solutions*, *JHEP* **06** (2006) 016 [[hep-th/0603119](#)] [[INSPIRE](#)].
- [27] E. Sorkin, *Non-uniform black strings in various dimensions*, *Phys. Rev.* **D 74** (2006) 104027 [[gr-qc/0608115](#)] [[INSPIRE](#)].
- [28] B. Kleihaus and J. Kunz, *Interior of Nonuniform Black Strings*, *Phys. Lett.* **B 664** (2008) 210 [[arXiv:0710.1726](#)] [[INSPIRE](#)].
- [29] P. Figueras, K. Murata and H.S. Reall, *Stable non-uniform black strings below the critical dimension*, *JHEP* **11** (2012) 071 [[arXiv:1209.1981](#)] [[INSPIRE](#)].
- [30] G.T. Horowitz ed., *Black holes in higher dimensions*, Cambridge University Press, Cambridge, U.K. (2012).
- [31] R. Gregory and R. Laflamme, *Hypercylindrical black holes*, *Phys. Rev.* **D 37** (1988) 305 [[INSPIRE](#)].
- [32] S. Bhattacharyya, S. Minwalla and K. Papadodimas, *Small Hairy Black Holes in $AdS_5 \times S^5$* , *JHEP* **11** (2011) 035 [[arXiv:1005.1287](#)] [[INSPIRE](#)].
- [33] O.J.C. Dias, P. Figueras, S. Minwalla, P. Mitra, R. Monteiro and J. E. Santos, *Hairy black holes and solitons in global AdS_5* , *JHEP* **08** (2012) 117 [[arXiv:1112.4447](#)] [[INSPIRE](#)].
- [34] S.A. Gentle, M. Rangamani and B. Withers, *A Soliton Menagerie in AdS* , *JHEP* **05** (2012) 106 [[arXiv:1112.3979](#)] [[INSPIRE](#)].
- [35] R. Monteiro, M.J. Perry and J.E. Santos, *Thermodynamic instability of rotating black holes*, *Phys. Rev.* **D 80** (2009) 024041 [[arXiv:0903.3256](#)] [[INSPIRE](#)].

EXACT EVENT HORIZON OF A BLACK HOLE MERGER

This chapter contains the publication:

- R. Emparan and M. Martinez,
“Exact Event Horizon of a Black Hole Merger,”
Class. Quant. Grav. **33**, no. 15, 155003 (2016), [arXiv:1603.00712](https://arxiv.org/abs/1603.00712) [gr-qc].

Exact event horizon of a black hole merger

Roberto Emparan^{1,2} and Marina Martínez²

¹ Institució Catalana de Recerca i Estudis Avançats (ICREA), Passeig Lluís Companys 23, E-08010 Barcelona, Spain

² Departament de Física Fonamental, Institut de Ciències del Cosmos, Universitat de Barcelona, Martí i Franquès 1, E-08028 Barcelona, Spain

E-mail: emparan@ub.edu

Received 18 March 2016, revised 14 June 2016


Accepted for publication 14 June 2016

Published 29 June 2016



Abstract

We argue that the event horizon of a binary black hole merger, in the extreme-mass-ratio limit where one of the black holes is much smaller than the other, can be described in an exact analytic way. This is done by tracing in the Schwarzschild geometry a congruence of null geodesics that approaches a null plane at infinity. Its form can be given explicitly in terms of elliptic functions, and we use it to analyze and illustrate the time-evolution of the horizon along the merger. We identify features such as the line of caustics at which light rays enter the horizon, and the critical point at which the horizons touch. We also compute several quantities that characterize these aspects of the merger.

 Online supplementary data available from stacks.iop.org/cqg/33/155003/mmedia

Keywords: event horizon, black hole, black hole merger

(Some figures may appear in colour only in the online journal)

1. Introduction

Black hole mergers occur in nature [1]. In the theory of general relativity they are entirely described by the vacuum equations $R_{\mu\nu} = 0$, but extracting the details of the fusion of the two horizons requires in general heavy computational resources. Nevertheless, we will show that there is one instance in which the event horizon of the merger becomes so simple that it can be described in an exact analytic way. This is the extreme-mass-ratio (EMR) limit in which one of the black holes is much smaller than the other. If m and M are the two black hole masses, or equivalently their characteristic sizes (in units $G = c = 1$), then the EMR limit is $m/M \rightarrow 0$.

This limit is often taken as one where the size of the large black hole, M , is fixed while the small black hole is regarded as a point-like object of size $m \rightarrow 0$. Although this viewpoint is appropriate for extracting the gravitational waves emitted in the collision (with wavelengths that grow with M), it erases the details of phenomena that happen on the scale of m , such as the evolution of the event horizon as the two black holes fuse with each other. In order to resolve these smaller length scales, we must take the EMR limit keeping m fixed while³ $M \rightarrow \infty$.

The techniques and ideas that we need for describing this process are elementary. Consider the last moments before the merger, when the small black hole is at a distance $\ll M$ of the large one. The equivalence principle asserts that we can always place ourselves in the rest frame of the small black hole, and that the curvature of the large black hole can be neglected over distances $\ll M$. Then the spacetime around the small black hole should be well approximated by the Schwarzschild geometry [3]. Although the curvature created by the large black hole vanishes in this limit, its horizon is still present: it becomes an infinite, Rindler-type, acceleration horizon. More precisely, it is a congruence of light rays that reach asymptotic null infinity as a planar null surface. We conclude that in the EMR limit, on scales much smaller than M , the event horizon of the black hole merger can be found by tracing an appropriate family of light rays in the Schwarzschild geometry; specifically, a congruence of null geodesics that approach a planar horizon at a large distance from the small black hole.

We will construct this event horizon explicitly, and show that it does indeed exhibit the behavior expected of the merger: at early times, spatial sections of the event horizon consist of two components, one of them an almost spherical small black hole, and the other an almost planar large black hole. The two horizons deform each other through their gravitational attraction (which the large black hole exerts as an acceleration effect, in accord with the equivalence principle) and develop conical shapes along a line of caustics where light rays enter the horizon before the merger. When the black holes merge, they form a single smooth surface that then relaxes down to a planar horizon at late times. We illustrate this with pictures drawn using our exact results. We also compute several parameters that characterize the merger—they are solutions of transcendental equations, so we obtain them numerically.

In our analysis the small black hole plunges head-on into the large one, but it is easy to show that if there is a relative velocity between the two black holes, e.g., the small black hole moves in a direction parallel to the large horizon, the situation is equivalent to our construction up to a rotation.

While we are not aware that this analysis of the horizon of EMR mergers has been done before, related ideas have been employed in recent years. References [4–7] apply the idea that the event horizon for the fall of any gravitating object into an acceleration horizon is obtained by appropriate light-ray-tracing in the spacetime of that object. Reference [8] studies the event horizon of the same EMR merger as we do, but it focuses on scales $\sim M$ and therefore misses the structure of the merger that we observe. A different study of an exact merger, focusing on two equal-mass charged black holes in the Kastor–Traschen solution in deSitter space [9], reaches some conclusions that agree with ours and are presumably generic [10].

Finally, since we have the exact geometry for the merger—i.e., the Schwarzschild metric—it is also possible to study the evolution of its apparent horizon. We leave this for a forthcoming article [11]. A 3D animation of the horizon merger is available at (stacks.iop.org/cqg/33/155003/mmedia).

³ These two views of the EMR limit are the leading-order approximations in a matched asymptotic expansion between the near-zone, with radii $r \ll M$, and the far-zone, with $r \gg m$, which can be matched in the overlap-zone $m \ll r \ll M$ [2]. We return to this issue in the conclusions.

2. Defining the event horizon

As we explained above, the exact geometry for the merger in the limit $m/M \rightarrow 0$ is the Schwarzschild solution with mass m . We seek the event horizon as a particular null hypersurface in this geometry. Conventionally, the Schwarzschild solution has an event horizon at $r = 2m$, which is a cylindrical null hypersurface that reaches \mathcal{I}^+ at infinite retarded time. However, we are interested instead in a different null hypersurface, namely one that reaches \mathcal{I}^+ at a finite retarded time with the geometry of a null plane, like an acceleration horizon would do. This acceleration horizon is the limiting form of the event horizon of the large black hole when $M \rightarrow \infty$.

So we begin with the Schwarzschild black hole, in $D = n + 3$ dimensions

$$ds^2 = -\left(1 - \frac{r_0^n}{r^n}\right)dt^2 + \frac{dr^2}{1 - \frac{r_0^n}{r^n}} + r^2 d\Omega_{(n+1)}^2. \quad (2.1)$$

We use the horizon radius r_0 instead of the mass $m \propto r_0^n$. Although we could set $r_0 = 1$ without loss of generality, we will mostly keep it explicit.

This geometry has a timelike Killing vector ∂_t , which defines the rest frame of the small black hole, and an exact $SO(n+2)$ rotational symmetry. Both isometries are only approximate when the ratio m/M is finite, and would be broken by corrections in an expansion in m/M . But the exact symmetry in the limit $m/M \rightarrow 0$ is crucial for our analysis.

The tangent vector to the light-ray trajectories is

$$P^\mu = \frac{dx^\mu(\lambda)}{d\lambda} = (t, \dot{r}, \dot{\phi}_1, \dots, \dot{\phi}_{n+1}), \quad (2.2)$$

with $P^2 = 0$ and λ an affine parameter along the geodesics. The event horizon of the collision has $SO(n+1)$ symmetry along the axis that joins the two black holes⁴, so we need only consider one angle of S^{n+1} , call it ϕ . Specifically, we write

$$d\Omega_{(n+1)} = d\theta^2 + \sin^2\theta d\phi^2 + \cos^2\theta d\Omega_{(n-1)}, \quad (2.3)$$

and study geodesics on the plane $\theta = \pi/2$. We put the collision axis along the two segments $\phi = 0, \pi$. Before the merger, $\phi = 0$ points away from the large black hole and $\phi = \pi$ points towards it.

The Killing vectors ∂_t and ∂_ϕ of the geometry imply two integrals of motion, and the equations to solve are

$$t = \frac{1}{1 - r_0^n/r^n}, \quad (2.4)$$

$$\dot{\phi} = -\frac{q}{r^2}, \quad (2.5)$$

$$\dot{r} = \frac{1}{r} \sqrt{r^2 - q^2 \left(1 - \frac{r_0^n}{r^n}\right)}, \quad (2.6)$$

where q is the impact parameter, i.e., the ratio between the conserved angular momentum and the energy of the light-ray trajectory.

It will be convenient to use r instead of λ as the (non-affine) parameter along the geodesics. This is because the integration of (2.6) gives $\lambda(r)$ as a combination of elliptic integrals of different kinds, which we cannot invert analytically to find $r(\lambda)$ and then obtain t

⁴ This is also a symmetry of a head-on, radial plunge of two Schwarzschild black holes at finite m/M .

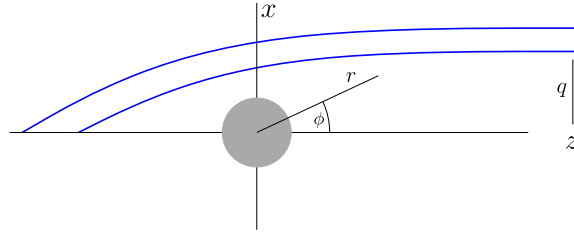


Figure 1. Projection on the spatial plane (x, z) of null generators of the event horizon. The blue curves are the paths traced by light rays that move from left to right towards \mathcal{I}^+ . At late times they move along the z direction as the generators of a Rindler horizon ($dt = dz$). They are labeled by the impact parameter q at future infinity.

(λ) and $\phi(\lambda)$. Instead, we get the geodesics as

$$t_q(r) = \int dr \frac{\dot{t}}{\dot{r}}, \quad \phi_q(r) = \int dr \frac{\dot{\phi}}{\dot{r}}. \quad (2.7)$$

The section of the event horizon in the space (t, ϕ, r) is a two-dimensional surface, i.e., a one-parameter family of geodesics. The entire $(n+2)$ -dimensional event horizon is obtained by rotating through an angle π around the collision axis, and acting with the group $SO(n)$ to generate the $\Omega_{(n-1)}$ factor of the geometry.

The integration constants in (2.7) are fixed by the requirement that the null surface becomes a planar horizon at infinity. The geodesics on this event horizon will be labeled by q . Let us first fix the integration constant for ϕ_q . We have

$$\phi_q(r \rightarrow \infty) = \int dr \frac{\dot{\phi}}{\dot{r}} \Big|_{r \rightarrow \infty} = \alpha_q + \frac{q}{r} + \mathcal{O}(r^{-3}), \quad (2.8)$$

with constant α_q . The latter corresponds to the asymptotic angle of the light-ray trajectories. In order that these rays asymptotically move all in the same direction, we must set α_q to a q -independent value. Without loss of generality, we choose

$$\alpha_q = 0. \quad (2.9)$$

If we define coordinates

$$x = r \sin \phi, \quad z = r \cos \phi, \quad (2.10)$$

then asymptotically all light rays move with $dx = 0$,

$$x|_{r \rightarrow \infty} = q + \mathcal{O}(r^{-(n+2)}), \quad (2.11)$$

$$z|_{r \rightarrow \infty} = r + \mathcal{O}(r^{-1}). \quad (2.12)$$

Figure 1 illustrates the meaning of q as the impact parameter of each geodesic at infinity.

With our choice (2.9) the horizon will satisfy

$$dt - dz = \mathcal{O}(r^{-n}). \quad (2.13)$$

We fix the integration constant for t_q so that all light rays arrive at \mathcal{I}^+ at the same, q -independent, retarded time. Since

$$t_q(r \rightarrow \infty) = r + r_0 \ln(r/r_0) + \beta_q + \mathcal{O}(r^{-1}), \quad (D = 4), \quad (2.14)$$

$$t_q(r \rightarrow \infty) = r + \beta_q + \mathcal{O}(r^{-n}), \quad (D \geq 5), \quad (2.15)$$

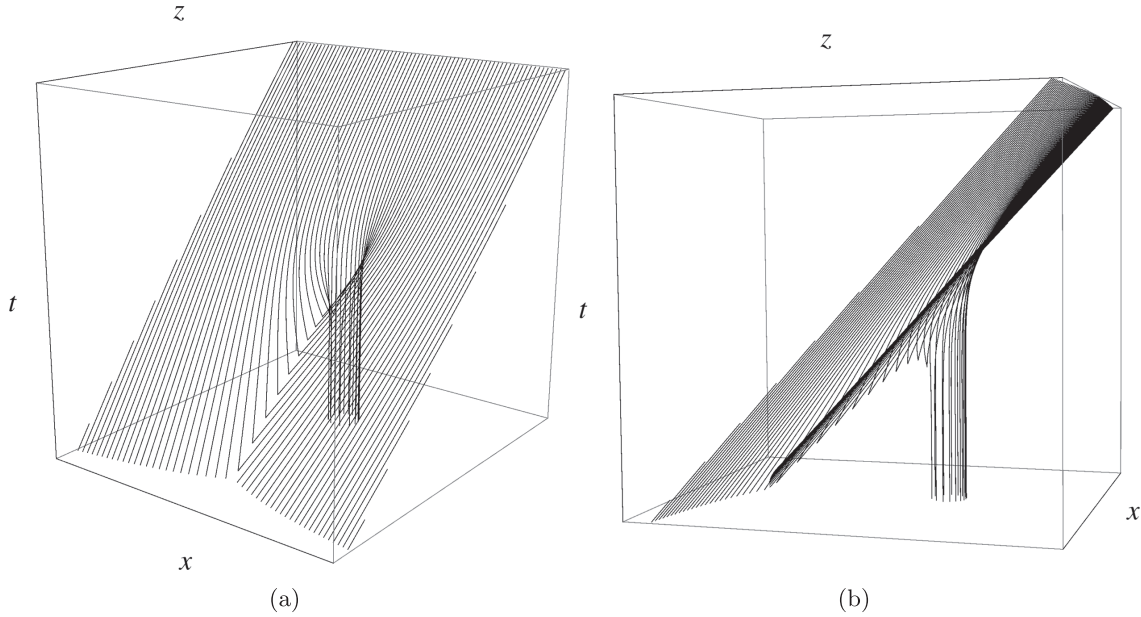


Figure 2. Two views of the event horizon of the four-dimensional merger, in the rest frame of the small black hole. Each curve is a null generator of the hypersurface with a different value of q . The coordinate t is the Killing time. $\sqrt{x^2 + z^2}$ is the area-radius of the Schwarzschild solution.

we must set the integration constant β_q to a q -independent value. For simplicity we choose

$$\beta_q = 0. \tag{2.16}$$

The integrals (2.7) do not take any simple form in general, but for $n = 1, 2$ they can be expressed as combinations of incomplete elliptic integrals. One particular generator can be found easily: the ‘central’ geodesic at $q = 0$, which is

$$t_{q=0}(r) = \begin{cases} r + r_0 \ln \frac{r - r_0}{r_0}, & (n = 1) \\ r + r_0 \ln \sqrt{\frac{r - r_0}{r + r_0}}, & (n = 2) \end{cases} \tag{2.17}$$

$$\phi_{q=0}(r) = 0. \tag{2.18}$$

(the result for arbitrary n can be given in terms of hypergeometric functions). This is a light ray that at $t \rightarrow -\infty$ emerges in the radial direction from the Schwarzschild horizon, to escape towards infinity.

3. Event horizon in $D = 4$

The explicit form of the integrals for $D = 4$,

$$t_q(r) = \int \frac{r^3 dr}{(r - r_0) \sqrt{r(r^3 - q^2 r + q^2 r_0)}}, \tag{3.1}$$

$$\phi_q(r) = - \int \frac{q dr}{\sqrt{r(r^3 - q^2 r + q^2 r_0)}}, \tag{3.2}$$

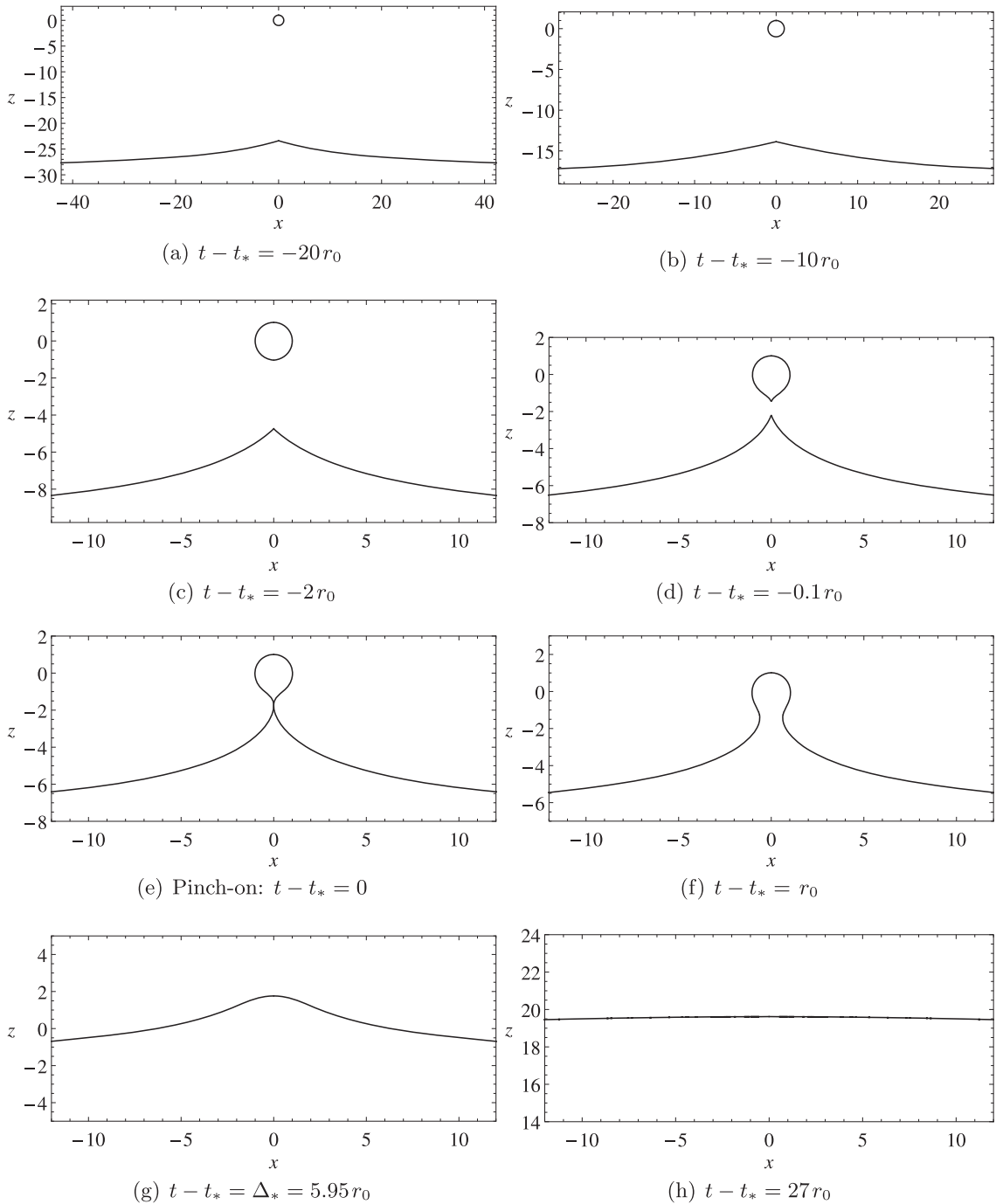


Figure 3. Sequence of constant-time slices of the $D = 4$ event horizon. t is the Killing time of the Schwarzschild geometry, and the spatial coordinates are centered on the small black hole, with area-radius $\sqrt{x^2 + z^2}$. Pinch-on occurs at $t = t_*$ (3.8). The time interval Δ_* is a natural measure of the duration of the fusion (3.9). New null generators enter the two components of the horizon at all $t \in (-\infty, t_*]$, creating cones at the caustic points. The full two-dimensional constant-time slices of the event horizon are obtained by rotating around $x = 0$. Axis units are $r_0 = 1$.

is not very enlightening; we give it in appendix A. The most delicate step is fixing the integration constants to the values (2.9) and (2.16). We have performed first the indefinite integrals using *Mathematica*, which makes specific q -dependent choices for the integration

constants that we must extract and then subtract. The procedure is cumbersome but straightforward. Figure 2 shows the hypersurface generated by these geodesics.

In figure 3 we show a sequence of constant-time slices of this event horizon. They clearly show the evolution expected in this merger: in the past there are two disconnected surfaces: an almost planar one and an almost spherical one. Evolving towards the future they approach each other, and eventually merge into a single horizon, which then relaxes into a flat surface. We do not have explicit analytic expressions for these constant- t slices. These require inverting the function $t_q(r)$ to find $r_q(t)$, which we have not managed to do except in the limit $r \gg r_0$, to be discussed in section 3.2. The plots in figure 3 have been drawn by taking constant- t cuts of plots generated with a sufficiently dense number of geodesics.

We often use the spatial coordinates x and z introduced in (2.10). Although these are not convenient for writing the metric at finite r , they provide an easy way of representing the information in the plane of polar coordinates (r, ϕ) .

3.1. Structure of the event horizon and parameters of the merger

Figure 2 exhibits clearly the presence before the merger of a line of caustics (also known as a crease set), where light rays intersect. At these points, null generators enter to be part of the event horizon. In the full three-dimensional event horizon all the generators that intersect lie on a S^1 of radius q at future infinity⁵. The presence of caustics is generic in the event horizons of black hole mergers. In our hypersurface the caustic line extends to past infinity.

There are two special values of the impact parameter, q_c and q_* , with $q_c < q_*$, which separate the generators into different classes.

3.1.1. Non-caustic generators. The light rays at $q = q_c$ separate the generators with $q > q_c$ that enter the horizon at a caustic at finite time, from those with $q < q_c$ that extend back to infinitely early times (see figure 4). The latter asymptote in the past to the generators of the Schwarzschild horizon at $r = r_0$. In particular, the critical value $q = q_c$ corresponds to the rays that start at $r = r_0$ at $\phi = \pi$, and therefore are determined by the equation

$$\phi_{q_c}(r_0) = \pi. \quad (3.3)$$

We can solve this numerically to obtain⁶

$$q_c = 2.228\,64\,r_0. \quad (3.4)$$

The generators with $q \leq q_c$ form at future infinity a disk of radius q_c and area πq_c^2 . Their initial area at past infinity is the area of the Schwarzschild black hole, $\mathcal{A}_{\text{in}} = 4\pi r_0^2$. Thus in the evolution of this part of the event horizon, to which no new generators are added, the area increases by

$$\Delta \mathcal{A}_{\text{non-caustic}} = \left(\left(\frac{q_c}{2r_0} \right)^2 - 1 \right) 4\pi r_0^2 = 0.24171 \mathcal{A}_{\text{in}}. \quad (3.5)$$

3.1.2. Caustic generators. All generators with $q_c < q < \infty$ enter the horizon at a caustic at finite time. Among them, we single out those with $q = q_*$ which are the last to enter the horizon as measured in Killing time t . Generators with $q > q_*$ enter the horizon on the side of

⁵ It may be more appropriate to refer to the intersection as a focus rather than a caustic, but the latter terminology is rather common.

⁶ This and subsequent numerical solutions of transcendental equations are obtained using *Mathematica*'s `FindRoot`, which gives better precision than we are showing.

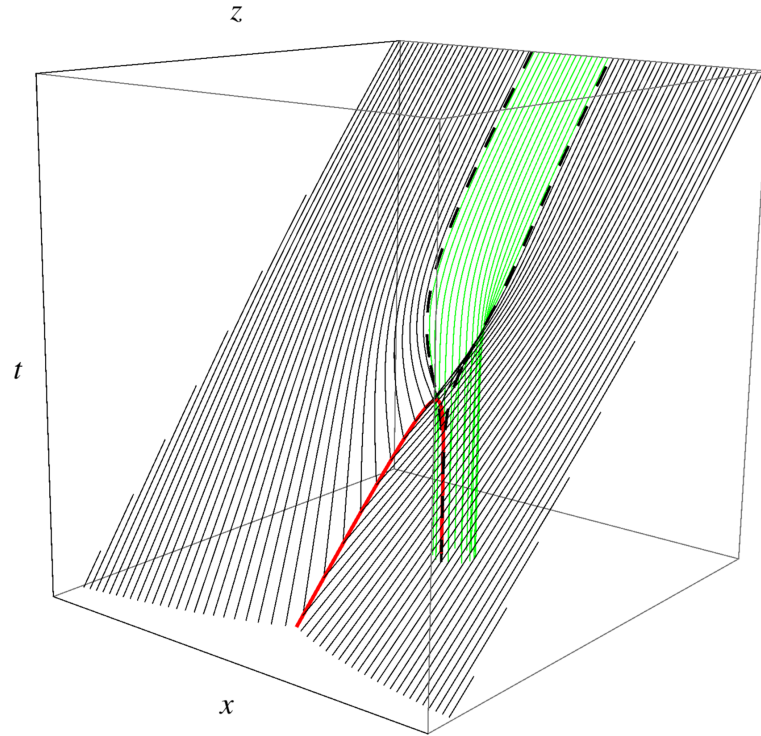


Figure 4. Event horizon of the merger in four-dimensions. Non-caustic geodesics are the green curves, which emanate from the Schwarzschild horizon in the infinite past. Caustic geodesics are shown in black. They enter the hypersurface through the caustic line (red thick curve). The black dashed curves are the geodesics with $q = q_c$ that separate the two classes.

the large black hole, and generators with $q_c < q < q_*$ enter on the side of the small black hole. This is illustrated in figure 5.

The rays with $q = q_*$ enter at time $t = t_*$ and radius $r = r_*$. These are the parameters that characterize the pinch-on instant at which the two horizons touch and merge to form a single one. In order to determine these parameters, follow the rays with $q = q_*$ back in time from \mathcal{I}^+ . At the caustic on the collision axis $\phi = \pi$, where they leave the horizon towards the past, they neither approach the small black hole nor escape from it, that is, $\dot{r}|_{\phi=\pi} = 0$. Then (2.6) implies that q_* and r_* are obtained by solving the equations

$$r_*^3 - q_*^2 r_* + q_*^2 r_0 = 0, \quad \phi_{q_*}(r_*) = \pi, \quad (3.6)$$

where r_* is the largest root of the cubic polynomial⁷. We find

$$q_* = 2.678\,48\,r_0, \quad r_* = 1.760\,31\,r_0. \quad (3.7)$$

r_* can be taken as a measure of how strongly the small black hole is distorted, or pulled at the cusp, from the initial sphere of radius r_0 .

Inserting these values in the solution for $t_q(r)$ we obtain

$$t_* = -4.460\,48\,r_0. \quad (3.8)$$

Note that t_* is determined only with reference to the choice (2.16) that fixes the origin of retarded time. We may also consider the difference Δ_* between the retarded time at \mathcal{I}^+ of the

⁷ For $q < q_{\text{ph}} = (3\sqrt{3}/2)r_0$ there are no real positive roots. q_{ph} corresponds to the unstable circular photon orbit at $r_{\text{ph}} = 3r_0/2$, which does not appear to play any special role in this construction.

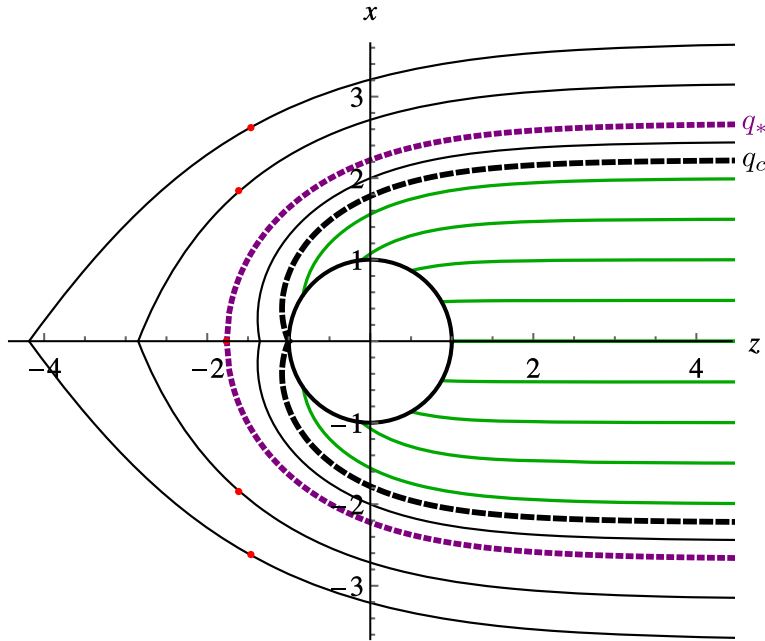


Figure 5. Projection of the hypersurface in the (x, z) plane. All rays propagate towards $z \rightarrow +\infty$. Green curves are non-caustic generators. The black dashed curves with $q = q_c$ separate them from caustic generators. The dotted purple curves with $q = q_*$ separate the generators that enter the horizon on the side of the small black hole, $q_c < q < q_*$ from those that enter on the side of the large black hole, $q > q_*$. The latter rays first approach the small black hole, reach a minimum distance r_{\min} (red dots), and then move away from it. For $q = q_*$, the minimum r_{\min} lies at the caustic. Rays with $q_c < q < q_*$ move away from the small black hole at all times after they enter the event horizon.

event horizon (in the direction $\phi = 0$), and the retarded time of the light ray emitted at the pinch-on instant in the opposite direction $\phi = \pi$ —i.e., towards the large black hole. This is

$$\Delta_* = r_* + r_0 \ln((r_* - r_0)/r_0) - t_* = 5.946\,76\,r_0. \tag{3.9}$$

Figure 6 illustrates it in a conformal diagram for the causal structure of the merger geometry (i.e., the Schwarzschild spacetime) along the collision axis.

Note that the dashed-red light ray propagates inside the large black hole, so the retarded-time difference Δ_* is not measurable by observers outside it. Δ_* also admits an interpretation that does not involve any propagation through the large black hole interior: it is the time elapsed from t_* until the moment when the central generator (2.17) reaches $r = r_*$ along the antipodal direction $\phi = 0$, i.e., until the instant at which the green ray intersects the line $r = r_*$ in figure 6. By this time, the two horizons have noticeably fused with each other (see figure 3). Through either interpretation, Δ_* can be regarded as characterizing the duration of the merger.

We can also quantify the growth in the area of the small black hole, now taking into account the addition of generators to the small horizon at caustics. This is

$$\Delta \mathcal{A}_{\text{smallbh}} = \left(\left(\frac{q_*}{2r_0} \right)^2 - 1 \right) 4\pi r_0^2 = 0.793\,56\, \mathcal{A}_{\text{in}}. \tag{3.10}$$

The difference between (3.10) and (3.5) is attributed to the generators with $q_c < q < q_*$ that are added, and to their subsequent expansion until they reach \mathcal{I}^+ .

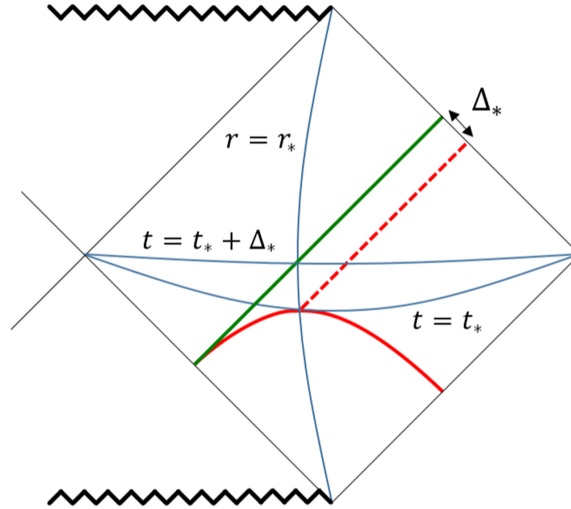


Figure 6. Conformal diagram for the geometry along the collision axis $\phi = 0, \pi$. The green light ray is the central event horizon generator (2.17) with $q = 0$, which moves along $\phi = 0$. The solid-red spacelike curve is the line of caustics, which extends along $\phi = \pi$. The dashed-red line is a light ray that emerges from the pinch-on point at $r = r_*, t = t_*$, towards \mathcal{I}^+ on $\phi = \pi$. This ray propagates inside the large black hole. The retarded-time difference Δ_* characterizes the duration of the merger.

It is unclear to us whether there is any useful way to quantify the total growth of the large horizon in the merger, since it is an infinite horizon where all the generators with $q_c < q < \infty$ have entered at caustics at a finite time in the past. That is, the number of generators entering the large horizon is infinite. This is a consequence of taking the EMR limit when the large black hole is infinite in size. Indeed, if we estimate the increment in the area neglecting the emission of radiation (see section 7), it is expected to be

$$\Delta\mathcal{A} \simeq 16\pi(M + m)^2 - 16\pi M^2 - 16\pi m^2 = 32\pi Mm, \tag{3.11}$$

which diverges in the limit $M/m \rightarrow \infty$ if we keep fixed the small black hole mass m .

We can obtain the equation for the caustics in explicit form. In order to find the radial position $r_{\text{caustic}}(q)$ we have to solve

$$\phi_q(r_{\text{caustic}}) = \pi \tag{3.12}$$

for a given $q > q_c$. Using the expressions in appendix A we obtain

$$r_{\text{caustic}}(q) = \frac{r_2 + r_3}{b^{-1} \text{sn}\left(\frac{\pi\sqrt{r_2(r_2+r_3)}}{2|q|} + F\left(\sin^{-1}\sqrt{b}, \frac{r_3 a}{r_2}\right), \frac{r_3 a}{r_2}\right)^2 - 1}, \tag{3.13}$$

where sn is a Jacobi elliptic function, r_2 and r_3 are two of the roots of the polynomial $r^3 - q^2 r + q^2 r_0$ (their explicit form is given in appendix A), and a and b are combinations of them,

$$a = \frac{2r_2 + r_3}{r_2 + 2r_3}, \tag{3.14}$$

$$b = \frac{r_2}{2r_2 + r_3}. \tag{3.15}$$

Equation (3.13) is valid for both $q_c < q < q_*$ and $q > q_*$.

The rays $q_c < q < q_*$ that enter at the small horizon at radius $r = r_{\text{caustic}}$, afterwards move away from the small black hole in trajectories with $\dot{r} > 0$. In contrast, the generators with $q > q_*$ that enter at the large horizon, first approach the small black hole, then reach a minimum distance of it, $r = r_{\text{min}}$, and afterwards escape away towards infinity. This minimum radius is the largest root of $r^3 - q^2r + q^2r_0$ that is also smaller than r_{caustic} , and we show it for some geodesics in figure 4.

These considerations imply that we must be careful when computing the generators with $q > q_*$. Since we are parametrizing the geodesics using r , their trajectories must be given as two branches of solutions

$$t = \begin{cases} -t_q(r) + 2t_q(r_{\text{min}}), & r \in [r_{\text{min}}, r_{\text{caustic}}], \\ t_q(r), & r \in [r_{\text{min}}, \infty), \end{cases} \quad (3.16)$$

$$\phi = \begin{cases} -\phi_q(r) + 2\phi_q(r_{\text{min}}), & r \in [r_{\text{min}}, r_{\text{caustic}}], \\ \phi_q(r), & r \in [r_{\text{min}}, \infty), \end{cases} \quad (3.17)$$

where $t_q(r)$ and $\phi_q(r)$ are the same functions we use for the other geodesics.

3.2. Perturbative solution at $r \gg r_0$

The integrals (3.1) and (3.2) simplify considerably if we evaluate them in an expansion in $r_0/r \ll 1$. In this limit the small black hole appears as a point particle, so we miss the structure of the event horizon around the region $r \sim r_0$ where the merger takes place. On the other hand, this limit allows us to find much more easily the geometry of the horizon at large distances of the small black hole.

In fact, we can obtain explicit analytic expressions for constant-time sections of the event horizon, which we could not do in the exact solution. For this purpose it is convenient to give the event horizon as a surface parametrized by t and q . To first order in r_0 , and after fixing the integration constant (2.16) we can invert $t_q(r)$ to find

$$r(q, t) = \sqrt{q^2 + t^2} + \frac{r_0}{2\sqrt{q^2 + t^2}} \left(t - \sqrt{q^2 + t^2} - 2t \ln \frac{t + \sqrt{q^2 + t^2}}{2r_0} \right) + \mathcal{O}(r_0^2). \quad (3.18)$$

With this, and after integrating $\phi_q(r)$ imposing (2.9), we obtain the event horizon in the spatial coordinates of (2.10),

$$\begin{aligned} x(q, t) &= q - r_0 \frac{(t - \sqrt{q^2 + t^2})^2}{2q\sqrt{q^2 + t^2}} + \mathcal{O}(r_0^2), \\ z(q, t) &= t - \frac{r_0}{2} \left(1 - \frac{t}{\sqrt{q^2 + t^2}} + 2 \ln \frac{t + \sqrt{q^2 + t^2}}{2r_0} \right) + \mathcal{O}(r_0^2). \end{aligned} \quad (3.19)$$

This is valid both for $z, t > 0$ and $z, t < 0$. In appendix B we extend it to the next order.

The only assumption in obtaining this result is that $r \gg r_0$. This includes several regions of interest:

3.2.1. Late times $t, z \gg r_0$, for all x and q . When $t \sim z \sim x$ (possibly $x \ll t, z$) the horizon takes an asymptotically planar form with logarithmic corrections

$$z = t - r_0 \left(\ln \frac{t + \sqrt{x^2 + t^2}}{2r_0} + \mathcal{O}(1) \right) + \mathcal{O}(r_0^2). \quad (3.20)$$

3.2.2. Moment of merger $t, z \sim r_0$, at large distance from the merger region, $|x| \gg r_0$. Here the event horizon is the surface

$$z \simeq t - r_0 \ln \frac{|x|}{2r_0} + \mathcal{O}(r_0^2/x), \quad (3.21)$$

and the spatial sections do not become flat (i.e., $z \simeq t$) at large $|x|$, but have $z \sim -\ln |x|$ instead. In fact the same phenomenon happens for $t, z \gg r_0$ if we consider exponentially large $|x| \sim r_0 e^{t/r_0}$.

This distortion from the planar shape is an effect of the long range of the gravitational field of the small black hole in four-dimensions. In a merger of black holes with small but finite mass ratio m/M , the radius of the large black hole acts as a long-distance cut-off on the coordinate x along the horizon. The results above mean that around the moment when the small black hole falls into the large one, it creates a big distortion $\sim m \ln(M/m)$ at distances $\gg m$ on the horizon of the latter, which does not dissipate until late times $t \gg m \ln(M/m)$.

3.2.3. Early times $-t, -z \gg r_0$, including the caustic line. Here equations (3.19) apply at all x and in particular around the caustic line on the large horizon at $x = 0$. Then we can study the properties of the caustic cones at early times. Assuming that the generators that reach the axis $\phi = \pi$ at this time have $q \ll |t|$ we can expand

$$x(q, t) \simeq q - \frac{2r_0|t|}{q}, \quad (3.22)$$

$$z(q, t) \simeq t - r_0 \left(\ln \left(\frac{q^2}{4|t|r_0} \right) + 1 \right) + \frac{2r_0^2|t|}{q^2}, \quad (3.23)$$

so near the axis $x = 0$ we find, consistently, $q \simeq \sqrt{2r_0|t|} \ll |t|$. Note that in $z(q, t)$ we have included a term of order r_0^2 , since near the caustic line at $|t| \gg r_0$ it contributes at the same order as the others (corrections to $z(q, t)$ at order r_0^3 or higher are suppressed near the caustic). Then, the caustic cone at the axis has slope

$$\left. \frac{dz}{dx} \right|_{\text{cone}} = \left. \frac{\partial_q z}{\partial_q x} \right|_{\text{cone}} \simeq -\sqrt{\frac{2r_0}{|t|}}. \quad (3.24)$$

This result is in precise agreement with the value that [8] calculated keeping the large black hole size fixed and expanding in the small black hole size⁸ r_0 .

The caustic line at early times is the spacelike curve $-t = r + \mathcal{O}(r_0)$. Its line element is

$$ds_c \simeq \sqrt{\frac{r_0}{r}} dr \quad (3.25)$$

so its total length $L_c = \int ds_c$ diverges in the past at $r \rightarrow \infty$. If the line is cut off by the size $\sim M$ of the large black hole, then its length is

⁸ Reference [8] in equation (120) gives the cone angle α as a function of the (large black hole) retarded time v and the small black hole mass μ . The result at $v \rightarrow 0$ agrees with ours at large $-t$, once we identify $2\alpha \simeq dz/dx|_{\text{cone}}$, $v \simeq -t$ and $\mu = r_0/2$.

$$L_c \sim \sqrt{mM}, \quad (3.26)$$

which is in parametric agreement with the calculation in [8].

The perturbative solution at order r_0^2 (appendix B) reproduces very well the exact shape of the event horizon outside of a region of size $\approx \Delta_*$ around the merger where the evolution is very nonlinear. Figure 7 exhibits this agreement.

It may be interesting to study the properties of the caustic line along the small black hole horizon. However, this requires a different approach and we have not pursued it.

4. Event horizon in $D = 5$

The five-dimensional version of (2.7),

$$t_q(r) = \int \frac{r^4 dr}{(r^2 - r_0^2) \sqrt{r^4 - q^2 r^2 + q^2 r_0^2}}, \quad (4.1)$$

$$\phi_q(r) = - \int \frac{q dr}{\sqrt{r^4 - q^2 r^2 + q^2 r_0^2}}, \quad (4.2)$$

is not more complicated than the four-dimensional case. Once again the solution is expressed in terms of elliptic integrals of different kinds, which we give in appendix A.

We show the $D = 5$ hypersurface in figure 8. It is very similar to the four-dimensional one, but now the event horizon at late time approaches a planar horizon more quickly, as we will see below.

Again, we have the same three types of null geodesics on the event horizon, and the values of q that delimit them are

$$q_c = 1.886\,98\,r_0, \quad q_* = 2.009\,00\,r_0. \quad (4.3)$$

The pinch-on radius and times are

$$r_* = 1.486\,22\,r_0, \quad (4.4)$$

$$t_* = -3.984\,44\,r_0, \quad (4.5)$$

$$\Delta_* = 4.654\,73\,r_0. \quad (4.6)$$

All these parameters are smaller than in four-dimensions, which reflects the fact that as D grows larger the gravitational potential is concentrated closer to the small black hole, and the merger proceeds more swiftly.

The area increments of the small black hole part of the horizon are

$$\Delta \mathcal{A}_{\text{non-caustic}} = \left(\frac{2}{3\pi} \left(\frac{q_c}{r_0} \right)^3 - 1 \right) 2\pi^2 r_0^3 = 0.425\,807\, \mathcal{A}_{\text{in}}, \quad (4.7)$$

$$\Delta \mathcal{A}_{\text{smallbh}} = \left(\frac{2}{3\pi} \left(\frac{q_*}{r_0} \right)^3 - 1 \right) 2\pi^2 r_0^3 = 0.720\,674\, \mathcal{A}_{\text{in}}. \quad (4.8)$$

The fact that (4.7) is larger than in four-dimensions is due to the larger number of directions in which the generators can expand. In contrast, the total increase in the area of the small black hole (4.8) is less than in four-dimensions, indicating that fewer generators are added to the horizon through the milder caustic. This conforms to the general idea that black hole mergers are less irreversible (produce less entropy) as the number of dimensions grows larger.

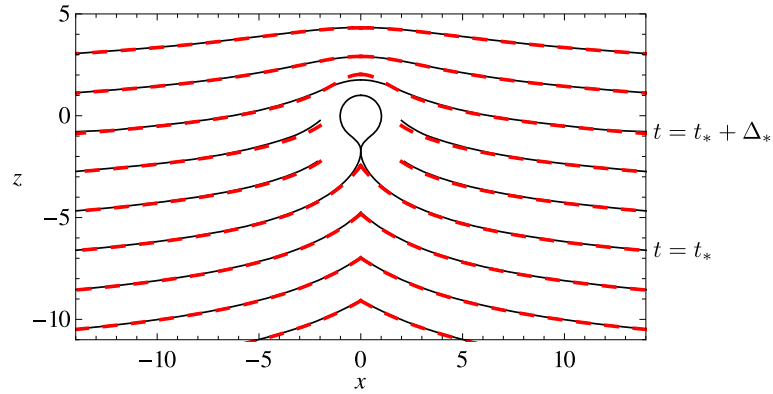


Figure 7. Constant-time slices of the four-dimensional event horizon, computed exactly (solid black), and approximately to order r_0^2 (dashed red). From top to bottom, these are $t - t_* = 10, 8, \Delta_*, 4, 2, 0, -2, -4, -6$. The region excluded, where the discrepancies are larger, has diameter $\lesssim \Delta_*$ around $x = z = 0$.

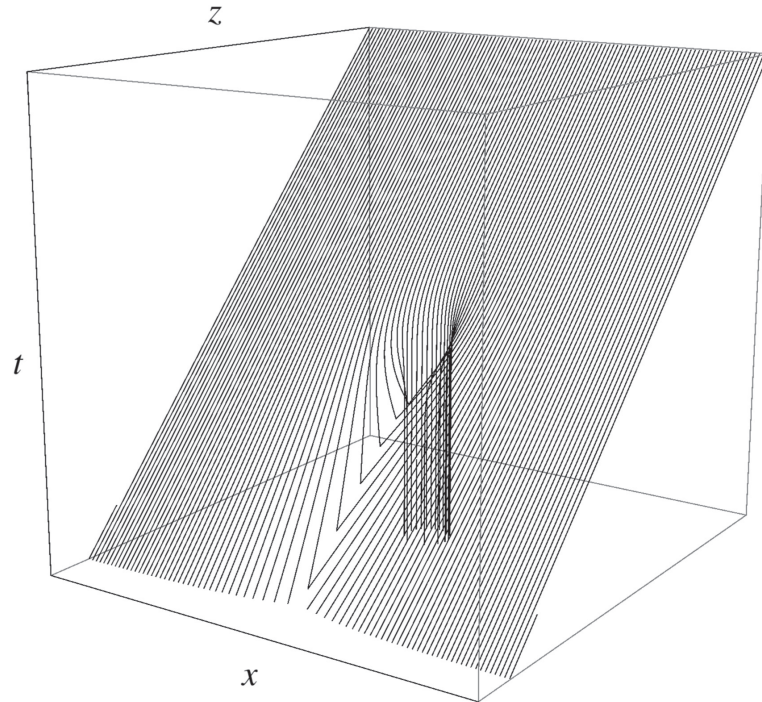


Figure 8. Event horizon of the merger in five-dimensions. Each curve is a null generator of the hypersurface.

4.1. Perturbative solution

Performing the integrals for small r_0 we now find

$$x(q, t) = q + r_0^2 \left(-\frac{2q^2 + 3t^2}{4q(t^2 + q^2)} + \frac{3t}{4q^2} \arctan \frac{q}{t} \right) + \mathcal{O}(r_0^4), \quad (4.9)$$

$$z(q, t) = t + r_0^2 \left(\frac{t}{4(t^2 + q^2)} + \frac{3}{4q} \arctan \frac{q}{t} \right) + \mathcal{O}(r_0^4), \tag{4.10}$$

when $t > 0$. The analytic continuation to $t < 0$ is obtained by substituting

$$\arctan \frac{q}{t} \rightarrow \pi - \arctan \frac{q}{|t|}. \tag{4.11}$$

At late times the horizon becomes planar, $z = t + \mathcal{O}(r_0^2/t)$, even at very large values of x . It is also planar at large distances around the merger time, $|x| \gg r_0 \sim t, z$, where $z = t + \mathcal{O}(r_0^2/x)$.

The generators that enter at the caustic at the axis $x = 0$ at an early time $-t \gg r_0$ have $q^3 \simeq 3\pi r_0^2 |t|/4$. There the horizon develops a cone with slope

$$\left. \frac{dz}{dx} \right|_{\text{cone}} \sim - \left(\frac{r_0}{|t|} \right)^{2/3} \tag{4.12}$$

(to obtain the precise factor we would need the corrections at r_0^4 in $z(q, t)$). The length of the caustic line $-t = r + \mathcal{O}(r_0^2)$ is again infinite, but now its dependence on the large black hole size is only logarithmic

$$L_c \sim \sqrt{m} \ln \frac{M}{m}. \tag{4.13}$$

These results generalize to arbitrary dimension, where the rays at the caustic have $q^{n+1} \propto r_0^n |t|$ and

$$\left. \frac{dz}{dx} \right|_{\text{cone}} \sim - \frac{q}{|t|} \sim - \left(\frac{r_0}{|t|} \right)^{n/(n+1)}, \tag{4.14}$$

so the cone is less pointed for larger n . The line element along the caustic line, $ds_c \simeq (r_0/r)^{n/2} dr$ is such that when $n > 2$ the total length is finite, even if the line extends to the infinite past. This is because the caustic line approaches much more quickly a null curve, which does not add to the total proper length.

Again, we interpret these results as consequences of the stronger localization of the gravitational field as n increases, which yields a very mild caustic singularity on the horizon at $r \gg r_0$.

5. Throat swelling

Black hole fusion begins at the moment when the cones on the event horizon close off, develop into cusps at $t = t_*$, and then form a thin throat that connects the two horizons. We can expect that the geometry of the event horizon exhibits critical behavior in the instants before and after pinch-on. Since in this regime we do not have explicit solutions for the constant-time sections of the event horizon, we study it through slices such as those used to produce the plots in figure 3.

Right before the merger, when the caustic cone on the large horizon closes off as $t \rightarrow t_*$, we expect that

$$\left. \frac{dz}{dx} \right|_{\text{cone}} \sim -(t_* - t)^{-\gamma}. \tag{5.1}$$

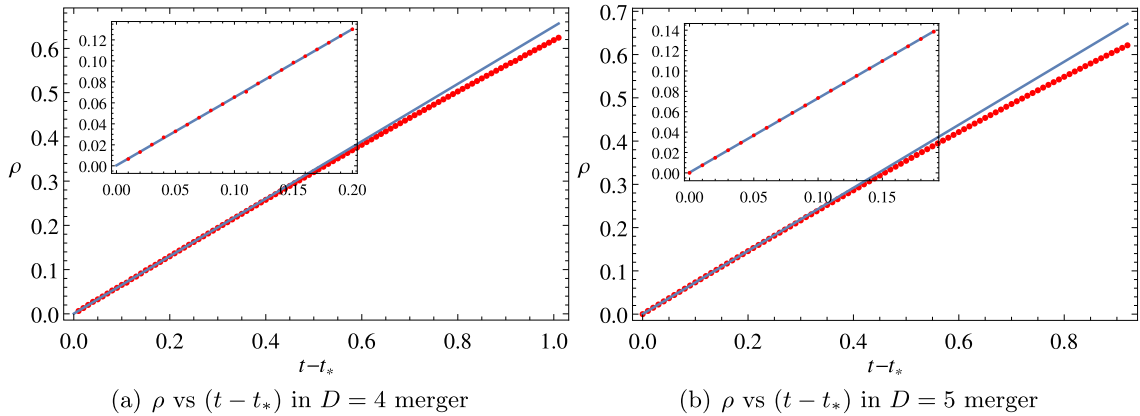


Figure 9. Plots of the throat thickness versus time, in units $r_0 = 1$. The blue curve is a linear fit to the first 20 points with $t - t_* \in (0.01, 0.2)$. The inset is a magnification close to the pinch-on, where the throat grows linearly with t .

We find $\gamma = 1/2$ up to a few percent, both in $D = 4$ and $D = 5$. This suggests that it may be the same in other dimensions. It may be interesting to verify this, and also to investigate whether this exponent is universal, e.g., when charge or rotation are introduced. Being a short-distance effect, the same critical behavior could be present in the small black hole horizon, but this remains to be studied.

We can also examine the growth of the thin throat connecting the two horizons immediately after its formation at pinch-on time t_* . We have managed to accurately measure the half-width ρ of the throat, i.e., its extent along the semi-axis $x > 0$. We find that, for times shortly after t_* , the throat grows linearly

$$\rho = \begin{cases} (0.650 \pm 0.005)(t - t_*), & (D = 4) \\ (0.730 \pm 0.005)(t - t_*), & (D = 5) \end{cases} \quad (5.2)$$

(see figure 9). This linear growth lasts until $\rho/r_0 \simeq 0.25$, and then begins to slow down.

The linear behavior (5.2) agrees with the results in [10], which studied a merger in the Kastor–Traschen solution of four-dimensional charged black holes in deSitter [9]. As [10] observed, the linear growth may be expected since after the merger the surface is smooth. So we expect this to be a general feature of black hole mergers.

In the example in [10] the behavior (5.2) was followed after a time by exponential growth, presumably due to the deSitter expansion. Instead, in our setup the growth slows down.

6. Mergers with relative velocities

We have described a merger in which an infinitely large black hole approaches along the z direction a finite-size black hole that is at rest. The asymptotic surface $dt = dz$ from which the event horizon is traced back is invariant under boosts in z , so the event horizon would be the same if there were any velocity along the collision axis.

We may also consider situations where the black holes have a relative velocity along a direction parallel to the large horizon—this includes in particular the possibility of a large rotating black hole and a small black hole on a trajectory not co-rotating with it. The generic arguments in the introduction indicate that in the EMR limit this event horizon should be equivalent to the one for radial plunge, but it may be worth elaborating the case.

Let us focus on the form of the event horizon in the asymptotic future, where we impose the initial (actually final) conditions that determine the null congruence. We have been considering that this horizon does not move, relative to the small black hole, along its planar directions, so asymptotically the surface is given by

$$dt = dz. \quad (6.1)$$

If instead the large horizon moves along the x direction, we can obtain its asymptotic form by a boost

$$t = \bar{t} \cosh \eta - \bar{x} \sinh \eta, \quad (6.2)$$

$$x = \bar{x} \cosh \eta - \bar{t} \sinh \eta, \quad (6.3)$$

and $z = \bar{z}$. That is, if now \bar{t} is the time in the rest frame of the small black hole, the event horizon is a null congruence in the Schwarzschild geometry that asymptotes to

$$d\bar{t} = \frac{d\bar{z}}{\cosh \eta} + \tanh \eta d\bar{x}. \quad (6.4)$$

However, this surface can also be obtained from (6.1) by performing a rotation in the (x, z) plane

$$z = \bar{z} \cos \alpha + \bar{x} \sin \alpha, \quad (6.5)$$

$$x = \bar{x} \cos \alpha - \bar{z} \sin \alpha, \quad (6.6)$$

and $t = \bar{t}$, so that

$$d\bar{t} = \cos \alpha d\bar{z} + \sin \alpha d\bar{x}. \quad (6.7)$$

We just need to choose the rotation angle to be

$$\sin \alpha = \tanh \eta. \quad (6.8)$$

Thus the effect of a boost in a direction parallel to the large horizon is equivalent to a rotation in the plane formed by this direction and the collision axis. We do not need to compute again the null generators, since it suffices to set the q -independent integration constant α in (2.9) to the value (6.8).

7. Concluding remarks

Everything we have needed to obtain the event horizon has been in place for a long time: the technical ingredients are the Schwarzschild solution and its null geodesics, known 100 years ago. The concepts involved are also venerably old—the equivalence principle, which predates general relativity itself, and the notion of event horizon, well understood more than 50 years ago.

The construction can be extended to EMR mergers with small black holes other than Schwarzschild. When the small black hole is asymptotically flat and spherically symmetric, like the Reissner–Nordstrom solution, the extension is straightforward, up to the explicit quadratures for $t_q(r)$ and $\phi_q(r)$. Of more direct physical interest is the EMR merger with a small Kerr black hole. The lower degree of symmetry makes the problem computationally quite harder, but still much simpler than when m/M is finite, since we know the exact geometry in which the event horizon must be found. The class of large black holes that can be covered is also very wide, since the geometry near a non-degenerate horizon is always Rindler space.

Gravitational wave emission is conspicuously absent from our description of the merger. In the limit $M \rightarrow \infty$ the radiation zone is pushed infinitely far away, and the geometry acquires an exact time-translation isometry, so there cannot be any waves. Relatedly, the quasinormal oscillations of the large black hole are not visible in our analysis. The lowest quasinormal modes have wavelengths $\sim M$, so they disappear from sight in the limit, while the higher modes of wavelength $\sim m$ have large partial wave numbers $\ell \sim M/m$ and are localized near the circular photon orbit of the large black hole, i.e., at a large distance, $\sim M$, from the near-zone that we focus on.

Thus the price to pay for capturing exactly the event horizon is that the main observational signature of a black hole merger is removed from the picture. What is, then, the utility of this analysis?

First of all, and leaving aside the difficulties (even of principle) of directly observing the structure of the event horizon at very short scales, we believe that it is useful to have as simple an understanding as possible of a basic phenomenon in general relativity—which furthermore can be a good approximation to events that possibly take place in nature: given the findings of [1], it does not seem impossible that black hole binary mergers with mass ratios $\lesssim 1/30$ could be detected in ground-based observatories, even more so in space-based ones. Our construction and characterization of the event horizon can be used as a benchmark for detailed numerical calculations that attempt to capture all the features of the phenomenon down to scales $\sim m$.

Second, our study gives the near-zone solution of the merger to leading order in m/M . One can then match it to the far-zone construction of the EMR event horizon in [8], to obtain the first-order corrections in m/M . This will make the curvature of the large black hole visible in the near-zone, as well as the effects of gravitational waves on it. Corrections computed in the near-zone then provide the boundary conditions for the next-order calculation in the far zone, and so on, iteratively in a matched asymptotic expansion. It is not inconceivable that the sensitivity of future detectors will require such higher-order calculations. Our work is only the first step in the description of their event horizons.

Acknowledgments

We are grateful to Vitor Cardoso for bringing [8] to our attention. This work has been partially supported by FPA2013-46570-C2-2-P, AGAUR 2009-SGR-168 and CPAN CSD2007-00042 Consolider-Ingenio 2010. MM is supported by an FI Fellowship of AGAUR, Generalitat de Catalunya, 2013FI B 00840.

Appendix A. Explicit solution

A.1. $D = 4$

In order to solve the integrals we begin by writing them as

$$t_q(r) = \int \frac{r^3 dr}{(r - r_0) \sqrt{r(r - r_1)(r - r_2)(r - r_3)}}, \quad (\text{A.1})$$

$$\phi_q(r) = - \int \frac{q dr}{\sqrt{r(r - r_1)(r - r_2)(r - r_3)}}, \quad (\text{A.2})$$

where r_1 , r_2 and r_3 are the roots of the polynomial $r^3 - q^2r + q^2r_0$. For $|q/r_0| < 3\sqrt{3}/2$ one of the roots is real (r_1) and the other two (r_2 and r_3) are complex conjugates:

$$r_1 = \frac{-1}{\sqrt[3]{18}}(f_1^{1/3} + f_2^{1/3}), \quad (\text{A.3})$$

$$r_2 = \frac{1}{\sqrt[3]{144}}[(f_1^{1/3} + f_2^{1/3}) + i\sqrt{3}(f_1^{1/3} - f_2^{1/3})], \quad (\text{A.4})$$

$$r_3 = \frac{1}{\sqrt[3]{144}}[(f_1^{1/3} + f_2^{1/3}) - i\sqrt{3}(f_1^{1/3} - f_2^{1/3})]. \quad (\text{A.5})$$

Here

$$f_1 = 9q^2r_0 - q^2\sqrt{81r_0^2 - 12q^2}, \quad (\text{A.6})$$

$$f_2 = 9q^2r_0 + q^2\sqrt{81r_0^2 - 12q^2}, \quad (\text{A.7})$$

are positive and real for $|q/r_0| < 3\sqrt{3}/2$. When $|q/r_0| > 3\sqrt{3}/2$ the polynomial has three different real roots, and it is simpler to write them as

$$r_1 = -\frac{|q|}{\sqrt{3}} \left[\cos \left(\frac{1}{3} \cos^{-1} \left(\frac{-3\sqrt{3}r_0}{2|q|} \right) \right) + \sqrt{3} \sin \left(\frac{1}{3} \cos^{-1} \left(\frac{-3\sqrt{3}r_0}{2|q|} \right) \right) \right], \quad (\text{A.8})$$

$$r_2 = \frac{2|q|}{\sqrt{3}} \left[\cos \left(\frac{1}{3} \cos^{-1} \left(\frac{-3\sqrt{3}r_0}{2|q|} \right) \right) \right], \quad (\text{A.9})$$

$$r_3 = \frac{|q|}{\sqrt{3}} \left[-\cos \left(\frac{1}{3} \cos^{-1} \left(\frac{-3\sqrt{3}r_0}{2|q|} \right) \right) + \sqrt{3} \sin \left(\frac{1}{3} \cos^{-1} \left(\frac{-3\sqrt{3}r_0}{2|q|} \right) \right) \right]. \quad (\text{A.10})$$

Since they are roots of a cubic with no quadratic term they satisfy

$$r_1 + r_2 + r_3 = 0, \quad (\text{A.11})$$

which we use to eliminate r_1 in favor of r_2 and r_3 .

The results can be expressed in terms of incomplete elliptic integrals of the first, second and third kind

$$F(x|m) = \int_0^x \frac{d\theta}{\sqrt{1 - m \sin^2 \theta}}, \quad (\text{A.12})$$

$$E(x|m) = \int_0^x \sqrt{1 - m \sin^2 \theta} d\theta, \quad (\text{A.13})$$

$$\Pi(n; x|m) = \int_0^x \frac{d\theta}{(1 - n \sin^2 \theta) \sqrt{1 - m \sin^2 \theta}}. \quad (\text{A.14})$$

When evaluating these expressions care must be exercised with the prescription for the square root of complex numbers and with the branch cuts in the elliptic functions. Our prescriptions are those implemented in *Mathematica 10*, which we have used for these calculations.

After using identities of elliptic integrals, and fixing the integration constants to the values (2.9) and (2.16), we get

$$\phi_q(r) = \frac{2q \left(F \left(\sin^{-1} \left(\sqrt{\frac{b(r+r_2+r_3)}{r}} \right) \middle| \frac{r_2}{r_3} a \right) - F \left(\sin^{-1}(\sqrt{b}) \middle| \frac{r_2}{r_3} a \right) \right)}{\sqrt{r_2(r_2+2r_3)}}, \quad (\text{A.15})$$

and

$$\begin{aligned} t_q(r) = & + \frac{\sqrt{r(r-r_2)(r+r_2+r_3)}}{\sqrt{r-r_3}} + r_0 \ln \left(\frac{\sqrt{(r-r_2)(r-r_3)} + \sqrt{r(r+r_2+r_3)}}{\sqrt{r(r+r_2+r_3)} - \sqrt{(r-r_2)(r-r_3)}} \right) \\ & - \frac{2r_0^3(r_2-r_3) \Pi \left(\frac{(r_0-r_3)a}{r_0-r_2}; \sin^{-1} \left(\sqrt{\frac{r-r_2}{(r-r_3)a}} \right) \middle| \frac{r_3 a}{r_2} \right)}{\sqrt{r_2(r_2+2r_3)}(r_0-r_2)(r_0-r_3)} \\ & + \frac{(2r_0^2(r_3-r_2) + r_0 r_2(r_3-r_2) + r_2 r_3(r_2+r_3)) F \left(\sin^{-1} \left(\sqrt{\frac{r-r_2}{(r-r_3)a}} \right) \middle| \frac{r_3 a}{r_2} \right)}{(r_3-r_0) \sqrt{r_2(2r_3+r_2)}} \\ & - \frac{2r_0(r_2-r_3)}{\sqrt{r_2(r_2+2r_3)}} \Pi \left(\frac{r_3}{r_2}; \sin^{-1} \left(\sqrt{\frac{r-r_2}{(r-r_3)a}} \right) \middle| \frac{r_3 a}{r_2} \right) \\ & - \sqrt{r_2(r_2+2r_3)} E \left(\sin^{-1} \left(\sqrt{\frac{r-r_2}{(r-r_3)a}} \right) \middle| \frac{r_3 a}{r_2} \right) - c_t(q). \end{aligned} \quad (\text{A.16})$$

$c_t(q)$ is the integration constant in the time integral

$$\begin{aligned} c_t(q) = & r_3 - \frac{2r_0^3(r_2-r_3) \Pi \left(\frac{(r_0-r_3)a}{(r_0-r_2)}; \sin^{-1}(\sqrt{a^{-1}}) \middle| \frac{r_3 a}{r_2} \right)}{\sqrt{r_2(2r_3+r_2)}(r_0-r_3)(r_0-r_2)} \\ & + \frac{(2r_0^2(r_3-r_2) + r_0 r_2(r_3-r_2) + r_3 r_2(r_3+r_2)) F \left(\sin^{-1}(\sqrt{a^{-1}}) \middle| \frac{r_3 a}{r_2} \right)}{\sqrt{r_2(2r_3+r_2)}(r_3-r_0)} \\ & - \frac{2r_0(r_2-r_3)}{\sqrt{r_2(2r_3+r_2)}} \Pi \left(\frac{r_3}{r_2}; \sin^{-1}(\sqrt{a^{-1}}) \middle| \frac{r_3 a}{r_2} \right) \\ & + r_0 \ln \left(\frac{2}{r_3+r_2} \right) - \sqrt{r_2(2r_3+r_2)} E \left(\sin^{-1}(\sqrt{a^{-1}}) \middle| \frac{r_3 a}{r_2} \right), \end{aligned} \quad (\text{A.17})$$

and

$$a = \frac{2r_2+r_3}{r_2+2r_3}, \quad (\text{A.18})$$

$$b = \frac{r_2}{2r_2+r_3}. \quad (\text{A.19})$$

A.2. $D = 5$

The integrals for the geodesics

$$t_q(r) = \int \frac{r^4 dr}{(r^2 - r_0^2)\sqrt{r^4 - q^2r^2 + q^2r_0^2}}, \quad (\text{A.20})$$

$$\phi_q(r) = -\int \frac{q dr}{\sqrt{r^4 - q^2r^2 + q^2r_0^2}}, \quad (\text{A.21})$$

are very similar to the four-dimensional ones. We rewrite them using two of the four roots of the polynomial under the surds

$$r_1 = \sqrt{\frac{q - \sqrt{q^2 - 4r_0^2}}{2}}, \quad r_2 = \sqrt{\frac{q + \sqrt{q^2 - 4r_0^2}}{2}}, \quad (\text{A.22})$$

(the other two roots are $-r_{1,2}$). Then

$$t_q(r) = \int \frac{r^4 dr}{(r^2 - r_0^2)\sqrt{(r^2 - r_1^2)(r^2 - r_2^2)}}, \quad (\text{A.23})$$

$$\phi_q(r) = -\int \frac{q dr}{\sqrt{(r^2 - r_1^2)(r^2 - r_2^2)}}. \quad (\text{A.24})$$

We perform the integrals again using *Mathematica 10*. After some manipulation and fixing the integration constants we obtain

$$\phi_q(r) = \frac{2q \left(-F \left(\sin^{-1} \left(\sqrt{\frac{(r-r_2)(r_1+r_2)}{2r_2(r-r_1)}} \right) \middle| l_+ \right) + F \left(\sin^{-1} \left(\sqrt{\frac{r_1+r_2}{2r_2}} \right) \middle| l_+ \right) \right)}{r_1 + r_2} \quad (\text{A.25})$$

and

$$\begin{aligned} t_q(r) = & \sqrt{\frac{(r-r_1)(r^2-r_2^2)}{r+r_1}} - \frac{2r_1^4}{(r_1^2-r_0^2)(r_1+r_2)} F \left(\sin^{-1} \left(\sqrt{\frac{(r+r_2)m_+}{r+r_1}} \right) \middle| l_+ \right) \\ & + (r_1-r_2) E \left(\sin^{-1} \left(\sqrt{\frac{(r-r_2)m_-}{r+r_1}} \right) \middle| l_- \right) \\ & + (r_1+r_2) F \left(\sin^{-1} \left(\sqrt{\frac{(r-r_2)m_-}{r+r_1}} \right) \middle| l_- \right) \\ & - \frac{r_0^3(r_1-r_2)}{(r_0-r_1)(r_0-r_2)(r_1+r_2)} \Pi \left(\frac{r_0-r_1}{(r_0-r_2)m_+}; \sin^{-1} \left(\sqrt{\frac{(r+r_2)m_+}{r+r_1}} \right) \middle| l_+ \right) \\ & + \frac{r_0^3(r_1-r_2)}{(r_0+r_1)(r_0+r_2)(r_1+r_2)} \Pi \left(\frac{r_0+r_1}{(r_0+r_2)m_+}; \sin^{-1} \left(\sqrt{\frac{(r+r_2)m_+}{r+r_1}} \right) \middle| l_+ \right) \\ & - c_l(q), \end{aligned} \quad (\text{A.26})$$

where the integration constant is given by

$$\begin{aligned}
c_t(q) = & -r_1 - \frac{2r_1^4}{(r_1^2 - r_0^2)(r_1 + r_2)} F(\sin^{-1}(\sqrt{m_+}) | l_+) \\
& + (r_1 - r_2) E(\sin^{-1}(\sqrt{m_-}) | l_-) + (r_1 + r_2) F(\sin^{-1}(\sqrt{m_-}) | l_-) \\
& - \frac{r_0^3(r_1 - r_2)}{(r_0 - r_1)(r_0 - r_2)(r_1 + r_2)} \Pi\left(\frac{r_0 - r_1}{(r_0 - r_2)m_+}; \sin^{-1}(\sqrt{m_+}) \middle| l_+\right) \\
& + \frac{r_0^3(r_1 - r_2)}{(r_0 + r_1)(r_0 + r_2)(r_1 + r_2)} \Pi\left(\frac{r_0 + r_1}{(r_0 + r_2)m_+}; \sin^{-1}(\sqrt{m_+}) \middle| l_+\right), \tag{A.27}
\end{aligned}$$

and

$$l_{\pm} = \pm \frac{4r_1 r_2}{(r_1 \pm r_2)^2}, \quad m_{\pm} = \frac{r_2 \pm r_1}{2r_2}. \tag{A.28}$$

Appendix B. Perturbative solution to order r_0^2

Here we give the result of the integrals (3.1) and (3.2) computed up to order r_0^2 , with the integration constants fixed to the values (2.9) and (2.16):

$$\begin{aligned}
t_q(r) = & \sqrt{r^2 - q^2} + \frac{r_0}{2} \left(\frac{r}{\sqrt{r^2 - q^2}} - 1 + 2 \ln \frac{r + \sqrt{r^2 - q^2}}{2r_0} \right) \\
& - r_0^2 \left(\frac{8q^2 - 7r^2}{8(r^2 - q^2)^{3/2}} + \frac{15}{8q} \arctan \frac{q}{\sqrt{r^2 - q^2}} \right) + \mathcal{O}(r_0^3), \tag{B.1}
\end{aligned}$$

$$\begin{aligned}
\phi_q(r) = & \arctan\left(\frac{q}{\sqrt{r^2 - q^2}}\right) + \frac{r_0}{q} \left(\frac{q^2 - 2r^2}{2r\sqrt{r^2 - q^2}} + 1 \right) \\
& + r_0^2 \left(-\frac{3q^4 - 20q^2r^2 + 15r^4}{16qr^2(r^2 - q^2)^{3/2}} + \frac{15}{16q^2} \arctan \frac{q}{\sqrt{r^2 - q^2}} \right) + \mathcal{O}(r_0^3). \tag{B.2}
\end{aligned}$$

Eliminating r in favor of q and t , and using the coordinates x and z defined in (2.10) we find

$$\begin{aligned}
x(q, t) = & q - r_0 \frac{(t - \sqrt{q^2 + t^2})^2}{2q\sqrt{q^2 + t^2}} \\
& + \frac{r_0^2}{16q^2(q^2 + t^2)^2} \left(15t(q^2 + t^2)^2 \arctan \frac{q}{t} \right. \\
& - 16q(q^2 + t^2)^2 \ln \frac{t + \sqrt{q^2 + t^2}}{2r_0} \\
& - q \left(6q^4 + 15t^4 + q^2t(21t + 4\sqrt{q^2 + t^2}) \right. \\
& \left. \left. - 8t\sqrt{q^2 + t^2}(3q^2 + 2t^2) \ln \frac{t + \sqrt{q^2 + t^2}}{2r_0} \right) \right) \\
& + \mathcal{O}(r_0^3). \tag{B.3}
\end{aligned}$$

$$\begin{aligned}
z(q, t) = & t - \frac{r_0}{2} \left(1 - \frac{t}{\sqrt{q^2 + t^2}} + 2 \ln \frac{t + \sqrt{q^2 + t^2}}{2r_0} \right) \\
& + \frac{r_0^2}{16q^2(q^2 + t^2)^2} \left(16t^4(-t + \sqrt{q^2 + t^2}) + q^4(-7t + 4\sqrt{q^2 + t^2}) \right. \\
& + q^2t^2(-23t + 16\sqrt{q^2 + t^2}) + 15q(q^2 + t^2)^2 \arctan \frac{q}{t} \\
& \left. + 8q^2\sqrt{q^2 + t^2}(q^2 + 2t^2) \ln \frac{t + \sqrt{q^2 + t^2}}{2r_0} \right) + \mathcal{O}(r_0^3). \tag{B.4}
\end{aligned}$$

These expressions are valid for $t > 0$. The analytic continuation (4.11) gives the results for $t < 0$.

References

- [1] Abbott B P *et al* (LIGO Scientific and Virgo Collaborations) 2016 Observation of gravitational waves from a binary black hole merger *Phys. Rev. Lett.* **116** 061102
- [2] Poisson E, Pound A and Vega I 2011 The Motion of point particles in curved spacetime *Living Rev. Relativ.* **14** 7
- [3] Schwarzschild K 1916 On the gravitational field of a mass point according to Einstein's theory *Sitzungsber. Preuss. Akad. Wiss. Berlin (Math. Phys.)* **S.189** arXiv:[physics/9905030](https://arxiv.org/abs/physics/9905030)
- [4] Amsel A J, Marolf D and Virmani A 2008 Collisions with black holes and deconfined plasmas *J. High Energy Phys.* **JHEP04(2008)025**
- [5] Figueras P, Hubeny V E, Rangamani M and Ross S F 2009 Dynamical black holes and expanding plasmas *J. High Energy Phys.* **JHEP04(2009)137**
- [6] Empanan R and Martínez M 2013 Black string flow *J. High Energy Phys.* **JHEP09(2013)068**
- [7] Sun M and Huang Y C 2015 Kerr black string flow *Nucl. Phys. B* **897** 98
- [8] Hamerly R and Chen Y 2011 Event horizon deformations in extreme mass-ratio black hole mergers *Phys. Rev. D* **84** 124015
- [9] Kastor D and Traschen J H 1993 Cosmological multi-black hole solutions *Phys. Rev. D* **47** 5370
- [10] Caveny S A and Matzner R A 2003 Adaptive event horizon tracking and critical phenomena in binary black hole coalescence *Phys. Rev. D* **68** 104003
- [11] Empanan R and Martínez M in preparation

Summary and Conclusions

CONCLUSIONS

This thesis has focused entirely on classical and thermodynamical aspects of black hole physics. We have considered four different classes of black holes that can be broadly classified as:

- black branes
- stationary black holes with non-Killing horizons
- rotating black holes
- dynamical black hole mergers

For each of these we have studied characteristic features and phenomena and we have produced new results. These results are contained in the four publications present in chapters 2, 3, 4 and 5. We will briefly summarise the main achievements.

Black branes in a box. We studied the effective hydrodynamics of neutral black branes enclosed in a cylindrical cavity. We used the size of the box, R , as a control parameter to study dynamic and thermodynamic instabilities. We observed that both instabilities disappear at the same critical value, R_c , of the cavity radius. We explained why the correlated stability conjecture, as usually interpreted, does not hold for all systems and we argued that its correct interpretation is the *Correlated Hydrodynamic Stability* (CHS). The CHS links the presence of unstable hydrodynamic modes to the local thermodynamic instability; this is transparent in our approach. We computed the viscosities of the effective fluid and obtained that they do not run with R . This might be a feature of a larger class of black branes. Close to the critical point, $R \approx R_c$, the wavenumber that marks the threshold of the instability exhibits critical behaviour $k_{GL} \sim (R - R_c)^{1/2}$.

Black string flow. We computed the smooth horizon of a black string falling through a planar acceleration horizon. This was the first exact description of a flowing horizon connecting a stringlike horizon with a planar one and it is valid for any number of dimensions $d > 5$. We obtained the horizon generators as well as the exact geometry of the flowing funnel. We computed a surface gravity that varies along the horizon. We also computed the expansion associated to the horizon generators: it vanishes in both asymptotic regions. This construction shows that stationary black holes with non-Killing horizons are possible with non-AdS asymptotics.

Bumpy black holes. We constructed numerically the first three families of rotating bumpy black holes in six dimensions. We followed the branches until they approached singular solutions. We found strong evidence of branches that exhibit conical structures close to the transitions to black rings, black saturns and di rings. We argued for the existence of a new class of solutions, *bumpy black rings*. We argued that transitions in higher branches would also occur beginning closer to the rotation axis and pinching-down subsequently at increasing value of the polar angle. Other branches were found to be extremely expanded in the rotation plane and exhibited the same kind of “cone” at their equator; thus becoming singular when highly deformed. We showed that these branches probably end in the phase diagram not connecting to any other black holes in the space of single spinning stationary solutions. Finally we found that a specific negative eigenvalue of the Lichnerowicz operator is not directly linked with a specific instability even though the total number of eigenvalues is consistent with the total number of instabilities at all times.

Black hole merger. We described in an exact analytic way the event horizon of a black hole merger in the extreme mass ratio (EMR) limit for four and five dimensions. Mergers in which the ratio of the masses is large are specially hard for numerical simulations. We expect that our exact results will be useful and serve as check/guide for future research in the area. We constructed the horizon by computing its generators and we extracted a number of parameters that characterise the merger. We identified the line of caustics, the critical radius at which both horizon touch, the big horizon relaxation timescale among other things. Finally we analysed the critical behaviour shortly before and after the pinch-on.

The same technique was used in the horizon construction of the black string flow and the black hole merger. This technique is very general and it can be employed in other setups to obtain different merging horizons. A clear extension to our work in Ch. 5 is to consider the Kerr metric instead of Schwarzschild’s. Kerr solution is less symmetric and different event horizons will be obtained depending on the relative orientation of the rotation and collision axes. Notice that by obtaining these horizons we will be able to describe all possible EMR black hole mergers occurring in our universe.

RESUMEN EN CASTELLANO

Esta tesis está enmarcada en el campo de los agujeros negros. En ella hemos considerado tanto agujeros negros en cuatro dimensiones como en dimensiones superiores ($d = 5$, $d = 6$ y d genérico).

Durante la tesis se han realizado cuatro proyectos que han involucrado diferentes tipos de agujeros negros. *Grosso modo* se pueden agrupar de la siguiente manera:

- Branas negras con horizontes extendidos
- Agujeros negros estacionarios con horizontes que no son de Killing
- Agujeros negros estacionarios que giran
- Fusión de agujeros negros

En cada uno de los proyectos se han estudiado fenómenos característicos del tipo de agujeros negros. Para conseguirlo se han utilizado diferentes técnicas adaptadas a cada uno de los problemas atacados. Cada uno de los estudios ha culminado en una publicación con nuevos resultados en el campo. Dichas publicaciones forman parte de esta tesis y están contenidas en los capítulos 2, 3, 4 y 5. En lo que sigue, explicaremos los fenómenos estudiados, mencionaremos las técnicas utilizadas y resumiremos los resultados obtenidos en cada una de ellas.

7.1 Branas negras en una caja

Las branas negras son agujeros negros que presentan horizontes de sucesos extendidos¹ y que poseen más de cuatro dimensiones. Este tipo de agujeros negros se ha estudiado mucho a lo largo de los años y algo que los caracteriza es ser inestables bajo perturbaciones a lo largo de sus horizontes. Perturbaciones de longitud de onda suficientemente larga ($\lambda > \lambda_{GL}$) crecen exponencialmente en el tiempo en vez de disiparse. Esta famosa inestabilidad es conocida como la inestabilidad de Gregory-Laflamme (GL).

¹Las que hemos estudiado en la tesis son p -branas neutras. Las soluciones presentan un total de $d = n + p + 3$ dimensiones y sus horizontes son una $(n + 1)$ -esfera por p direcciones planas, esto es $\mathbb{S}^{n+1} \times \mathbb{R}^p$.

Las branas negras aquí estudiadas, al igual que el agujero negro de Schwarzschild, tienen calor específico negativo. Esto significa que son termodinámicamente inestables cuando se ponen en contacto con un baño térmico a su misma temperatura. Hace unos años se propuso una conjetura que relacionaba las inestabilidades dinámicas y termodinámicas de agujeros negros con horizontes extendidos. Esta conjetura, por Gubser y Mitra, es conocida como la *Correlated Stability Conjecture* (CSC) y ha sido estudiada a fondo. Normalmente se emplea un parámetro de control (carga de algún tipo, condiciones de contorno de caja, etc.) con el que se pueden investigar tanto zonas de estabilidad como de inestabilidad. En muchos casos los regímenes de estabilidad termodinámica y dinámica coinciden. Se han encontrado sin embargo contraejemplos en los que la solución, aún siendo termodinámicamente estable, presenta inestabilidades dinámicas.

En el primer proyecto realizado durante esta tesis investigamos el sistema de una brana dentro de una caja con condiciones de contorno de Dirichlet. Atacamos el problema desde la teoría efectiva de *worldvolumes* de branas negras². Utilizamos el radio de la caja R como parámetro de control entre zonas de estabilidad e inestabilidad y observamos que las dos inestabilidades desaparecen para el mismo valor crítico de radio de la caja R_c . Esto es, para cajas con $R \leq R_c$ las inestabilidades desaparecen mientras que para cajas mayores las inestabilidades vuelven a estar presentes, como se sabe que lo están en el caso en el que no hay caja. Debido a que en este marco la relación entre inestabilidades de tipo hidrodinámico (inestabilidades dinámicas de longitud de onda arbitrariamente grande) y termodinámico están directamente relacionadas, en la publicación contenida en el capítulo 2 damos una explicación de como debe realmente entenderse la CSC. Derivamos también las cantidades asociadas al fluido efectivo, incluyendo sus correcciones disipativas (viscosidades). Desde la visión del fluido efectivo, la inestabilidad de GL presente en branas negras se traduce en una inestabilidad del fluido bajo perturbaciones de densidad, es decir, las ondas de sonido no se propagan. Por último, estudiamos el comportamiento crítico del sistema al estabilizarse cuando $R \rightarrow R_c$ y vimos que hay un exponente crítico determinando el comportamiento, $k_{GL} \sim (R - R_c)^{1/2}$.

7.2 Horizontes que fluyen (*Black String Flow*)

La mayoría de agujeros negros estacionarios estudiados en libros de texto y en una amplia mayoría de artículos presentan horizontes de Killing y por ende una temperatura constante (constante tanto a lo largo de secciones espaciales de sus horizontes como en el tiempo). Se ha mostrado, sin embargo, que ésta no es la única posibilidad para agujeros negros estacionarios. Éstos pueden tener horizontes que no sean de Killing y describir un gradiente de temperatura a lo largo de sus horizontes que se mantenga constante en el tiempo si presentan horizontes no compactos.

En el segundo proyecto de esta tesis construimos un horizonte de este tipo. El horizonte del *black string flow* describe una cuerda infinitamente larga en caída libre

²Esta teoría permite describir de manera efectiva la dinámica de estos agujeros negros mediante variables y ecuaciones propias de la hidrodinámica.

(a lo largo de su longitud) a un horizonte (planar) de aceleración³. La intersección entre ambos horizontes es suave y está perfectamente capturada en nuestra descripción. La construcción se llevó a cabo mediante la integración de geodésicas nulas en el espaciotiempo de la cuerda negra estática y eligiendo la familia de geodésicas específica que genera correctamente el horizonte. Efectivamente, los generadores de esta hipersuperficie nula no son vectores de Killing del espaciotiempo de la cuerda negra. Calculamos la temperatura (gravedad superficial) como el parámetro de no afinidad de los generadores del horizonte y vimos que el horizonte describe un gradiente de temperaturas que se mantiene constante en el tiempo. El horizonte describe un flujo de calor estacionario entre dos depósitos infinitos de calor, uno de ellos a temperatura finita (la cuerda) y el otro a temperatura cero (el agujero negro infinitamente grande).

La construcción es totalmente analítica y en un número arbitrario de dimensiones ($d \geq 5$). Además, ha sido realizada en espacio asintóticamente plano y muestra que los horizontes con flujo de calor no solamente existen en espacios con constante cosmológica negativa.

7.3 Agujeros negros *bumpy*

En cuatro dimensiones la única solución estacionaria de las ecuaciones de Einstein en el vacío tiene topología esférica y es el agujero negro de Kerr. En cinco o más dimensiones el espacio de soluciones de agujeros negros compactos y con momento angular es, sin embargo, mucho más rico. Son posibles horizontes estacionarios con topologías diferentes a la esférica: anillo negro, saturno negro, dos anillos negros concéntricos, etc.

En esta parte de la tesis estudiamos un tipo de agujeros negros estacionarios de topología esférica llamados *bumpy black holes*⁴. Los agujeros negros que consideramos tienen solamente un momento angular. Lo que diferencia a estos agujeros negros del agujero negro de Myers Perry⁵ (MP) es que la esfera transversa a la rotación varía de manera no monótona a lo largo del ángulo polar. Estos agujeros negros, en espacio de soluciones, conectan las ramas del agujero negro de Myers Perry con las otras soluciones (con diferentes topologías) mencionadas anteriormente.

Construimos numéricamente las primeras tres familias de agujeros negros *bumpy*. Realmente son seis familias de soluciones (se agrupan de dos en dos según el punto de corte con la rama del MP de donde nacen). Tres de ellas son las que conectan con el anillo negro, el saturno negro y los dos anillos negros concéntricos (las llamamos ramas-(+)). Las otras tres son las “anti-ramas” de estas y las llamamos

³Este horizonte también describe la caída libre de una cuerda negra fina (y por ende caliente) a un agujero negro esférico de radio característico mucho mayor que el de la cuerda (y por ende frío); en el límite cercano al horizonte del agujero negro grande.

⁴Aunque el estudio ha sido realizado en seis dimensiones, estas familias de agujeros negros existen para todo $d \geq 6$.

⁵El agujero negro de MP es la generalización a dimensiones $d > 4$ del agujero negro de Kerr y puede tener uno o más momentos angulares según el número de dimensiones.

ramas-(-); es decir, son soluciones con la deformación con respecto al MP en el sentido opuesto que en el caso de las ramas-(+).

Estudiamos a fondo la geometría de todas las soluciones. Para el caso de las ramas-(+) verificamos la presencia de conos en los horizontes para valores grandes de deformación. Estos conos aparecen para mediar la transición topológica que ocurre cuando dos ramas con diferente topología se encuentran en el espacio de soluciones. Con el estudio de la tercera rama-(+) obtuvimos evidencia fuerte de un nuevo tipo de solución al que llamamos anillo negro *bumpy*. Las ramas-(-) se extienden mucho en el plano de rotación y parecen acabar, en el espacio de soluciones, con una singularidad localizada en el ecuador y sin conectar a ninguna otra solución. En este artículo también estudiamos la estabilidad de estas soluciones mediante cantidades termodinámicas y mediante el espectro del operador de Lichnerowicz. Comprobamos que el número de autovalores negativos de este operador coincide con el número de inestabilidades presentes en las soluciones.

7.4 Fusión de agujeros negros

La fusión de agujeros negros es tradicionalmente parte del campo de la relatividad general numérica. Para describir de manera razonable la radiación gravitatoria emitida y el horizonte de sucesos de un proceso de fusión de agujeros negros se requieren tanto superordenadores como técnicas numéricas muy complejas.

Hay sin embargo un caso en que el proceso puede tratarse de manera analítica. Es el límite de razón de masas extremas (EMR) en que uno de los agujeros negros tiene infinita o cero masa en comparación al compañero. Curiosamente casos en que las masas difieren mucho son especialmente complicados numéricamente. Nosotros consideraremos el límite exacto en que $m/M \rightarrow 0$ manteniendo la masa del agujero negro pequeño, m , fija y la del grande, M , infinita.

En general los horizontes de sucesos pueden describirse mediante sus generadores. Éstos son simplemente rayos de luz en el espaciotiempo que nunca abandonan el horizonte. En el límite de EMR, la geometría está dominada totalmente por el agujero negro pequeño y basta con trazar geodésicas nulas en el espaciotiempo de éste. En este proceso, al fijar las constantes de integración cuidadosamente, es posible obtener el horizonte de sucesos de una colisión de dos agujeros negros.

Como última parte de esta tesis construimos y caracterizamos el horizonte de sucesos de una colisión de agujeros negros en el límite EMR (en cuatro y cinco dimensiones) considerando un agujero negro pequeño de tipo Schwarzschild. Una vez obtenida la hipersuperficie, identificamos la línea de cáusticas, el radio crítico r_* en el cual los horizontes se tocan, los tiempos de relajación del agujero negro grande, etc. Estudiamos los instantes críticos anteriores y posteriores al primer contacto entre los horizontes. Justo antes de la fusión, el horizonte del agujero negro grande presenta un cono con un cierto ángulo, este ángulo va cerrándose hasta que llega a cero en el momento del contacto ($t = t_*$). Hemos observado que el cierre del ángulo del cono está bien descrito por un comportamiento crítico $\sim (t_* - t)^\gamma$ con $\gamma = 1/2$. Una vez los dos horizontes se han unido, se forma una

garganta conectando a ambos. Se ha observado que esta garganta crece linealmente con el tiempo, $\rho \sim (t - t_*)$. Estos últimos resultados han sido obtenidos tanto para cuatro como para cinco dimensiones y parecen indicar cierta independencia del número de dimensiones.

